The University Of Sheffield.

Advanced Wireless Localisation Methods Dealing with Incomplete Measurements

By

Chao Liu

Supervised by:

Prof. Lyudmila Mihaylova

Dr. Iñaki Esnaola

A thesis submitted in partial fulfilment of the requirements for the degree of

Doctor of Philosophy

University of Sheffield

Faculty of Engineering

Department of Automatic Control and Systems Engineering

September 2018

Abstract

Positioning techniques have become an essential part of modern engineering, and the improvement in computing devices brings great potential for more advanced and complicated algorithms. This thesis first studies the existing radio signal based positioning techniques and then presents three developed methods in the sense of dealing with incomplete data. Firstly, on the basis of received signal strength (RSS) location fingerprinting techniques, the Kriging interpolation methods are applied to generate complete fingerprint databases of denser reference locations from sparse or incomplete data sets, as a solution of reducing the workload and cost of offline data collection. Secondly, with incomplete knowledge of shadowing correlation, a new approach of Bayesian inference on RSS based multiple target localisation is proposed taking advantage of the inverse Wishart conjugate prior. The MCMC method (Metropolis-within-Gibbs) and the maximum a posterior (MAP) / maximum likelihood (ML) method are then considered to produce target location estimates. Thirdly, a new information fusion approach is developed for the time difference of arrival (TDOF) and frequency difference of arrival (FDOA) based dual-satellite geolocation system, as a solution to the unknown time and frequency offsets. All proposed methods are studied and validated through simulations. Result analyses and future work directions are discussed.

Acknowledgements

The author would like to express his outmost gratitude to the supervisor Professor Lyudmila Mihaylova! Through the whole PhD study, she teaches the author with professional and inspiring knowledge. She encourages the author through the whole PhD study with great enthusiasm and patience. The acknowledgements go also to the second supervisor Dr Iñaki Esnaola for providing vital guidance and expertise!

The author would like to specially thanks Dr Le Yang for his extraordinary tuition and priceless friendship! The author would also like to thank Dr Naveed Salman, Aroland Kiring, Yuxin Zhao and Dr Allan De Freitas for their help and collaborations!

At last, the author would like to express the wholehearted gratitude to his wife, Mengzi Wang, for her invaluable support and love!

Contents

List of Symbols and Notations

x, x_i, y, y_i	Coordinates
$\mathbf{s}, \mathbf{s}_i$	Target/Sensor location
m, M	Number of targets
$\mathbf{b}, \mathbf{b}_j$	Base station location
n, N	Number of base stations
$z, z_{i,j}\mathbf{z}, \mathbf{z}_i, \bar{\mathbf{z}}, \bar{\mathbf{z}}_i$	Received signal strength (RSS)
$f, f_{i,j}, \mathbf{f}, \mathbf{f}_i$	Noise-free, RSS
b, b_j	Transmitting power in dB
l_0	Referencing path loss measure at 1 meter away from the transmitter
α, β	Path loss exponent
$d, d_{i,j}, \mathbf{d}$	Distance
$\varepsilon, \boldsymbol{\varepsilon}$	Shadowing attenuation
d_c, D_c	Decorrelation distance
$d_{i,j}$	Distance between the j-th transmitter and i-th receiver
ε	Shadowing attenuation
σ_ε	Shadowing variance
$\sigma_\varepsilon, \boldsymbol{\sigma}_\varepsilon, \boldsymbol{\Sigma}_\varepsilon, \mathbf{C}$	Shadowing variance/covariance

w, w_i	Weight
$p(\cdot)$	Probability
$\mathcal{L}(\cdot)$	Likelihood
$\mathbb{E}(\cdot)$	Expected value
$\mathrm{Var}(\cdot)$	Variance
$\mathrm{Cov}(\cdot)$	Covariance
$\mathcal{I}(\cdot)$	Fisher information
$\mathcal{IW}(\cdot)$	Inverse Wishart Distribution

List of Abbreviations

AOA	angle of arrival
ATR	asymmetric trip ranging
BDS	BeiDou navigation satellite system
BLUE	best linear unbiased estimate
BN	beacon node
BS	base station
CAF	cross ambiguity function
CRLB	Cramér-Rao lower bound
FDOA	frequency difference of arrival
GLONASS	global navigation satellite system
GLS	generalised least square
GPS	global positioning systems
MAP	maximum a posterior
	MCMC Markov chain Monte Carlo
ML	maximum likelihood
MS	mobile station
OSP	orthogonal subspace projection
PLE	path loss exponent

RFID	radio-frequency identification
RTOF	roundtrip time of flight
TDOA	time difference of arrival
TOF	time of flight
WLAN	wireless local area network

List of Figures

List of Publications

Peer Review Conference Paper

1. C. Liu, A. Kiring, N. Salman, L. Mihaylova, and I. Esnaola, "A kriging algorithm for location fingerprinting based on received signal strength", in *Proceedings of 2015 Workshop on Sensor Data Fusion (SDF 2015)*, 2015

2. C. Liu, L. Yang, and L. Mihaylova, "Dual-satellite source geolocation with time and frequency offsets and satellite location errors", in *Proceedings of 20th International Conference on Information Fusion (FUSION 2017)*, 2017. (**ISIF 2017 Tammy Blair Best Student Paper Award**)

3. Y. Zhao, C. Liu, L. S. Mihaylova, and F. Gunnarsson, "Gaussian process for rss fingerprints construction in indoor localization", in *21st International Conference on Information Fusion (FUSION 2018)*, 2018

4. A. Kiring, N. Salman, C. Liu, I. Esnaola, and L. Mihaylova, "A shrinkage-based particle filter for tracking with correlated measurements", in *Proceedings of 2015 Workshop on Sensor Data Fusion (SDF 2015)*, 2015

Peer Review Journal Paper

5. A. Kiring, N. Salman, C. Liu, I. Esnaola, and L. Mihaylova, "Tracking with sparse and correlated measurements via a shrinkage-based particle filter", vol. 17, no. 10, pp. 3152–3164, 10 2017

Chapter 1

Introduction

1.1 Wireless Localisation

Wireless localisation, or wireless positioning, is the techniques that estimate target locations through deploying wireless devices, measuring and analysing signals. With the advances in wireless techniques and the decrease in the cost of electronic products, wireless devices become prevalent and start playing essential roles in both our everyday life and industry. In the meantime, with the development of wireless localisation methods, location-based services become increasingly popular and influential.

The precision farming, which has been considered as the next generation of agriculture, requires positioning techniques as fundamental of farming management systems including field observing, data analysing and decision making [6]. Modern logistics depends on position systems in cargo sorting and transportation [7]. For providing better healthcare, hospitals start to using wireless devices to locate and monitor the patients [8]. In large shopping malls or tourist attractions, positioning applications can provide basic navigation.

A well known wireless positioning system is the global positioning system (GPS). It is a satellite-based radio frequency navigation system launched by the U.S. government in 1978, which provide geolocation and time information to a GPS receiver. It is now the most widely used positioning technique in outdoor environments, and

its accuracy meets the requirement of most outdoor applications. There are similar projects including the global navigation satellite system (GLONASS) launch by Russian in 1982, Galileo positioning system launched by the European Union in 2011 and BeiDou navigation satellite system (BDS) launched by China in 2000 [9]. However, the satellite-based positioning systems perform poorly under non-line-of-sight conditions, such as in dense forests or high building area, and it is not applicable for in-building environments [10].

Except for satellite-based systems, different localisation methods have been developed for wireless communication networks. These techniques are developed upon the wireless measurements, which are usually related to the relative location of the base station and target. Common wireless measurements include directional measurement, e.g. the angle of arrival (AOA), ranging-related measurement, e.g. the time of arrival (TOA) and the received signal strength (RSS) [11]. However, these measurements suffer from the uncertainty of radio propagation, such as shadow fading and multipath effect, and finally result in reduced positioning accuracy and integrity.

By taking advantage of statistics, more accurate models can be built from measurements, which can further improve the target location estimate. However, it typically demands a large number of measurements to produce reliable models, and moreover, multi-dimension problems would significantly improve the requirements of measurements. Therefore, it is worth to enhance the existing positioning techniques in the sense of utilising statistical modelling and dealing with incomplete measurements.

1.2 Aims and Achievements

1.2.1 Aims

Positioning algorithm based on statically models requires a large number of measurements to compute model parameters and further produces accurate estimates.

However, measurements collection can be time-consuming, and parameter estimation can be computationally complex, or even unavailable under specific circumstances.

This thesis aims to improve existing positioning techniques in the sense of tackling incomplete data. On the one hand, through analysing and modelling the correlation between the limited measurements, advanced algorithms are proposed to improve the efficiency or accuracy via utilising the correlation. On the other hand, for scenarios where there is a lack of information about the measurement models, innovative approaches can be developed to reduce the adverse effects on estimation.

1.2.2 Achievements

This thesis presents will three main achievements:

1. Two Kriging interpolation algorithms are proposed to improve the efficiency of the offline data collection of location fingerprinting techniques.

The fingerprinting method involves an offline data collection phase in order to build a fingerprint database covering the whole area of interest. However, data collection at refined grid points leads to massive workload. This thesis proposes a solution that taking measurements only at sparsely distributed grid points and employing the Kriging methods to generate fingerprints at denser points. The advantage of the Kriging method is that it exploits the spatial correlation from data and performs interpolation based on the correlation model. Simulations and real data experiments are conducted, and the results validate that the proposed approaches significantly reduce the offline workload while having acceptable localisation accuracy.

2. On the lack of sufficient received signal strength (RSS) measurements, a new approaches of Bayesian inference on multi-target location is proposed to improve localisation through taking advantage of shadowing correlation.

For RSS based localisation, taking account of the shadowing correlation could improve the accuracy. However, to obtain normal correlation values requires sufficient

RSS measurements especially for multi-target problems. With the aim of coping with the prior knowledge of shadowing correlation contained in a limited number of measurements, the inverse Wishart distribution is proposed, and a close-form of the posterior is derived. Afterwards, the Markov chain Monte Carlo (MCMC) is applied to generate samples from the posterior and further yield the target location estimate as the sample mean. The maximum a posterior (MAP) / maximum likelihood (ML) method is considered as an alternative way to estimate target locations. Simulation results are studied, and several insights are discussed.

3. In time difference of arrival (TDOA) and frequency difference of arrival (FDOA) based positioning systems, a new closed-form algorithm is developed for handling unknown linear nuisance parameters in measurement models.

In dual-satellite geolocation systems where two satellites are imperfectly time-synchronised and frequency-locked, the TDOA and FDOA measurements subject to unknown time and frequency offsets. Achieving the maximum likelihood (ML) geolocation performance usually requires jointly estimating the target location and extra variables (i.e., unknown time and frequency offsets as well as possibly existing satellites errors), which is computationally intensive. In the thesis, a novel closed-form geolocation algorithm is proposed. It first fuses the TDOA and FDOA measurements in a low-complex way to mitigate the unknown linear time and frequency offsets and then produce a pair of TDOA and FDOA values for target geolocation. From the pair of values, the final estimate is later found via standard geolocation algorithm. Simulation results verify that the developed algorithm attains the Cramér-Rao lower bound (CRLB) and is faster under Gaussian noises and mild conditions.

1.3 Organisation of Thesis

The remaining parts of the thesis are organised as follows: Section II reviews different types of wireless measurements and some existing positioning algorithms. Section III introduces the Kriging methods for RSS fingerprint interpolation. Simulations

results are analysed. Section IV first presents the new proposed Bayesian inference on multi-target localisation and later discusses the MCMC and MAP/ML methods as localisation approaches based on experiments results. Section V initially analyses the CRLB of TDOA and FDOA geolocation problems to reveal some insights. Based on that, the new closed-form algorithm is developed. Simulation results are studied afterwards. The final section concludes the thesis, and possible future work directions are depicted at last.

Chapter 2

Literature Review

Many wireless localisation algorithms have been developed during the past few decades. The applications have been ubiquitously adopted from military weapons to civil engineering [12], [13]. This chapter presents a survey of wireless localisation techniques and categorises them based on system topologies, positioning algorithm and corresponding measurement.

2.1 System Topologies

The localisation systems can be divided into four topologies depending on which part needs to be localised between the transmitters and receivers and where the algorithm is processed [14]:

1. **Remote positioning system**: The transmitter is the mobile target and supposes to be localised. Several receivers with known locations measure the signal of the transmitter. The measurements are then collected and passed to a master station to perform the localisation.

2. **Self-positioning**: Several transmitters are located at known positions. The receiver is capable of measuring the signals of transmitters and computing its location on board.

3. **Indirect remote positioning system**: A mobile receiver measures the signal

of several transmitters with known locations. However, the measurements need to be passed to a master station to perform positioning.

4. **Indirect self-positioning system**: Signal of a mobile transmitter is measured by several receivers with known locations. However, the measurements are collected and transferred to the mobile transmitter to perform positioning.

However, the same type of measurement and positioning algorithm can be adopted by different system topologies.

2.2 Positioning Algorithms and Signal Measurements

2.2.1 Proximity Positioning

The proximity method estimates a target position by recording when the target comes into the sensing of a base station. The target is estimated to overlap the fixed receiver which last recorded it. An example of proximity localisation is the *radio-frequency identification* (RFID), where a target attached with an RFID tag is located when recognised by an RFID scanner [15], [16].

An illustration of proximity localisation is given in 2.1.

The proximity positioning has several advantages. First, it can be used with nearly all types of existing radio infrastructures. Second, in cases such as the RFID, because targets only have to emit an identification code, they can be designed to be very low-cost. However, the proximity technique has some disadvantages. First, localisation precision is quite limited since every target within the proximity area of a receiver will be estimated at the same location of the receiver. Second, the target can only be identified when it approximates a receiver. In order to cover the whole area and maintain the accuracy of localisation, plenty of receivers need to be deployed.

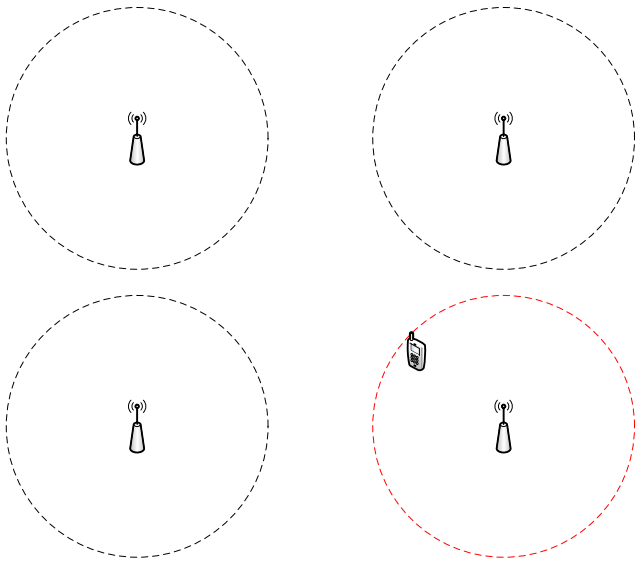

Figure 2.1: Proximity localisation.

2.2.2 Triangulation and Directional Measurement

Triangulation is a method of determining the target location utilising directional measurements, such as the angle of arrival (AOA). AOA is a measure of the arriving direction of signals. Utilising a set of receivers, e.g. an antenna array, time delays of the arrival signal between receivers can be converted into the AOA measurement [17], [18]. Figure 2.2 illustrates the triangulation method. As shown, A and B are the fixed reference receivers. The dash lines indicate the directions of arrival signal transmitted by an unknown target. Intuitively, the target is estimated at the intersection of direction lines [19].

The triangulation technique has several advantages. Firstly, the triangulation can produce highly accurate estimates if the directional measurements are of high quality. Secondly, the triangulation method improves the positioning accuracy compared to the proximity method because the target can be estimated in all areas covered by the receiver. The major drawback of triangulation is that directional measurements are severely affected by the obstacles and multipath propagation.

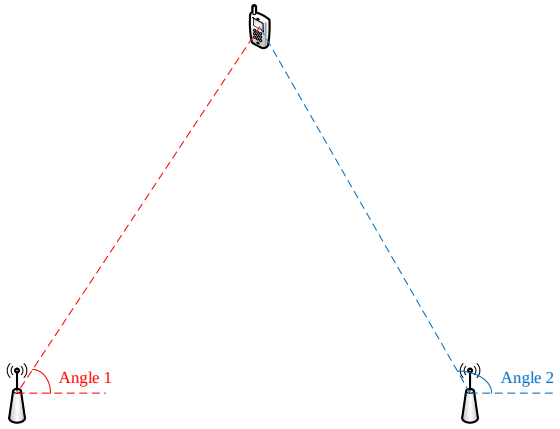

Figure 2.2: Triangulation.

2.2.3 Trilateration and Ranging Measurement

Trilateration is a method of determining the location of a target utilising distance information derived from ranging measurements. As shown in Figure 2.3, the possible target locations form in two dimensions (2D) a circle of which the centre is the known receiver and the radius equals to the distance between the target and a known fixed station. At least three receivers and corresponding measurements are needed to perform localisation. The target location is estimated at the intersection area of three circles.

The distance between the target and receiver can be estimated from the ranging measurements, such as the time of arrival (TOA), two-way time of arrival and received signal strength (RSS).

Time of Arrival is the measure of the propagation time of a radio signal transmitted from a transmitter (beacon node) to a receiver (receiver node). The transmitting timestamp is coded and carried in the signal. A receiver compares the receiving timestamp with the transmitting timestamp to produce the TOA measurement. Given the signal propagation speed, the distance between the transmitter and receiver can be estimated [20], [21].

However, the radio signal propagates in the air at a speed of light. Therefore, to

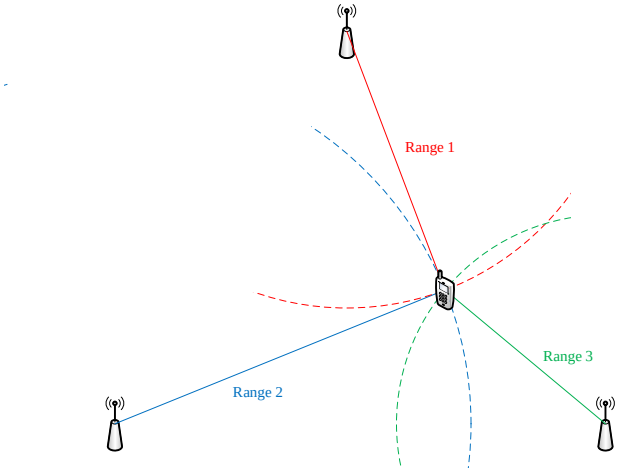

Figure 2.3: Trilateration

obtain accurate distance information, it demands a high-frequency clock and clock synchronisation between the transmitter and receiver, which is a strict prerequisite in general.

Two-way Time of Arrival is an alternative way to measure the radio signal propagation time. First, the original signal is transmitted by a transmitter. Once observes the signal, the receiver will send a response signal back to the transmitter. By comparing the transmitting time of the original signal and receiving time of the response signal at the transmitter, the distance between the transmitter and receiver can be estimated.

As an alternative, the two-way TOA does not require clock synchronisation between the transmitter and receiver, but the processing time elapses before the receiver returns the responding signal will affect the distance estimation. However, if the processing time is relatively small compared with the signal propagation time, it can be ignored [22].

Received Signal Strength is a measure of energy strength of the received signal. It can apply acoustic signal [23]–[27], and radio signal. In free space, energy decay

of a radio signal is defined by Friis free-space propagation model. Therefore, the received energy strength at the receiver is given by

$$P_r = \frac{P_t G_t G_r \lambda^2}{(4\pi)^2 d^2}, \tag{2.1}$$

where P_t is the transmitted energy strength, G_t and G_r are the gain factors of the transmitter and receiver, λ is the signal wavelength and d is the distance between the transmitter and receiver.

In the literature of wireless signal propagation, the logarithm form of energy decay model is more widely employed. A generic logarithm RSS model can be found in [28], which is

$$z = P_t - L_0 - 10\alpha \log_{10} d + \varepsilon, \tag{2.2}$$

where b is the transmitting power in logarithm, l_0 is the reference path loss measured at 1 meter away from the transmitter, α is the path loss exponent and ε represents the shadowing attenuation and is Gaussian distributed with zero mean and variance σ_ε^2.

Given the locations of transmitters and receivers, a specific propagation model of RSS can be established via computing the statistics of RSS measurements. Inversely, with a known path loss model and the locations of receivers, the distance from the target to Receivers can be derived.

Compared to decent TOA and two-way TOA measurements, RSS measurements are more accessible in general. However, RSS measurements are severely affected by environment phenomena such as reflection, diffraction and scattering, which further causes errors in distance estimation.

2.2.4 Multilateration

Multilateration is similar to the trilateration method. It determines the location of a target using measurements such as the time difference of arrival (TDOA). First, the range differences from the target to two known fixed base stations can be calculated

from TDOA measurements. Obtained the range differences, possible locations of the target will form a hyperbola between the two fix base stations, which is shown as the dashed line in Figure 2.4. In order to perform localisation, at least two TDOA measurements between three base stations are essential. The target location is estimated at the intersection area of two hyperbolas [22].

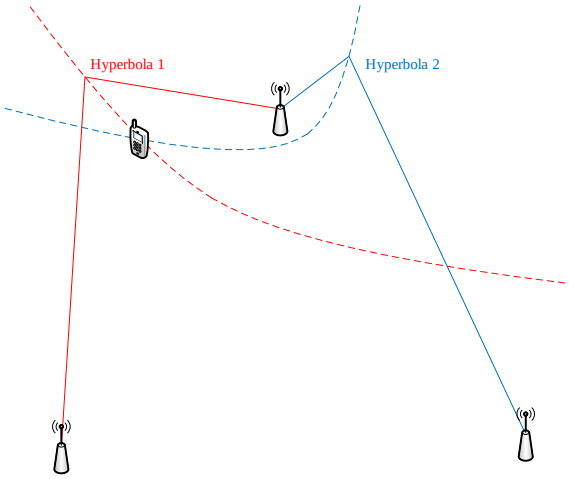

Figure 2.4: Multilateration

2.3 RSS Fingerprinting Localisation

The fingerprinting localisation, as the name suggested, estimates a target position via features matching. The RSS fingerprinting method utilises the RSS measurement as the location feature. In the paper [29], the proposed "empirical method" for target localisation is actually the original form of location fingerprinting, despite that it is claimed to be triangulation in a broad sense.

The primary advantage of the fingerprinting methods is that it exploits existing radio infrastructures, such as wireless local area networks (WLAN) or cellular networks. Thus extra deployment costs can be avoided [30]. Moreover, once given the fingerprints database, the base station locations are not required to perform localisation.

2.3.1 Fingerprinting Localisation

There are two stages for location fingerprinting methods: offline data collection phase and positioning phase. In the offline stage, RSS measurements of several base stations are collected for all predefined points in the area of interest. Later, the area can be approximately represented by a set of elements, given as [10]

$$\{\mathbf{p}_i, \mathbf{z}_i, \theta_i\}, i = 1, \ldots, M \tag{2.3}$$

where $\mathbf{p}_i = [x_{p,i}, y_{p,i}]$ represents the coordinates of i-th reference points in 2D, $\mathbf{z}_i$ represents the composite vector of RSS measurements, , and θ_i contains other optional information such as variance [31] or orientation [29].

In the paper [29], three 2.4GHz wireless LAN base stations are deployed in a typical office environment. A human hold PC visits all reference points to collect RSS fingerprints. However, as reported in [32], the orientation would affect the RSS measuring especially when the device is held by a human. One solution to the orientation problem is to have RSS measured from a different direction and take the average. Furthermore, the RSS collection can be controlled remotely to mitigate the human body effects, for example, using a small robot.

Given the fingerprint database, there are different frameworks for estimating target location in the positioning stage.

2.3.1.1 Deterministic Framework

The deterministic method mainly refers to the k nearest neighbour method. Given the target RSS measurement, $\mathbf{z}_s = [z_{s,1}, \ldots, z_{s,n}]^\mathsf{T}$, similarity between the target measurement and known fingerprints is calculated adopting a specific metric, e.g. Euclidean distance (ℓ_2 norm) or Manhattan distance (ℓ_1 norm), as given by

$$\text{Euclidean distance: } \|\mathbf{z}_s - \mathbf{z}_i\|_{\ell_2} = \sqrt{\sum_{j=1}^{n} (z_{s,j} - z_{i,j})^2} \tag{2.4a}$$

$$\text{Manhattan distance: } \|\mathbf{z}_s - \mathbf{z}_i\|_{\ell_1} = \sum_{j=1}^{n} |z_{s,j} - z_{i,j}| \tag{2.4b}$$

where $|\cdot|$ is the absolute value and n is the number of base stations. Other metrics such as modified p-norm and infinity-norm are considered in [33], [34].

Once found k most similar fingerprints, the target location $\mathbf{s} = [x_s, y_s]^\mathsf{T}$ can be estimated as a linear combination of the fingerprint locations, which is

$$\hat{\mathbf{s}} = \sum_{i=1}^{k} w_i \cdot \mathbf{p}_i \tag{2.5}$$

where w_i is the weights. The weights can be equal or can be calculated as the inverse of the norm [35].

2.3.1.2 Probabilistic Framework

Given the target measurement $\mathbf{z}_s$, the idea of probabilistic framework is to compute the posterior probability $p(\mathbf{z}_i \mid \mathbf{z}_s)$ for each known fingerprints. According to Bayes' rule, the conditional probability is given as

$$p(\mathbf{z}_i \mid \mathbf{z}_s) \propto p(\mathbf{z}_s \mid \mathbf{z}_i) \cdot p(\mathbf{z}_i) \tag{2.6}$$

where $p(\mathbf{z}_s \mid \mathbf{z}_i)$ is the likelihood, and $p(\mathbf{z}_i)$ is the prior.

In cases where there is a lack of prior information about known fingerprints, the prior $p(\mathbf{z}_i)$ can be assumed following the uniform distribution [36]. Consequently, the similarities between the target measurement and known fingerprints are mainly determined by the likelihood $p(\mathbf{z}_s \mid \mathbf{z}_i)$. The likelihood can be either computed based on the actual histogram of RSS samples measured at referencing location [37], or using a distribution assumption, such as Gaussian distribution [38].

Similarly to the deterministic framework, once find the several fingerprints that have the highest posterior, the target location can be estimated as a linear combination of the fingerprint locations as given by (2.5), where the weights are typically given by the normalised posterior [31].

2.3.2 Fingerprints Interpolation

The localisation accuracy depends highly on the predefined reference points in the sense of density. More precisely, it is intuitive that having more reference points distributed in the area of interest will improve the correctness of the most matching fingerprint.

However, having denser reference points would significantly increase the workload of the offline collection and possible maintenance in the future. One solution to reduce the workload is taking measurements only at part of the reference points, and later to utilise interpolation method to estimate the RSS at unmeasured reference points. The idea that using interpolation methods can be found in literature.

In [39], RSS fingerprint at unmeasured location is estimated based on a specific propagation model including a distance-dependent path loss and environmental attenuation. Corresponding parameters are estimated from limited actual measurements. The location related environmental attenuation is partitioned as reflection and wall attenuation, and these attenuation can be estimated based on the construction floor plan. However, the estimation is too simply to characterise the complex and rapid varying attenuation, and therefore leads to noticeable errors. Similar work has been repeated in [40].

In [41], high-resolution grid-based fingerprint databases are produced from low-resolution databases via merging the measurements from two adjacent grids. First, the original RSS fingerprint database is represented as an RGB colour map. To refine the resolution, a grid splits into two grids of half size. Then, the RSS of a half-size grid is adjusted based on the RGB value averaging of original colour and colour of adjacent grid. Though the interpolation is conducted through RGB colour "fusion", it is essentially linear interpolation.

A recent paper [35] investigates spatial interpolation and extrapolation methods for construction of fingerprint databases, including *linear interpolation* based on Delaunay triangulation, nearest neighbour (NN) interpolation and k-nearest neighbour (KNN) with the inverse distance weighting (IDW) to name a couple. In the IDW

method, RSS estimates are given by a weighted sum of unknown surrounding data points, where the weight as calculated as the normalised inverse of actual distance (Euclidean distance).

In [42], an adaptive smoothing method is proposed with regard to the discontinuity of RSS as a result of walls. The complete fingerprint database is produced using IDW interpolation method.

2.4 Shadowing Attenuation

Compared with the free-space propagation, RSS measurements in practice may fluctuate due to the fast fading and the shadowing attenuation. The former is caused by the multipath propagation effects, while the latter is considered as results from large obstacles lying in the propagation path. The multipath effect can be eliminated by averaging RSS measurements over a short period. However, the propagation environment merely changes, and thus the shadowing attenuation at a specific location remain at the same level **fading**.

The RSS model represented in logarithm form in given in (**??**), where the shadowing attenuation ε is typically assumed following a zero-mean Gaussian distribution.

2.4.1 Shadowing Correlation

The shadowing attenuation is main caused by the propagation environment, and thus the shadowing at two closed locations can be considered correlated. In literature, there are several models of shadowing correlation.

For convenience, the following notations will be adopted. Assuming there are n targets, and the location of the i-th target is denoted by $\mathbf{s}_i = [x_{s,i}, y_{s,i}]^\mathsf{T} (i = 1 \dots n)$. There are m base stations, and the location of the j-th base station is denoted by $\mathbf{b}_j = [x_{b,j}, y_{b,j}]^\mathsf{T} (j = 1 \dots m)$. The distance between the i-th target and j-th base station is given by $d_{i,j} = \sqrt{(x_{s,i} - x_{b,j})^2 + (y_{s,i} - y_{b,j})^2}$. The RSS of the j-th base station measured by the i-th target is denoted by $z_{i,j}$.

2.4.1.1 Auto-correlation

For two closely located static targets in a localisation scenario, RSS of the same base station will suffer similar shadowing attenuation, because the two propagation path are close to each other and thus might encounter the same obstacles. Consequently, the shadowing auto-correlation of two closely located targets is determined by the distance between targets, as given in [43]:

$$\rho(z_{i,j}, z_{k,j}) = \exp\left(- \frac{d_{i,k}}{d_c} \right), \tag{2.7}$$

where $z_{k,j}$ is the RSS measured by the k-th target, $d_{i,k} = \sqrt{(x_{s,i} - x_{s,k})^2 + (y_{s,i} - y_{s,k})^2}$ is the distance between the i-th target and k-th target, and d_c is the correlation/decorrelation distance which indicates the maximum distance that shadowing correlations can be observed.

2.4.1.2 Cross-correlation

According to literature [44], [45], the shadowing cross-correlation can be found when two base stations are transmitting to a common target. Regardless of distance between the two base stations, RSS measured by the common target will suffer similar shadowing attenuation if the directions of signal sources are close to each other. Therefore, the shadowing cross-correlation is determined by the angle difference of arrival (ADOA).

For outdoor propagation, there are two models for shadowing cross-correlation [46]:

- Model "0.8/0.4" by Granziano [47]

$$\rho(z_{i,j}, z_{i,l}) = \begin{cases} 0.8 - |\theta_{i,jl}| \,/150, & \text{if } |\theta_{i,jl}| \leq 60^\circ \\ 0.4, & \text{if } |\theta_{i,jl}| > 60^\circ \end{cases} \tag{2.8}$$

where $z_{i,l}$ is the RSS of the l-th base station, and $|\theta_{i,jl}|$ is the ADOA.

- Model "0.8/0.0" by Sørensen [48]

$$\rho(z_{i,j}, z_{i,l}) = \begin{cases} 0.78 - 0.0056\,|\theta_{i,jl}|\,, & \text{if } |\theta_{i,jl}| < 15^\circ \\ 0.48 - 0.0056\,|\theta_{i,jl}|\,, & \text{if } 15^\circ \leq |\theta_{i,jl}| < 60^\circ \\ 0.0, & \text{if } |\theta_{i,jl}| > 60^\circ \end{cases} \tag{2.9}$$

For indoor propagation, some measurement campaigns have been conducted [49], [50] and the conclusion contradicts the aforementioned models. In [49], transmitters are placed on different floors. On the one hand, if the transmitters are placed in the similar positions of adjacent floors, the shadowing correlation varies between 0.64 to 0.95. On the other hand, when the transmitters are placed in the opposite positions of adjacent floors, the correlation is found between -0.65 to -0.34. In [50], two transmitters are placed closely on a floor, and a third transmitter is placed at a far point on the same floor. Measurements are collected along the corridor, and the cross-correlation is investigated as a function of propagation distance and time window. The results show that cross-correlation varies between 0.8 to -0.1.

There is currently no well-agreed model for predicting the correlation. However, two key factors shall be considered in practice [44]:

- If the ADOA is small, the two path profiles share many common elements and are expected to have high correlation. Hence the cross-correlation should decrease with increasing ADOA.

- The relative values of the two path lengths. If the ADOA is close to zero, the cross-correlation is expected to be one when the path lengths are equal. As one of the path lengths is increased, it incorporates elements which are not common to the shorter path, so the cross-correlation decreases.

2.4.1.3 The Third Type Correlation

For multiple target localisation, if the shadowing auto-correlation and cross-correlation are both considered, there will arise the third type of correlation. For example, if

$z_{i,j}$ is auto-correlated to $z_{k,j}$, and $z_{i,j}$ is cross-correlated to $z_{i,l}$, there is obvious correlation between $z_{i,l}$ and $z_{k,j}$ though they are measured from different base station and targets.

One way to model the third type of correlation refers to Graziosi [51], in which the correlation is a production of auto-correlation and cross-correlation, i.e.

$$\rho(z_{i,l}, z_{k,j}) = \rho(z_{i,j}, z_{k,j}) \cdot \rho(z_{i,j}, z_{i,l}), \tag{2.10}$$

where the first component on the right side is the auto-correlation and the second is the cross-correlation. The third type of correlation $\rho(z_{i,l}, z_{k,j})$ can be written in another form, i.e.

$$\rho(z_{i,l}, z_{k,j}) = \rho(z_{i,l}, z_{k,l}) \cdot \rho(z_{k,j}, z_{k,l}). \tag{2.11}$$

Because the auto-correlation is determined only by the distance between targets $d_{i,k}$, the auto-correlation component in the two equation are equal. However, according to (2.8) and (2.9), the cross-correlation is determined by the ADOA, which might have significant differences depending on the location of targets and base station.

For localisation scenarios, one way to adopt Graziosi's model is to generate the third type of correlation in a consistent manner, e.g., use the cross-correlation component of targets with smaller indices. An alternative explanation is that when the distance between targets are much smaller than propagation distance, the ADOA for the targets only have a minor difference and thus the cross-correlation can be seen as equal.

2.5 Summary

This chapter first categorises the localisation systems topologies depending on which part needs to be localised and where the algorithm is processed. Afterwards, the chapter reviews several standard positioning algorithms including proximity positioning, triangulation, trilateration and multilateration as well as the corresponding

measurements.

Then, RSS fingerprinting localisation is introduced. The fingerprinting method involves an offline data collection phase and online localisation phase. Deterministic framework and probabilistic framework for localisation phase are studied. For the offline phase, a short survey of RSS fingerprint interpolation is presented.

At last, the RSS shadowing attenuation and three types of shadowing correlation are reviewed.

Chapter 3

Indoor RSS Fingerprints Interpolation Using Kriging Methods

The ranging based localisation method, such as trilateration and multilateration, would suffer in outdoor dense building area or typical indoor environments. An alternative solution is the fingerprinting, which locates a target through feature matching. More precisely, in the offline preparation phase, a type of location feature (fingerprints), such as RSS, is measured and collected for all predefined points in the area. Later in the positioning phase, the target measurement is compared with all existing location features. The final target location is estimated based on the comparison/matching result.

The localisation accuracy of fingerprinting method depends essentially on the density of predefined points. In other words, the more data points are exploited in the offline phase, the better positioning accuracy would be achieved. However, the feature collection is time-consuming and laborious. Especially where there are environmental changes, fingerprints over the area might alter significantly. In that case, an efficient way of maintaining the fingerprint database is beneficial.

In this chapter, an advanced interpolation method, the Kriging method, is pro-

posed to improve the efficiency of the offline work. Specifically, the workload of data collection can be obviously reduced because not all but only a few location features at sparsely distributed grid points are required, and unmeasured features can be estimated from surrounding data points. Compared with other standard interpolation methods, such as the k-nearest neighbours (kNN) and inverse distance weighted (IDW) method, the Kriging method exploits the spatial correlation of data. The simulation and real data experiments show that the proposed Kriging methods improve the fingerprints estimation and further yield better localisation accuracy.

The chapter will be organised as follows: first, geostatistics and Kriging methods are introduced including necessary theoretical details. Then, simulation results are shown and discussed. The real data experiments are presented after. A summary of the chapter is given at last.

3.1 Kriging Interpolation

Natural phenomena, such as ore grades, humidity or smog, are the product of many interacting physical, chemical or biological processes. Because of the incomplete understanding of the processes and the complexity of their interaction, there are no good models that characterise these processes available [52]. By employing statistics tools, *geostatistics* offers a way to model the spatial correlation of natural phenomena and provides adaptations of classical regression techniques to take advantage of this spatial correlation [53].

A central problem of geostatistics is the reconstruction of the phenomenon through estimating values at unknown locations based on observations at a limited number of points. Mathematically this problem can be regarded as spatial interpolation problem [54]. A formal analogy is provided by the prediction problem in time series: given values of the past, usually at regular time intervals, the task is to predict the value of the signal at some time in the future. First, the signal is analysed, typically by computing and modelling the spectrum, and then a predictor is proposed. Geostatistics follows a similar approach but in the spatial setting.

The spatial interpolation method is called the *Kriging* method, which refers to a group of least-squared based interpolation methods. It is named after Danie G. Krige, who developed empirically statistical methods to predict ore grades from spatially correlated sample data in the gold mines of South Africa [52].

The standard routine of Kriging method consists of spatial model analysis and data interpolation. Following the routine, the Kriging method will be introduced in details.

3.1.1 Spatial Model Analysis

3.1.1.1 Covariance function and Variogram

Similar to spectrum and covariance analysis in time series, a spatial model is required to produce estimations. The idea of modelling the natural phenomena as they are spatially random is initiated by Matheron in [55].

Given an area of interest $\mathcal{G} \subset \mathrm{R}^2$, the value of a spatial phenomenon at a location $\mathbf{p}$ is regarded as a random variable $Z(\mathbf{p})$. Overall, the phenomenon in the area can be characterised by a *random field*, which is a collection of spatial random variables $\{Z(\mathbf{p}) \mid \mathbf{p} \in \mathcal{G}\}$.

Typically, to compute statistics and draw inferences of the random field, multiple observations at each location are required. However, referring to some natural phenomena, such as ore grades, difficulties arise because at each location there is only one observation. To overcome this problem, further assumptions are required, i.e. stationarity.

The stationarity implies that the statistics of the random filed $\{Z(\mathbf{p}) \mid \mathbf{p} \in \mathcal{G}\}$ are spatially invariant. For example, *second order stationarity* implies that the expected value over random field is constant and the covariance of two random variables $Z(\mathbf{p}_i)$ and $Z(\mathbf{p}_j)$ depends only on the separation distance $\|\mathbf{p}_i - \mathbf{p}_j\|$, that is

$$\mathbb{E}[\mathbf{p}] = \mu, \tag{3.1a}$$

$$\mathrm{Cov}(Z(\mathbf{p}_i), Z(\mathbf{p}_j)) = \mathbb{E}\Big[\big(Z(\mathbf{p}_i) - \mu\big)\big(Z(\mathbf{p}_j) - \mu\big)\Big] = C(\|\mathbf{p}_i - \mathbf{p}_j\|) = C(h), \tag{3.1b}$$

where μ is the constant expected value, $C(\cdot)$ is the spatial covariance function, and h is called *lag* (following the manner in time series), which represents the separation distance $\|\mathbf{p}_i - \mathbf{p}_j\|$. Thus, under the assumption of the second order stationarity, a random field can be completed characterised by the constant expected value and covariance function.

Although the second order stationarity is known as *weak-sense stationarity* in time series analysis, it is still a strong requirement in spatial analysis. In geostatistics, a weaker assumption is more widely used, namely *intrinsic stationarity* [56].

By adopting a new random variable, i.e. $\delta(\mathbf{p}_i, \mathbf{p}_j) = Z(\mathbf{p}_i) - Z(\mathbf{p}_j)$, the intrinsic stationarity implies that: within a local area $g \subset \mathcal{G}$ ($\mathbf{p}_i, \mathbf{p}_j \in g$), the expected value of $\delta(\mathbf{p}_i, \mathbf{p}_j)$ is zero and the variance of $\delta(\mathbf{p}_i, \mathbf{p}_j)$ depends only on the separation distance $\|\mathbf{p}_i - \mathbf{p}_j\|$, i.e.

$$\mathbb{E}[\delta(\mathbf{p}_i, \mathbf{p}_j)] = 0, \tag{3.2a}$$

$$\mathrm{Var}(\delta(\mathbf{p}_i, \mathbf{p}_j)) = \mathbb{E}[\delta(\mathbf{p}_i, \mathbf{p}_j)]^2 = 2\gamma(\|\mathbf{p}_i - \mathbf{p}_j\|) = 2\gamma(h), \tag{3.2b}$$

where $\gamma(\cdot)$ is called *variogram*, which is an alternative form of spatial correlation model. Thus, under the intrinsic stationarity, a random field can be completed characterised by the variogram.

Comparing (3.1b) and (3.2b), the covariance function is a measure of the similarity between random variables, while the variogram is a measure of dissimilarity [57]. Under some conditions, the two functions can have certain quantitative relations, which will be shown later. Moreover, the intrinsic stationarity is "weaker" than the second order stationarity in the sense of that the property is restricted in "local area" rather than over the whole area.

3.1.1.2 Obtain the Variogram

Similarly to the time series analysis, the variogram is obtained through regression analysis. According to (3.2b), the independent variable for the correlation model is the lag h, which is determined by the separation distance between two data

points rather than the actual locations. The dependent variable equals to half of the variance of $\delta(\mathbf{p}_i, \mathbf{p}_j)$. Therefore, given a data set $\{z(\mathbf{p}_1), z(\mathbf{p}_2), \ldots\}$, the first objective is to calculate the sample variances of $\delta(\mathbf{p}_i, \mathbf{p}_j)$ as a function of lag h.

Specifically, differences between all possible pairs of data points, i.e. $\delta(\mathbf{p}_i, \mathbf{p}_j)$ (where $i, j = 1, 2, \ldots$), are calculated at first. After setting lag intervals h, the differences are "thrown into bins" according to the their separation distances/lags. For convenience, the total number of difference values in the bin of a certain lag h is denoted by $N(h)$, where the i-th difference value is denoted by $\delta_i(h)$ $(i = 1, \ldots, N(h))$. Then, the so called *empirical variogram* (or *experimental variogram*), which are the half sample variances of $\delta(\mathbf{p}_i, \mathbf{p}_j)$, are calculated as

$$\hat{\gamma}(h) = \frac{1}{2} \times \frac{1}{N(h)} \sum_{i=1}^{N(h)} \big(\delta_i(h)\big)^2, \tag{3.3}$$

An example of variogram is shown in Figure 3.4.

The next step is to fit in a model as the final variogram function using the classic regression method, e.g. least square regression [56], [58]. The model is usually chosen from several possible options, as given below [52]

Spherical Model:

$$\gamma(h) = \begin{cases} 0 & \text{for } h = 0 \\ C_0 + C\Big\{\dfrac{3h}{2d_c} - \dfrac{1}{2}\Big(\dfrac{h}{d_c}\Big)^3\Big\} & \text{for } 0 < h \le d_c \\ C_0 + C & \text{for } h > d_c \end{cases} \tag{3.4}$$

Exponential Model:

$$\gamma(h) = \begin{cases} 0 & \text{for } h = 0 \\ C_0 + C\Big\{1 - \exp\Big(-\dfrac{3h}{d_c}\Big)\Big\} & \text{for } h > 0 \end{cases} \tag{3.5}$$

Gaussian Model:

$$\gamma(h) = \begin{cases} 0 & \text{for } h = 0 \\ C_0 + C\Big\{1 - \exp\Big(-\dfrac{3h^2}{d_c^2}\Big)\Big\} & \text{for } h > 0 \end{cases} \tag{3.6}$$

Power Model:

$$\gamma(h) = \begin{cases} 0 & \text{for } h = 0 \\ C_0 + C \cdot h^a \ (0 < a < 2) & \text{for } h > 0 \end{cases} \tag{3.7}$$

where C_0 represents the nugget component, and d_c is the decorrelation range. The value $C_0 + C$ is known as the *sill*.

According to [57], since there is no explicit criterion, the selection of the best fitted model can be flexible. Moreover, linear combinations of the above models are considered licit.

3.1.2 Kriging Interpolation

The Kriging interpolation method refers to a group of least square based methods [59]. Given a dataset $\{z(\mathbf{p}_1), z(\mathbf{p}_2), \ldots\}$, the Kriging estimates the value at an unmeasured location $\mathbf{p}_0$ as a weighted sum of surrounding data points, i.e.

$$\bar{z}(\mathbf{p}_0) = \sum_{i=1}^{k} \lambda_i z(\mathbf{p}_i), \tag{3.8}$$

where k is the number of data points in the local neighbourhood of $\mathbf{p}_0$, and $\lambda_i (i = 1 \cdots k)$ are the Kriging weights. The Kriging weights are derived through minimising the variance of estimator error

$$\min_{\lambda_i \in R} \mathrm{Var}(\bar{z}(\mathbf{p}_0) - z(\mathbf{p}_0)), \tag{3.9}$$

under the unbiasedness constraint

$$\mathbb{E}[\bar{z}(\mathbf{p}_0) - z(\mathbf{p}_0)] = 0, \tag{3.10}$$

where $z(\mathbf{p}_0)$ represent the true value at location $\mathbf{p}_0$.

There are three commonly used Kriging methods, namely *simple Kriging*, *ordinary Kriging* and *universal Kriging*. The simple Kriging method adopts an assumption that the expected value of $z(\mathbf{p})$ is a known constant over the whole area, which is too strong for RSS value interpolation. Therefore the simple Kriging method is not considered. The ordinary Kriging and universal Kriging are introduced here.

In the following derivation, for conciseness, the variables are abbreviated as

$$z(\mathbf{p}_i) \Rightarrow z_i, \tag{3.11a}$$

$$\bar{z}(\mathbf{p}_0) \Rightarrow \bar{z}_0, \tag{3.11b}$$

$$\gamma(\|\mathbf{p}_i - \mathbf{p}_j\|) \Rightarrow \gamma_{i,j}. \tag{3.11c}$$

3.1.2.1 Ordinary Kriging

In case that the expected value of $Z(\mathbf{p})$ over the whole area is not a constant and is unknown, the ordinary Kriging introduces a weaker assumption that is equivalent to the intrinsic stationarity: within the local neighbourhood of $\mathbf{p}_0$, the expected value of $Z(\mathbf{p})$ is unknown but is a constant, denoted by $\mu(\mathbf{p}_0)$, i.e.

$$\mathbb{E}[Z(\mathbf{p})] = \mu(\mathbf{p}_0). \tag{3.12}$$

Therefore, substituting the Kriging estimate in the unbiasedness constraint (3.10) with (3.8), it can be further derived as

$$\mathbb{E}[\bar{z}_0 - z_0] = \mathbb{E}\left[\sum_{i=1}^{k} \lambda_i z_i - z_0\right] \tag{3.13a}$$

$$= \sum_{i=1}^{k} \lambda_i \mathbb{E}[Z_i] - \mathbb{E}[z_0] \tag{3.13b}$$

$$= \sum_{i=1}^{k} \lambda_i \mu - \mu = 0. \tag{3.13c}$$

As an equivalent unbiasedness constraint, the Kriging weights should be subject to

$$\sum_{i=1}^{k} \lambda_i = 1. \tag{3.14}$$

The error variance in (3.9) can be derived as

$$\begin{aligned}
\mathrm{Var}(\bar{z}_0 - z_0) &= \mathbb{E}[\bar{z}_0 - z_0]^2 && \text{(3.15a)}\\
&= \mathbb{E}\Big[\sum_{i=1}^{k} \lambda_i z_i - z_0\Big]^2 && \text{(3.15b)}\\
&= \mathbb{E}\Big[\sum_{i=1}^{k} \lambda_i z_i - \sum_{i=1}^{k} \lambda_i z_0\Big]^2 && \text{(3.15c)}\\
&= \mathbb{E}\Big[\sum_{i=1}^{k} \lambda_i \big(z_i - \bar{z}_0\big)\Big]^2 && \text{(3.15d)}\\
&= \mathbb{E}\Big[\sum_{i=1}^{k}\sum_{j=1}^{k} \lambda_i\lambda_j \big(z_i - \bar{z}_0\big)\big(z_j - \bar{z}_0\big)\Big] && \text{(3.15e)}\\
&= \mathbb{E}\Big[\sum_{i=1}^{k}\sum_{j=1}^{k} \lambda_i\lambda_j \Big\{\frac{1}{2}\big(z_i - \bar{z}_0\big)^2 + \frac{1}{2}\big(z_j - \bar{z}_0\big)^2 - \frac{1}{2}\big(z_i - z_j\big)^2\Big\}\Big] && \text{(3.15f)}\\
&= \sum_{i=1}^{k}\sum_{j=1}^{k} \lambda_i\lambda_j \Big\{\frac{1}{2}\mathbb{E}\big[z_i - \bar{z}_0\big]^2 + \frac{1}{2}\mathbb{E}\big[z_j - \bar{z}_0\big]^2 - \frac{1}{2}\mathbb{E}\big[z_i - z_j\big]^2\Big\} && \text{(3.15g)}\\
&= 2 \cdot \sum_{i=1}^{k} \lambda_i \Big\{\frac{1}{2}\mathbb{E}\big[z_i - \bar{z}_0\big]^2\Big\} - \sum_{i=1}^{k}\sum_{j=1}^{k} \lambda_i\lambda_j \Big\{\frac{1}{2}\mathbb{E}\big[z_j - z_0\big]^2\Big\} && \text{(3.15h)}\\
&= 2 \cdot \sum_{i=1}^{k} \lambda_i \gamma_{i,0} - \sum_{i=1}^{k}\sum_{j=1}^{k} \lambda_i\lambda_j \gamma_{i,j}, && \text{(3.15i)}
\end{aligned}$$

where from (3.15g) to (3.15h), the equivalent components that have different indexing variables are merged under (3.14), i.e.

$$\sum_{i=1}^{k}\sum_{j=1}^{k} \lambda_i\lambda_j \Big\{\frac{1}{2}\mathbb{E}\big[z_i - \bar{z}_0\big]^2 + \frac{1}{2}\mathbb{E}\big[z_j - \bar{z}_0\big]^2\Big\}$$

$$= \sum_{j=1}^{k} \lambda_j \Bigg(\sum_{i=1}^{k} \lambda_i \Big\{ \frac{1}{2} \mathbb{E}\big[z_i - \bar{z}_0 \big]^2 \Big\} \Bigg) + \sum_{i=1}^{k} \lambda_i \Bigg(\sum_{j=1}^{k} \lambda_j \Big\{ \frac{1}{2} \mathbb{E}\big[z_j - \bar{z}_0 \big]^2 \Big\} \Bigg) \tag{3.16a}$$

$$= 2 \cdot \sum_{i=1}^{k} \lambda_i \Big\{ \frac{1}{2} \mathbb{E}\big[z_i - \bar{z}_0 \big]^2 \Big\}, \tag{3.16b}$$

and from (3.15h) to (3.15i), the half expected values are substituted with the variogram values according to (3.2b) under the unbiasedness condition (3.10), i.e.

$$\gamma_{i,j} = \frac{1}{2} \mathrm{Var}(\delta(\mathbf{p}_i - \mathbf{p}_j)) \tag{3.17a}$$

$$= \frac{1}{2} \mathrm{Var}(z_i - z_j) \tag{3.17b}$$

$$= \frac{1}{2} \mathbb{E}[z_i - z_j]^2. \tag{3.17c}$$

To minimise the variance of Kriging estimate error subject to the constraints (3.14), the *Lagrange multiplier* optimisation method is adopted. By introducing a Lagrange multiplier l, the new objective is given by

$$\min_{\lambda_i \in R} 2 \cdot \sum_{i=1}^{k} \lambda_i \gamma_{i,0} - \sum_{i=1}^{k} \sum_{j=1}^{k} \lambda_i \lambda_j \gamma_{i,j} + 2l \cdot \Bigg(\sum_{i=1}^{k} \lambda_i - 1 \Bigg), \tag{3.18}$$

Taking the partial differentials of (3.15i) with respect to each Kriging weights and the Lagrange multiplier, and then making them equal to zero, there results in a set of equations, i.e.

$$\begin{cases} \sum_{j=1}^{k} \lambda_j \gamma_{1,j} + l = \gamma_{1,0} \\ \qquad \vdots \\ \sum_{j=1}^{k} \lambda_j \gamma_{k,j} + l = \gamma_{k,0} \\ \sum_{i=1}^{k} \lambda_i = 1 \end{cases}. \tag{3.19}$$

Rewrite the equation set into matrix form, that is

$$\begin{pmatrix} \gamma_{1,1} & \cdots & \gamma_{1,k} & 1 \\ \vdots & \ddots & \vdots & \vdots \\ \gamma_{k,1} & \cdots & \gamma_{k,k} & 1 \\ 1 & \cdots & 1 & 0 \end{pmatrix} \begin{pmatrix} \lambda_1 \\ \vdots \\ \lambda_k \\ l \end{pmatrix} = \begin{pmatrix} \gamma_{1,0} \\ \vdots \\ \gamma_{k,0} \\ 1 \end{pmatrix}. \tag{3.20}$$

Thus, the optimised Kriging weights are given by

$$\begin{pmatrix} \lambda_1 \\ \vdots \\ \lambda_k \\ l \end{pmatrix} = \begin{pmatrix} \gamma_{1,1} & \cdots & \gamma_{1,k} & 1 \\ \vdots & \ddots & \vdots & \vdots \\ \gamma_{k,1} & \cdots & \gamma_{k,k} & 1 \\ 1 & \cdots & 1 & 0 \end{pmatrix}^{-1} \begin{pmatrix} \gamma_{1,0} \\ \vdots \\ \gamma_{k,0} \\ 1 \end{pmatrix}. \tag{3.21}$$

Finally, given the data points in the neighbourhood $\{z_1, \ldots, z_k\}$ and corresponding variogram function $\gamma(h)$, the value at location $\mathbf{p}_0$ is given by

$$\bar{z}_0 = \sum_{i=1}^{k} \lambda_i z_i, \tag{3.22}$$

Multiply λ_i to the i-th equation in (3.19) and sum up the first k equations, it gives

$$\sum_{i=1}^{k} \lambda_i \left(\sum_{j=1}^{k} \lambda_i \lambda_j \gamma_{i,j} + l \right) = \sum_{i=1}^{k} \lambda_i \gamma_{i,0}, \tag{3.23a}$$

$$\Rightarrow \quad \sum_{i=1}^{k} \sum_{j=1}^{k} \lambda_i \lambda_j \gamma_{i,j} = \sum_{i=1}^{k} \lambda_i \gamma_{i,0} - l. \tag{3.23b}$$

Therefore, the Kriging variance, which is the minimised estimate error variance in (3.9), can be further derived from (3.15i) as

$$\mathrm{Var}(\bar{z}_0 - z_0) = 2 \cdot \sum_{i=1}^{k} \lambda_i \gamma_{i,0} - \sum_{i=1}^{k} \sum_{j=1}^{k} \lambda_i \lambda_j \gamma_{i,j} \tag{3.24a}$$

$$= \sum_{i=1}^{k} \lambda_i \gamma_{i,0} + l. \tag{3.24b}$$

3.1.2.2 Universal Kriging

The universal Kriging can be seen as an enhanced version of ordinary Kriging method, in the sense of that it applies to more general scenarios where the expected value of $Z(\mathbf{p})$ can have obvious trends. More precisely, the random variable $Z(\mathbf{p})$ can be decomposed as

$$Z(\mathbf{p}) = \mu(\mathbf{p}) + R(\mathbf{p}), \tag{3.25}$$

where $\mu(\mathbf{p})$ represents the *trend*, and $R(\mathbf{p})$ represents the *residual* which is modelled as a zero expected value random field variable, i.e.

$$\mathbb{E}[R(\mathbf{p})] = 0. \tag{3.26}$$

The function of trend can be further modelled as a linear combination of known functions but with unknown coefficients, i.e.

$$\mu(\mathbf{p}) = \beta_1 \varphi_1(\mathbf{p}) + \beta_1 \varphi_2(\mathbf{p}) + \cdots, \tag{3.27}$$

where $\beta_1, \beta_2, \ldots$ are the unknown linear coefficients, and $\varphi_1(\mathbf{p}), \varphi_2(\mathbf{p}), \ldots$ are the known functions. In the following derivation part, a trend consisting of 2 components will be taken as example, that is

$$\mu(\mathbf{p}) = \beta_1 \varphi_1(\mathbf{p}) + \beta_1 \varphi_2(\mathbf{p}) \tag{3.28a}$$

$$= \sum_{\tau=1}^{2} \beta_\tau \varphi_\tau(\mathbf{p}). \tag{3.28b}$$

Different from the simple Kriging and ordinary Kriging method that are based

on the spatial correlation of the entire value $Z(\mathbf{p})$, the universal Kriging relies on the spatial correlation of the residual component $R(\mathbf{p})$. In such cases, the variogram that characterises the random field $\{R(\mathbf{p}) \mid \mathbf{p} \in \mathcal{G}\}$ should be established on the residual data set $\{r(\mathbf{p}_1), r(\mathbf{p}_2), \ldots\}$ so that it is termed as *residual variogram*. As preliminaries, obtaining the residual data set could adopt different approaches in the context of applications. For convenience, the residual variogram will be denoted as same as $\gamma(h)$ and $\gamma_{i,j}$ in the previous section.

Similarly, the universal Kriging estimates the value at an unmeasured location $\mathbf{p}_0$ as a weighted sum of surrounding data points, i.e.

$$\bar{z}_0 = \sum_{i=1}^{k} \lambda_i z_i \tag{3.29a}$$

$$= \sum_{i=1}^{k} \lambda_i \Big(\sum_{\tau=1}^{2} \beta_\tau \varphi_\tau(\mathbf{p}_i) + r_i \Big), \tag{3.29b}$$

where r_i is the short hand for $r(\mathbf{p}_i)$. Again, the Kriging weights are optimised through minimising the estimate error variance under the unbiasedness condition, as described in (3.8) and (3.10).

Substitute the estimate in the unbiasedness constraint (3.10) with the universal Kriging estimate (3.29b), it can be derived as

$$\mathbb{E}[\bar{z}_0 - z_0] = \mathbb{E}\left[\sum_{i=1}^{k} \lambda_i \Big(\sum_{\tau=1}^{2} \beta_\tau \varphi_\tau(\mathbf{p}_i) + r_i \Big) - \Big(\sum_{\tau=1}^{2} \beta_\tau \varphi_\tau(\mathbf{p}_0) + r_0 \Big) \right] \tag{3.30a}$$

$$= \mathbb{E}\left[\sum_{i=1}^{k} \lambda_i \sum_{\tau=1}^{k} \beta_\tau \varphi_\tau(\mathbf{p}_i) - \sum_{\tau=1}^{2} \beta_\tau \varphi_\tau(\mathbf{p}_0) \right] + \mathbb{E}\left[\sum_{i=1}^{k} \lambda_i r_i - r_0 \right] \tag{3.30b}$$

$$= \sum_{\tau=1}^{2} \beta_\tau \left\{ \mathbb{E}\Big[\sum_{i=1}^{k} \lambda_i \varphi_\tau(\mathbf{p}_i) - \varphi_\tau(\mathbf{p}_0) \Big] \right\} \tag{3.30c}$$

$$= 0, \tag{3.30d}$$

which lead to an equivalent equation set, i.e.

$$\begin{cases} \sum_{i=1}^{k} \lambda_i \varphi_1(\mathbf{p}_i) - \varphi_1(\mathbf{p}_0) = 0 \\ \sum_{i=1}^{k} \lambda_i \varphi_2(\mathbf{p}_i) - \varphi_2(\mathbf{p}_0) = 0 \end{cases} \tag{3.31}$$

In order to repeat part of the derivation in ordinary section, select the first function $\varphi_1(\mathbf{p})$ always equals to 1, which gives the similar conclusion as (3.14), i.e.

$$\varphi_1(\mathbf{p}) = 1 \quad \Rightarrow \quad \sum_{i=1}^{k} \lambda_i = 1. \tag{3.32}$$

Taking advantage of derivations in (3.30) and (3.15), the estimate error variance can be derived as

$$\begin{aligned} \mathrm{Var}(\bar{z}_0 - z_0) &= \mathbb{E}[\bar{z}_0 - z_0]^2 && \text{(3.33a)} \\ &= \mathbb{E}\left[\sum_{\tau=1}^{k} \beta_\tau \left(\sum_{i=1}^{k} \lambda_i \varphi_\tau(\mathbf{p}_i) - \varphi_\tau(\mathbf{p}_0) \right) + \left(\sum_{i=1}^{k} \lambda_i r_i - r_0 \right) \right]^2 && \text{(3.33b)} \\ &= \mathbb{E}\left[\sum_{i=1}^{k} \lambda_i r_i - r_0 \right]^2 && \text{(3.33c)} \\ &= 2 \cdot \sum_{i=1}^{k} \lambda_i \left\{ \frac{1}{2} \mathbb{E}\big[r_i - \bar{r}_0 \big]^2 \right\} - \sum_{i=1}^{k} \sum_{j=1}^{k} \lambda_i \lambda_j \left\{ \frac{1}{2} \mathbb{E}\big[r_j - r_0 \big]^2 \right\} && \text{(3.33d)} \\ &= 2 \cdot \sum_{i=1}^{k} \lambda_i \gamma_{i,0} - \sum_{i=1}^{k} \sum_{j=1}^{k} \lambda_i \lambda_j \gamma_{i,j}, && \text{(3.33e)} \end{aligned}$$

where from (3.33b) to (3.33c), the first term in the expected value is eliminated according to the equation set (3.31).

Again, using the Lagrange multiplier optimisation, the task now is given by

$$\min_{\lambda_i \in R} 2 \cdot \sum_{i=1}^{k} \lambda_i \gamma_{i,0} - \sum_{i=1}^{k} \sum_{j=1}^{k} \lambda_i \lambda_j \gamma_{i,j} + 2 \cdot \sum_{\tau=1}^{2} l_\tau \left(\sum_{i=1}^{k} \lambda_i \varphi_\tau(\mathbf{p}_i) - \varphi_\tau(\mathbf{p}_0) \right), \tag{3.34}$$

where l_τ is the introduced Lagrange multiplier. Taking the partial differentials with respect to each Kriging weights and Lagrange multipliers, and then making them

equals to zero, there results in a set of equations, i.e

$$\begin{cases} \sum_{j=1}^{k} \lambda_j \gamma_{k,j} + \sum_{\tau=1}^{2} l_\tau \varphi_\tau(\mathbf{p}_1) = \gamma_{i,0} \\ \vdots \\ \sum_{j=1}^{k} \lambda_j \gamma_{k,j} + \sum_{\tau=1}^{2} l_\tau \varphi_\tau(\mathbf{p}_k) = \gamma_{k,0} \\ \sum_{i=1}^{k} \lambda_i \varphi_1(\mathbf{p}_i) - \varphi_1(\mathbf{p}_0) = 0 \\ \sum_{i=1}^{k} \lambda_i \varphi_2(\mathbf{p}_i) - \varphi_2(\mathbf{p}_0) = 0 \end{cases} \tag{3.35}$$

Rewrite (3.35) in matrix form, that is

$$\begin{pmatrix} \gamma_{1,1} & \cdots & \gamma_{1,k} & \varphi_1(\mathbf{p}_1) & \varphi_2(\mathbf{p}_1) \\ \vdots & \ddots & \vdots & \vdots & \vdots \\ \gamma_{k,1} & \cdots & \gamma_{k,k} & \varphi_1(\mathbf{p}_k) & \varphi_2(\mathbf{p}_k) \\ \varphi_1(\mathbf{p}_1) & \cdots & \varphi_1(\mathbf{p}_k) & 0 & 0 \\ \varphi_2(\mathbf{p}_k) & \cdots & \varphi_2(\mathbf{p}_k) & 0 & 0 \end{pmatrix} \begin{pmatrix} \lambda_1 \\ \vdots \\ \lambda_k \\ l_1 \\ l_2 \end{pmatrix} = \begin{pmatrix} \gamma_{1,0} \\ \vdots \\ \gamma_{k,0} \\ \varphi_1(\mathbf{p}_0) \\ \varphi_2(\mathbf{p}_0) \end{pmatrix} \tag{3.36}$$

Therefore, the optimised Kriging weights can be given by

$$\begin{pmatrix} \lambda_1 \\ \vdots \\ \lambda_k \\ l_1 \\ l_2 \end{pmatrix} = \begin{pmatrix} \gamma_{1,1} & \cdots & \gamma_{1,k} & \varphi_1(\mathbf{p}_1) & \varphi_2(\mathbf{p}_1) \\ \vdots & \ddots & \vdots & \vdots & \vdots \\ \gamma_{k,1} & \cdots & \gamma_{k,k} & \varphi_1(\mathbf{p}_k) & \varphi_2(\mathbf{p}_k) \\ \varphi_1(\mathbf{p}_1) & \cdots & \varphi_1(\mathbf{p}_k) & 0 & 0 \\ \varphi_2(\mathbf{p}_k) & \cdots & \varphi_2(\mathbf{p}_k) & 0 & 0 \end{pmatrix}^{-1} \begin{pmatrix} \gamma_{1,0} \\ \vdots \\ \gamma_{k,0} \\ \varphi_1(\mathbf{p}_0) \\ \varphi_2(\mathbf{p}_0) \end{pmatrix} \tag{3.37}$$

Multiply l_τ to the τ-th equation in (3.31) and sum together, it gives

$$\sum_{\tau=1}^{2} l_\tau \Big(\sum_{i=1}^{k} \lambda_i \varphi_\tau(\mathbf{p}_i) - \varphi_\tau(\mathbf{p}_0) \Big) = 0 \tag{3.38a}$$

$$\Rightarrow \quad \sum_{\tau=1}^{2} l_\tau \Big(\sum_{i=1}^{k} \lambda_i \varphi_\tau(\mathbf{p}_i) \Big) = \sum_{\tau=1}^{2} l_\tau \varphi_\tau(\mathbf{p}_0) \tag{3.38b}$$

$$\Rightarrow \quad \sum_{i=1}^{k} \lambda_i \Big(\sum_{\tau=1}^{2} l_\tau \varphi_\tau(\mathbf{p}_i) \Big) = \sum_{\tau=1}^{2} l_\tau \varphi_\tau(\mathbf{p}_0) \tag{3.38c}$$

where from (3.38b) to (3.38c) there is legit swap of the summation order on the left sides of equations. Further, multiply λ_i to the i-th equation in (3.35) and sum them together, it gives

$$\sum_{i=1}^{k} \lambda_i \Big(\sum_{j=1}^{k} \lambda_j \gamma_{i,j} + \sum_{\tau=1}^{2} l_\tau \varphi_\tau(\mathbf{p}_i) \Big) = \sum_{i=1}^{k} \lambda_i \gamma_{i,0} \tag{3.39a}$$

$$\Rightarrow \quad \sum_{i=1}^{k} \sum_{j=1}^{k} \lambda_i \lambda_j \gamma_{i,j} = \sum_{i=1}^{k} \lambda_i \gamma_{i,0} - \sum_{i=1}^{k} \lambda_i \Big(\sum_{\tau_1}^{2} l_\tau \varphi_\tau(\mathbf{p}_i) \Big) \tag{3.39b}$$

$$\Rightarrow \quad \sum_{i=1}^{k} \sum_{j=1}^{k} \lambda_i \lambda_j \gamma_{i,j} = \sum_{i=1}^{k} \lambda_i \gamma_{i,0} - \sum_{\tau=1}^{2} l_\tau \varphi_\tau(\mathbf{p}_0) \tag{3.39c}$$

Therefore, continuing the derivation of (3.33e), the universal Kriging estimate error variance is given by

$$\mathrm{Var}(\bar{z}_0 - z_0) = 2 \cdot \sum_{i=1}^{k} \lambda_i \gamma_{i,0} - \sum_{i=1}^{k} \sum_{j=1}^{k} \lambda_i \lambda_j \gamma_{i,j} \tag{3.40a}$$

$$= \sum_{i=1}^{k} \lambda_i \gamma_{i,0} + \sum_{\tau=1}^{2} l_\tau \varphi_\tau(\mathbf{p}_0) \tag{3.40b}$$

3.1.3 Advantages of Kriging Method

There are some noticeable advantages of the geostatistics tools:

- Comparing to other interpolation methods, e.g. linear interpolation and k-nearest neighbours, the Kriging methods take advantage of the correlation between data based on statistical analysis.

- The Kriging estimate is a best linear unbiased estimate.

- As consequences of utilising the spatial correlation, the Kriging method could compensate for the negative effects of data clustering. More precisely, data points from a compact cluster will be treated like a single data point because

the information provided from the cluster is redundant. Mathematically, data points from a cluster will be assign smaller weights that a signal point.

- The Kriging methods provide a statistic of estimate error, i.e. Kriging variance, which is helpful in evaluations such as the confidence interval.

3.2 Kriging of RSS Fingerprints

The RSS can be modelled as

$$z(\mathbf{p}) = f(\mathbf{p}) + \upsilon(\mathbf{p}) \quad \text{(in dB)}, \tag{3.41}$$

where $f(\mathbf{p})$ is the true value of RSS and is given by

$$f(\mathbf{p}) = P_t - L - 10\alpha \log_{10} d(\mathbf{p}), \tag{3.42}$$

and P_t is the transmitting power, L is the measured path loss at 1 meter away from the base station, $d(\mathbf{p})$ is the distance from the target to the base station, and $\upsilon(\mathbf{p})$ represents the shadowing effect which is assumed a zero-mean Gaussian distributed.

As described in the previous chapter, the shadowing effect is the consequence of the obstacles lying in the signal propagation path. By fixing the base station, the shadowing effects can be considered as related to the target location and therefore has spatial correlations. In such a sense, the interpolation methods can be considered here to estimate the signal strength at an unmeasured location.

However, the geostatistics tool has some disadvantages when applying to radio RSS estimation:

- **Spatial Model**: For the variogram established on the complete form $z(\mathbf{p})$, it is obvious that the expected value of the difference between two RSS could be non-zero, i.e.

$$\mathbb{E}[z(\mathbf{p}_i) - z(\mathbf{p}_j)] = -10\alpha \log_{10} d(\mathbf{p}_i) + 10\alpha \log_{10} d(\mathbf{p}_j) \tag{3.43a}$$

$$\neq 0, \text{ for } d(\mathbf{p}_i) \neq d(\mathbf{p}_j) \tag{3.43b}$$

Furthermore, the variance of the difference between the two RSS depends not only on the separation distance, i.e.

$$\mathrm{Var}(z(\mathbf{p}_i) - z(\mathbf{p}_j)) \neq 2\gamma(\|\mathbf{p}_i - \mathbf{p}_j\|). \tag{3.44}$$

Therefore, assuming the intrinsic stationarity as described in (3.2) for the RSS brings noticeable compromise.

For the residual variogram established on the shadowing component $\upsilon(\mathbf{p})$, the intrinsic stationarity can be adopted when considers the shadowing autocorrelation taking the form of Gudmundson's model [43]. However, the shadowing components need to be extracted from the complete data, which requires preprocessing such as model regression and analysis of the data. Consequently, the quality of the residual variogram would highly depend on the preprocessing results.

- **Kriging Method**: For the ordinary Kriging method, the expected value of RSS has obvious trend, i.e.

$$\mathbb{E}[z(\mathbf{p})] = f(\mathbf{p}) = P_t - L - 10\alpha \log_{10} d(\mathbf{p}). \tag{3.45}$$

Thus, assuming the expected value of RSS is invariant in the local neighbourhood is another important compromise.

3.2.1 Ordinary Kriging

Given a data set $\{z(\mathbf{p}) \mid \mathbf{p} \in \mathcal{G}\}$, the steps of applying ordinary Kriging method to estimate unmeasured RSS fingerprints are given below:

1. Given a data set $\{z(\mathbf{p}) \mid \mathbf{p} \in \mathcal{G}\}$, assign all possible pairs of data points into bins according to the lag h. The range and intervals of lag can be selected

depending on the practice. Compute the empirical variogram as given in (3.3).

2. Take all models from (3.4) to (3.7), fit the models using the lease square regression method. Select the "best fitted" one as the final variogram model.

3. For an unmeasured location $\mathbf{p}_0$, select data points in the neighbourhood, i.e. $\{z_{\mathbf{p}_i} \mid \|\mathbf{p}_i - \mathbf{p}_0\| \leq d_c\}$, where d_c is the decorrelation range and is obtained found from the fitted variogram model.

4. Calculate the Kriging weights according to (3.21).

5. The Kriging estimate is given by (3.8), and the Kriging variance is given by (3.24b).

Once the variogram has been established, the steps 3, 4 and 5 shall be repeated for all unmeasured locations.

3.2.2 Universal Kriging

Given a data set $\{z(\mathbf{p}) \mid \mathbf{p} \in \mathcal{G}\}$, the preprocessing step and steps of universal Kriging method to estimate unmeasured RSS fingerprints are given below:

1. Given a data set $\{z(\mathbf{p}) \mid \mathbf{p} \in \mathcal{G}\}$, using least squares method to fit the model given in (3.42).

2. Adopt the fitted model in the previous step to extract the shadowing noise data set $\{\upsilon(\mathbf{p}) \mid \in \mathcal{G}\}$.

3. Assign all possible pairs of data points into bins according to specific range and intervals of lag lag. Compute the empirical variogram of the shadowing noise as given in (3.3).

4. Take all models from (3.4) to (3.7), fit the models using the lease square regression method. Select the "best fitted" one as the final residual variogram model.

5. Assuming the trend function as follows

$$f_1(\mathbf{p}) = 1, \tag{3.46a}$$

$$f_2(\mathbf{p}) = \log_{10} d(\mathbf{p}). \tag{3.46b}$$

6. For an unmeasured location $\mathbf{p}_0$, select shadowing noise of the data points in the neighbourhood, i.e. $\{v_{\mathbf{p}_i} \mid \|\mathbf{p}_i - \mathbf{p}_0\| \leq d_c\}$, where d_c is the decorrelation range and can be found from the fitted residual variogram model.

7. Calculate the Kriging weights according to (3.37).

8. The Kriging estimate is given by (3.8), and the Kriging variance is given by (3.40b).

The steps 6, 7 and 8 shall be repeated for all unmeasured locations.

3.3 Performance Validation and Evaluation

To validate the proposed approaches, both simulation and real-data experiment have been conducted. In simulations, RSS measurements including shadowing noise are generated and then compose a grid-based fingerprint database. Afterwards, some fingerprints are removed. The sampled (retained) fingerprints are used to estimate the missing entries through the IDW method, ordinary Kriging and universal Kriging methods. Interpolation and localisation results are studied against different sampling density. In the real-data experiment, the RSS measurements are collected in the room D10 of Amy Johnson building, University of Sheffield. Following the similar manner, some RSS fingerprints are removed and then estimated based on the sampled entries. Only interpolation result analysis is presented

3.3.1 Simulation Results

Figure 3.1 depicts the basic setup for simulation, there are 5 base stations deployed in a 25m $\times$ 25m area. The area is divided into 50×50 grids where each grid is of

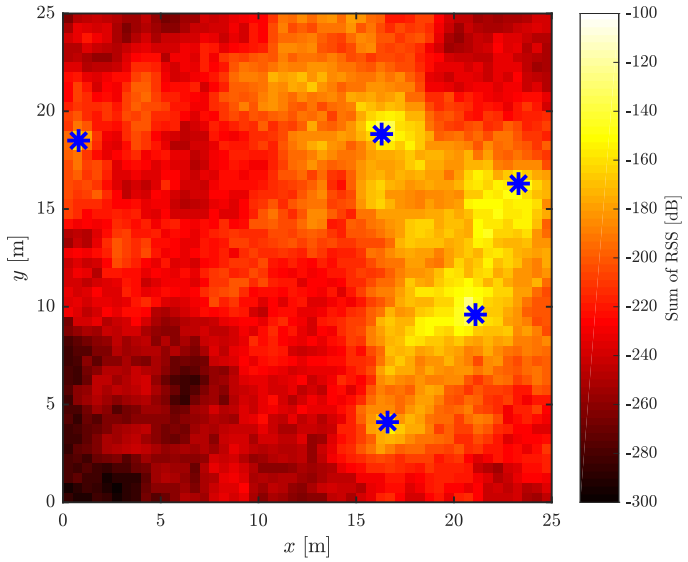

Figure 3.1: Aggregated RSS map for all base stations. The blue asterisks represent the base stations.

size 0.5m × 0.5m. For each grid, the fingerprints consist of 5 RSS measurements from different base stations.

An RSS measurement consists of a noise-free value generated according to the model (3.41), and the shadowing noise, where the shadowing effects are considered only auto-correlated (2.7) and are generated from a zero-mean multivariate Gaussian distribution. RSS measurements at all grid points is simulated and comprise a RSS

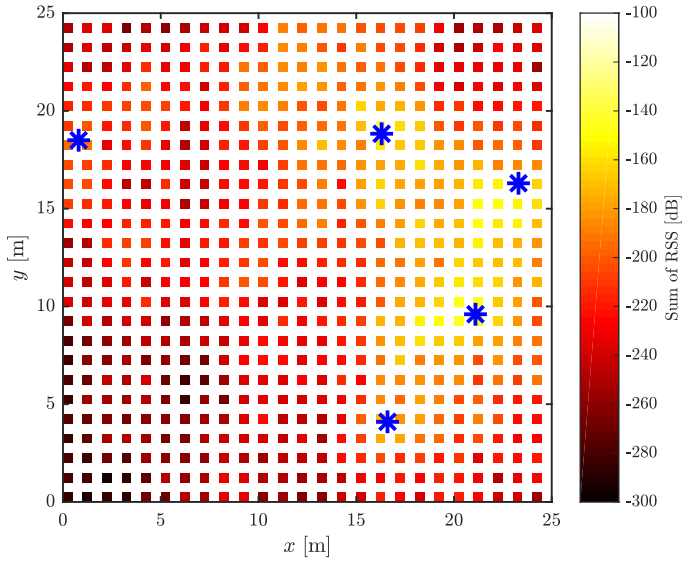

(a) 25 density% (625 reference points).

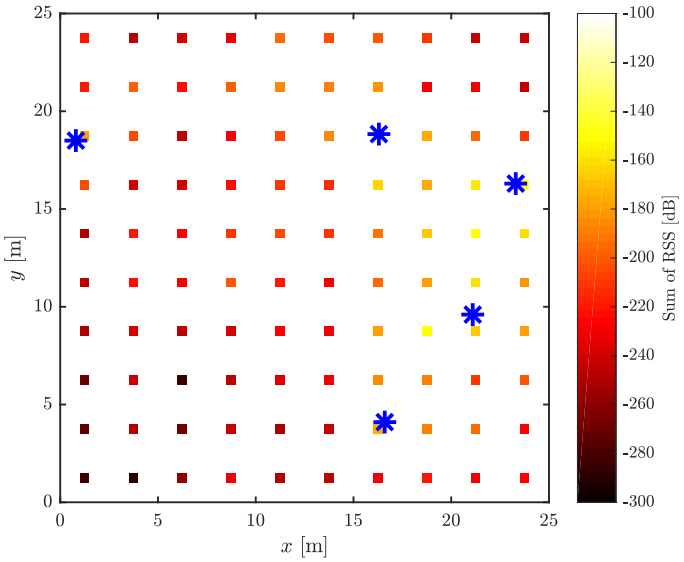

(b) 4% density (100 reference points).

Figure 3.2: Maps of fingerprint set with different density of reference points.

fingerprint database, where the i-th entry is given by

$$\{\mathbf{p}_i, \mathbf{z}_i\}, i = 1, 2, ... \tag{3.47}$$

where $\mathbf{p}_i = [x_{p,i}, y_{p,i}]^\mathsf{T}$ is the location of grid centre, $\mathbf{z}_i = [z_{i,1}, ..., z_{i,5}]^\mathsf{T}$ is the RSS measurement including the shadowing noises.

The objective here is to study interpolation and localisation performances with respect to the density of known data points. Thus, from the complete fingerprint

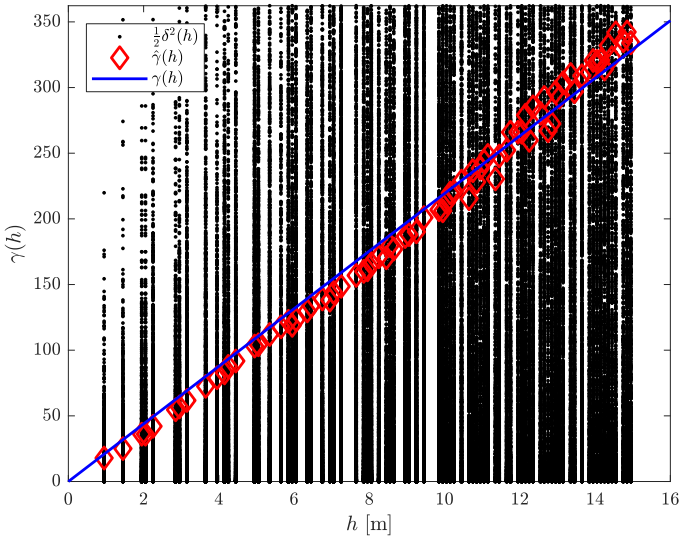

(a) 25% density.

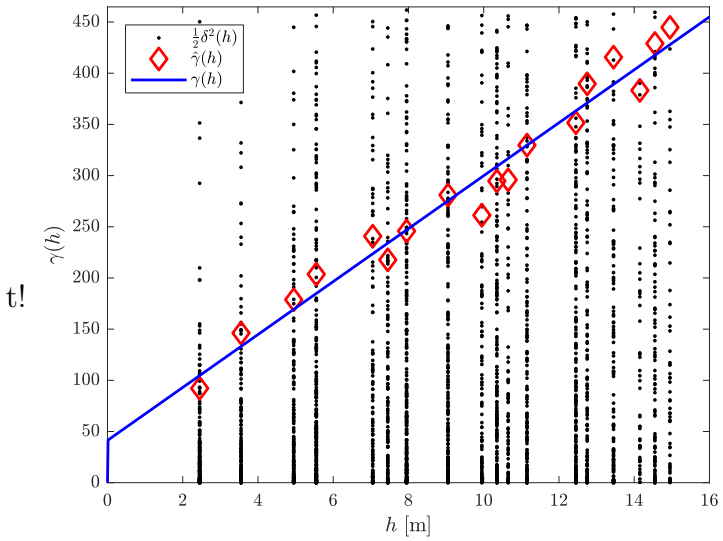

t!

(b) 4% density.

Figure 3.3: Ordinary Kriging variogram modelling for base station 1.

database, the "known" referencing set of entries are sampled following a uniform manner, while the rest are given as the "unknown" comparing set. As shown in Figure 3.2, four referencing sets with different densities are generated, which includes 625, 289, 169 and 100 reference points respectively.

Given a referencing set, the fingerprints of unknown/unmeasured locations are estimated/interpolated using the inverse distance weighting, OK and universal Kriging methods.

For the Kriging methods, spatial correlation modelling, which is the variogram

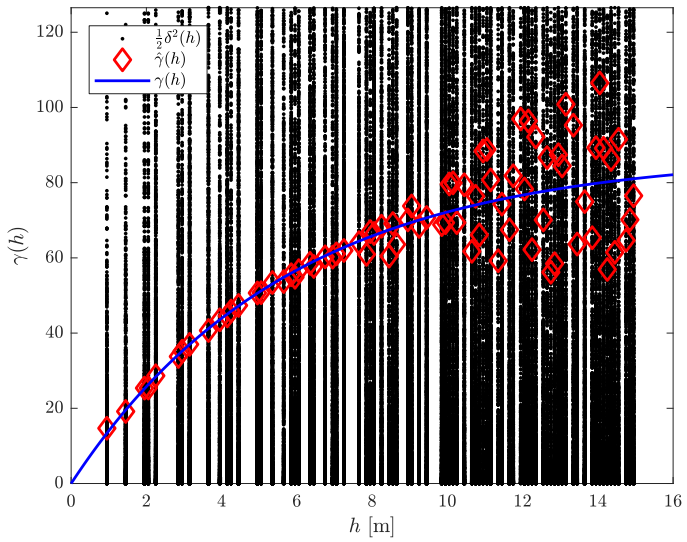

(a) 25% density.

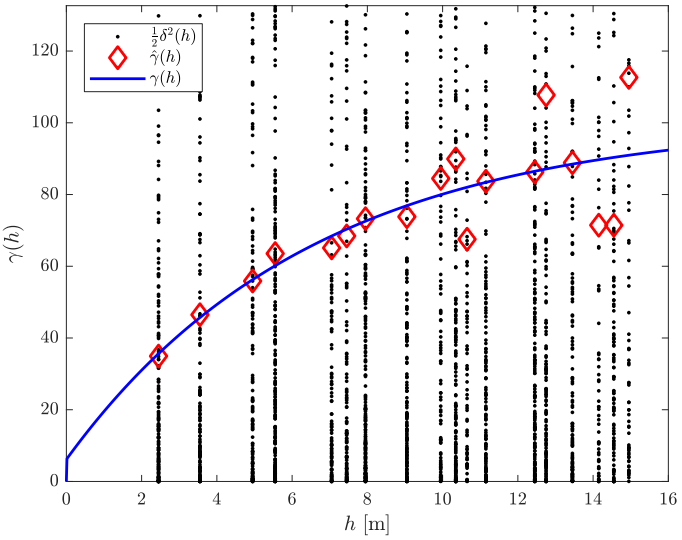

(b) 4% density.

Figure 3.4: Universal Kriging residual variogram modelling for base station 1.

modelling, is decisive to the interpolation quality. Figure 3.3 illustrates the variogram analysis for ordinary Kriging and Figure 3.4 demonstrates for the universal Kriging.

In each figure, the horizontal axis is the *lag* between two known data points, each black dot represents the half square of difference between a pair of data points, $\frac{1}{2}\delta^2(h)$; the red diamonds represent the empirical variogram values, which are the mean values of black dots; the solid blue line is the fitted exponential model (3.5). Though most of the black dots are concentrated around the corresponding mean

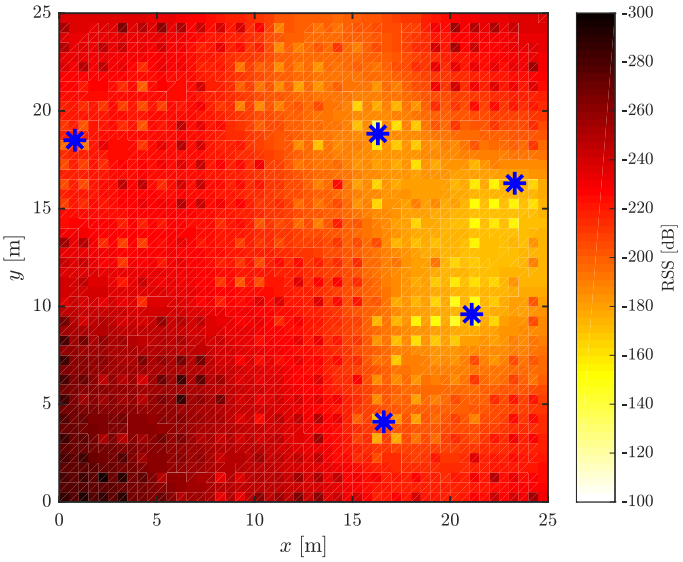

(a) 25% density.

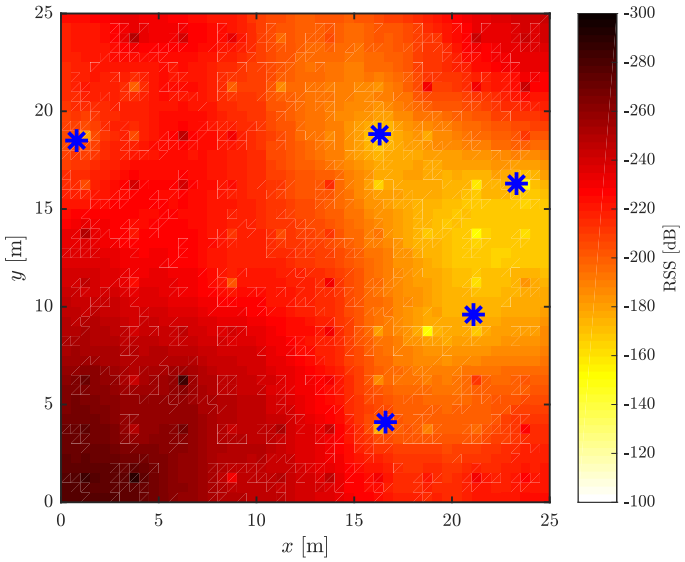

(b) 4% density.

Figure 3.5: IDW recovered map in simulation.

values (red diamonds), there are still data points that have significant deviations. The variogram is established on the mean values and characterises the most general qualities. It would lead to overestimate of the low bound and underestimate the upper bound when performing interpolations.

As shown in Figure 3.3, both variogram increase along with the lag h and are very similar to linear models. According to [56], this indicates obvious trends for the data. Noticing that these variograms are built on the entire value that includes

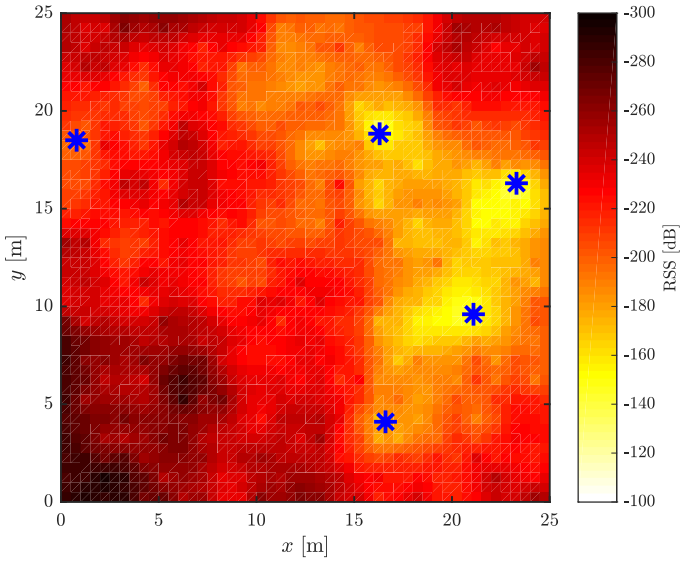

(a) 25% density.

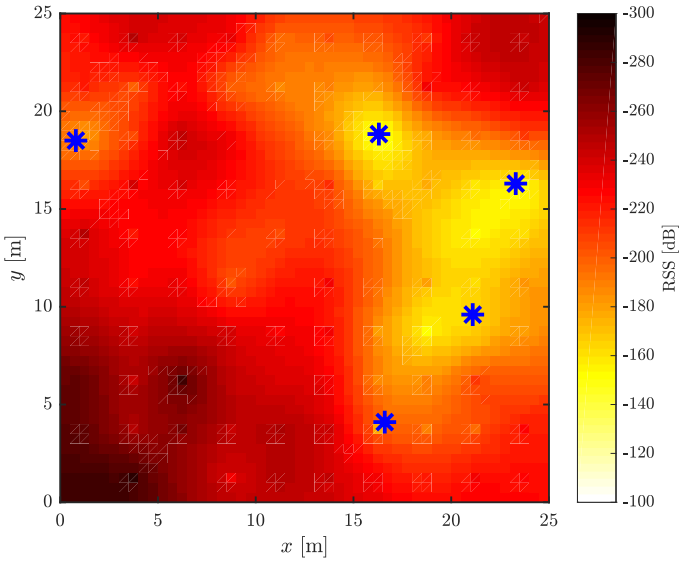

(b) 4% density.

Figure 3.6: Ordinary Kriging recovered map in simulation.

both the noise-free components and shadowing noise. The obvious trend is actually the result of the noise-free components.

As depicted in Figure 3.4, the residual modelling for universal Kriging, which has eliminated the "trend", is more meaningful than ordinary Kriging. The empirical variogram values converge to a certain profile when the lag is short, and begin to diverge after a certain distance, called decorrelation distance. In other words, the spatial correlation for residuals follow certain models when the distance between

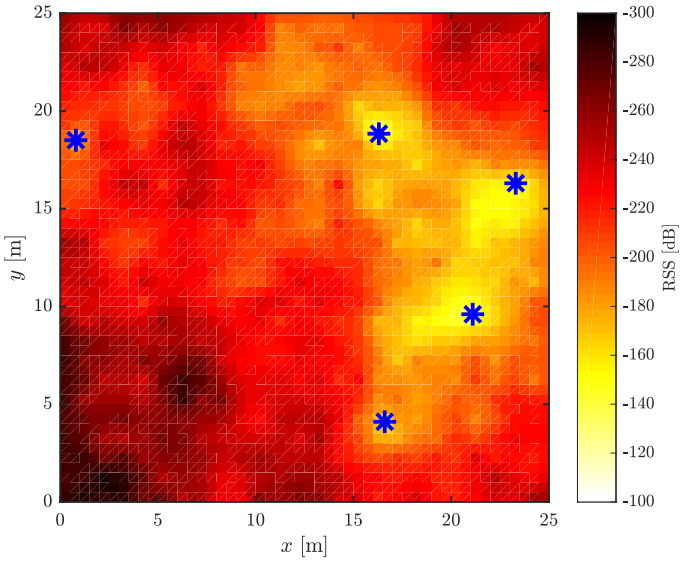

(a) 25% density.

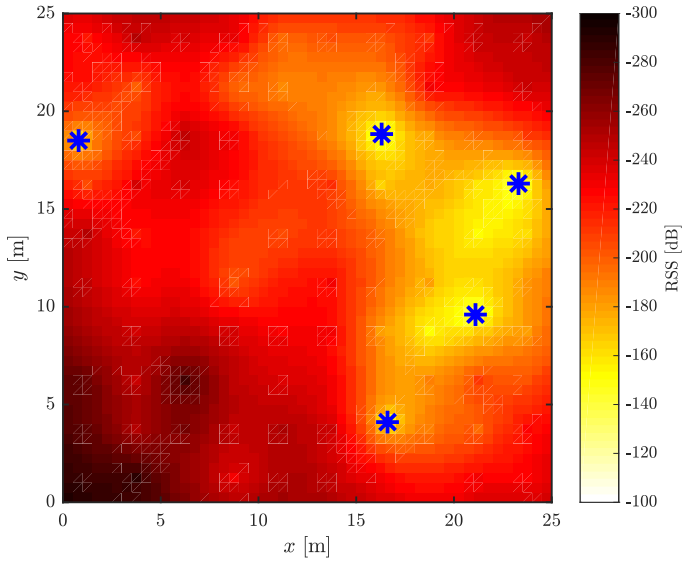

(b) 4% density.

Figure 3.7: Universal Kriging recovered RSS map in simulation.

data points are short, and the correlation can be "ignored" if the data points are widely apart. As a result, only the data points within the decorrelation is selected to estimate the unknown RSS measurement. For the IDW and ordinary Kriging methods, the same decorrelation distance is adopted.

Figure 3.5, Figure 3.6 and Figure 3.7 illustrate the recovered RSS map using different interpolation methods.It is intuitive that the maps recovered from datasets of 25% density are more "smooth" than the maps recovered from 4% density. It, to a certain extent, implies the less information contained in datasets of lower density. Whilst, the IDW recovered maps is more "smooth" than the Kriged maps. This is due to the poorly weighting system and overly averaging of IDW without benefits from spatial correlations.

To study the qualities of the recovered database, the averaged root-mean-square error (RMSE) of an RSS estimate is calculated as follows:

$$\text{RMSE} = \sqrt{\frac{1}{K}\sum_{i=1}^{K}(\mathbf{z}_i - \bar{\mathbf{z}}_i)^{\mathsf{T}} \cdot (\mathbf{z}_i - \bar{\mathbf{z}}_i)} \tag{3.48}$$

where $\mathbf{z}_i$ is the RSS vector of i-th fingerprint from the original database, $\bar{\mathbf{z}}$ is the corresponding estimate from the recovered database, and K is the total number of

fingerprints.

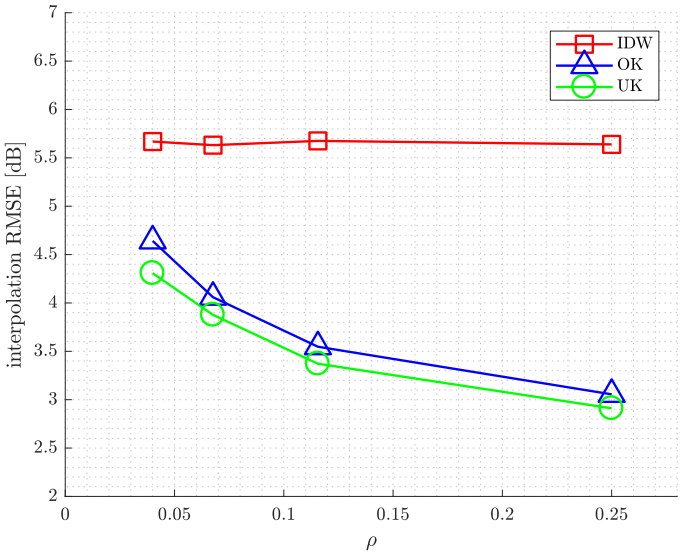

Figure 3.8: Interpolation RMSE.

Figure 3.8 shows the interpolation results analysis. The IDW method gives the worst interpolation results of which the interpolation RMSE stays around 5.7dB. However, it is due to the overlarge decorrelation distance adopted, all data points within the decorrelation distance are averaged to produce the estimate. This results in that the interpolation RMSE of IDW change merely with respect to the density.

As expected, the interpolation RMSE of ordinary Kriging and universal Kriging are better than the IDW method. Both RMSE profiles decrease with the increase in density. Consistently to the variogram modelling result, the universal Kriging gives better interpolation than the ordinary Kriging. However, the gap is small, which indicates that both Kriging methods are effective.

The final purpose is to perform fingerprinting localisation. Therefore, all the recovered databases are tested by a simple fingerprinting algorithm. Specifically, the fingerprint whose measurement vector has the smallest Euclidean distance to the target measurement vector is given as the target location estimate. Entries in the comparing data set are used as the target including a location and corresponding RSS measurements.

As shown in Figure 3.9, the IDW recovered databases provide the worst localisation performance. However, the RMSE profile decreases with the increases in

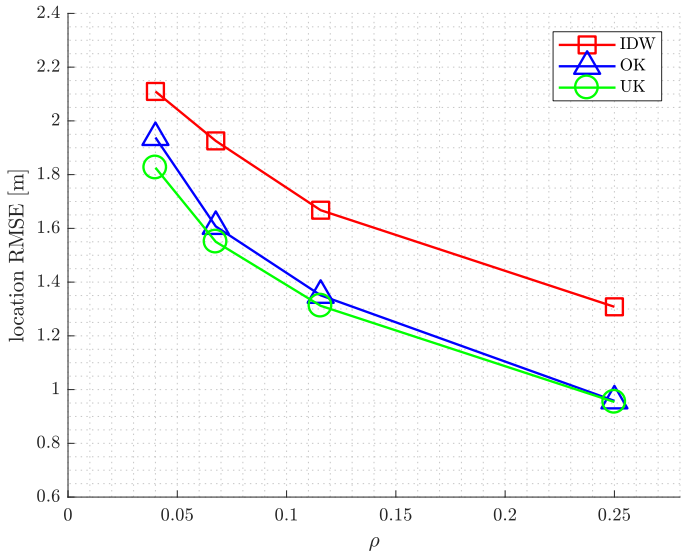

Figure 3.9: Localisation RMSE.

density, which is different from the interpolation result. It is because during the fingerprinting with IDW recovered databases, a target is usually estimated at the nearest "known" data point rather than a recovered location. Therefore, the denser the "known" data points are, the better accuracy the localisation would achieve.

Both RMSE profiles of ordinary Kriging and universal Kriging recovered database decrease with the increase of data points density. Consistently Figure 3.8, the ordinary Kriging recovered databases give better localisation performance than IDW, while the universal Kriging method provides the best. The gap between the ordinary Kriging and universal Kriging profiles decrease and almost coincide when the density reaches 25%. It implies that both ordinary Kriging and universal Kriging recovered databases have equivalent quality for localisation when the interpolation error is lower than a certain level.

3.3.2 Real Data Experiment

The real-data collection is conducted in the room D10 of Amy Johnson building, University of Sheffield. The RSS measurement of a Cisco wireless access point is collected using an Android mobile device held by a human. As shown in Figure 3.10, the room is divided into 1 meter grids. At each grid centre, about 100 RSS readings are collected in 1 minute, and then the averaged reading are used as grid measure-

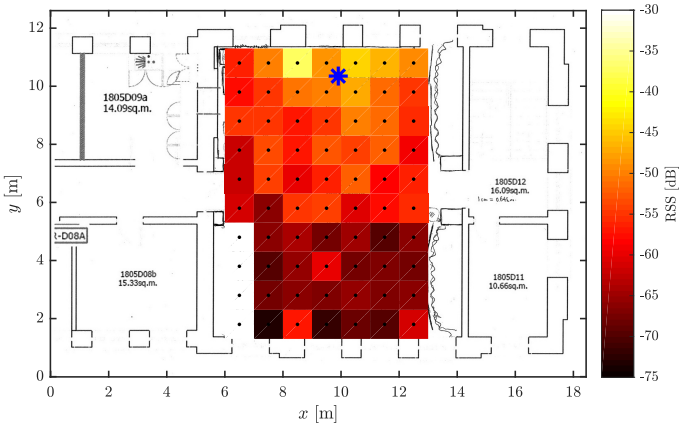

Figure 3.10: Original RSS map.

ments. The blue asterisk denotes the location of access points.

As shown in Figure 3.10, if the RSS is considered as model (3.41), the shadowing noise is significant and changes rapidly in spatial. Taking the example of two grids in the left bottom, the RSS difference is about 27dB for the interval of 1 meter.

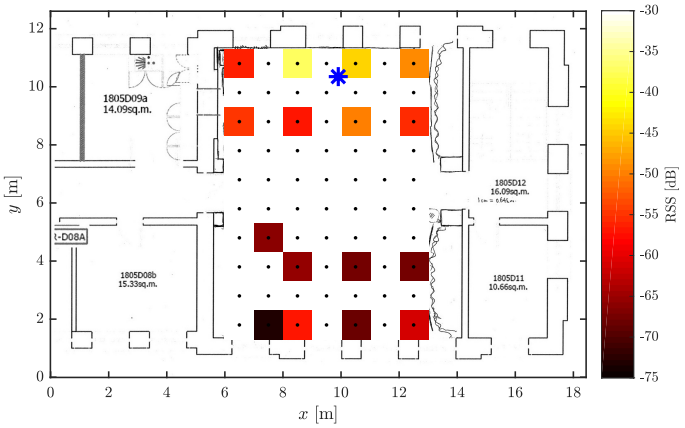

(a) 20 fingerprints, 28.5% density.

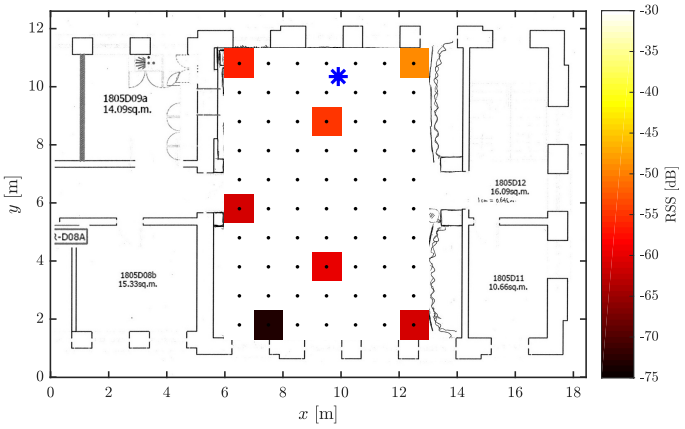

(b) 7 fingerprints, 10% density.

Figure 3.11: Fingerprint maps of reference sets for real data experiments.

The severe changes result from the human body absorption and device orientation, which might lead to difficulties in modelling shadowing spatial correlation.

The Figure 3.11 demonstrate the map of remained RSS fingerprints after sampling. The remained data points were manually picked but approximate uniformly sampling. Following the same manner, the remained fingerprints are used to estimate the removed/unmeasured RSS through the IDW, ordinary Kriging and universal Kriging methods. Because the room is of small size compared with the decorrelation distance in simulation and the remained fingerprints could be too sparse for interpolation, the whole room is regarded as neighbour area for each unknown data

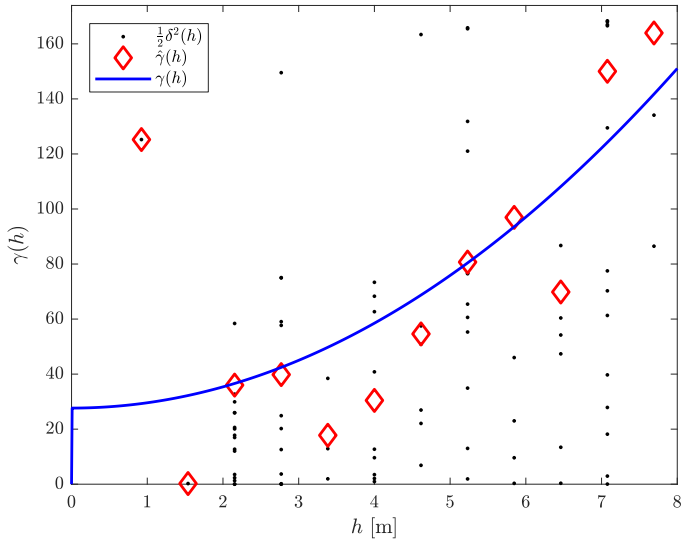

(a) 28.5% density.

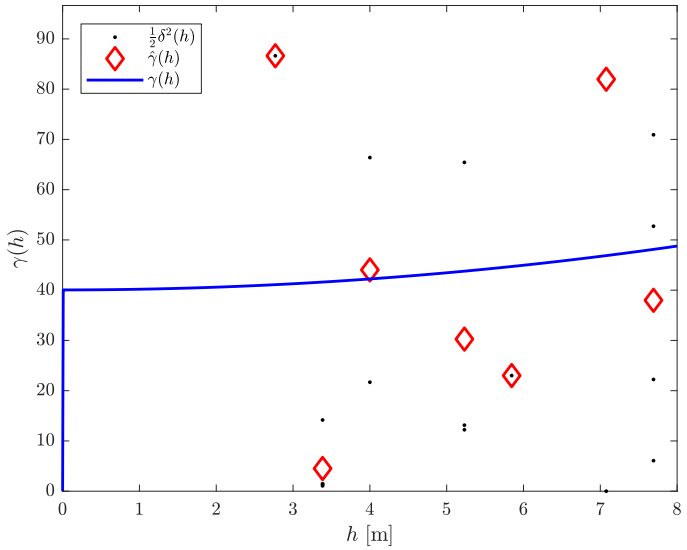

(b) 10% density.

Figure 3.12: Ordinary Kriging variogram modelling for real data experiment.

points, and all RSS in the remained data set will be utilised for interpolation.

The variogram modelling for ordinary Kriging method is shown in the Figure 3.12. As illustrated, the black dots which represent the half square of the RSS difference are much fewer than simulation and less concentrated around the red diamonds that represent the mean value. Furthermore, the variogram fitting quality is obviously lower, especially for lower density. This could be the consequence of significant and rapidly varying shadowing noises.

The effects of significant shadowing noises can be seen more clearly from Figure 3.13. As shown, the empirical variogram value for residuals after removing the

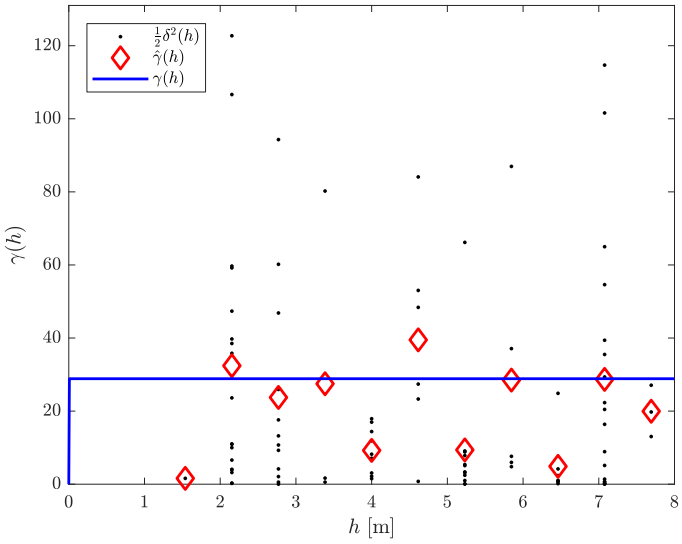

(a) 28.5% density.

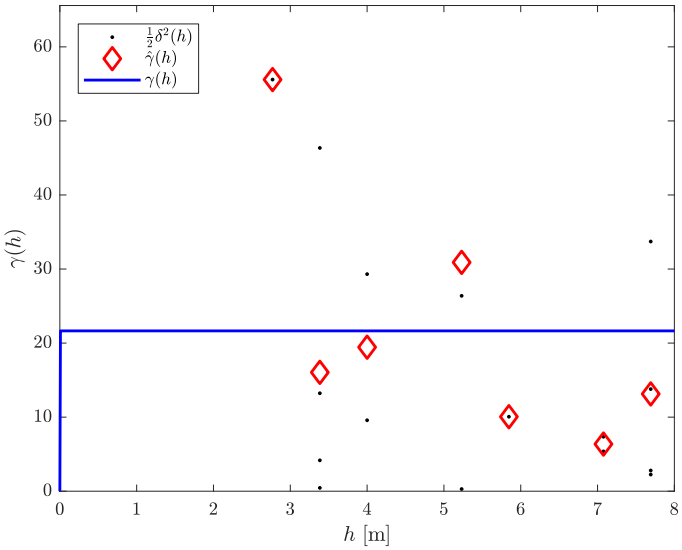

(b) 10% density.

Figure 3.13: Residual variogram modelling for real data experiment.

trend components are randomly scattered, and the fitted variogram model is almost flat. This implies that the residuals merely have a spatial correlation.

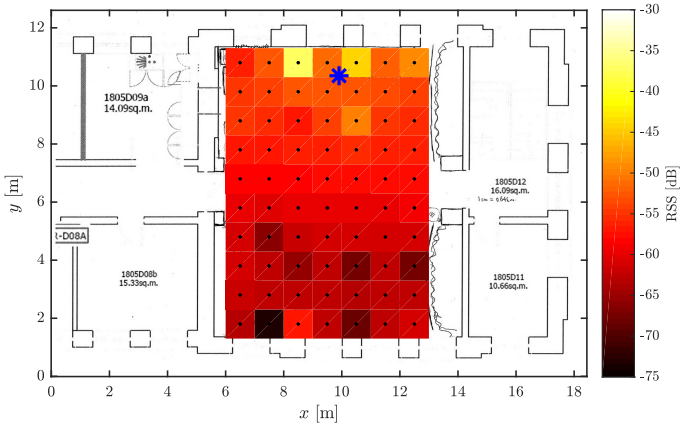

(a) 28.5% density.

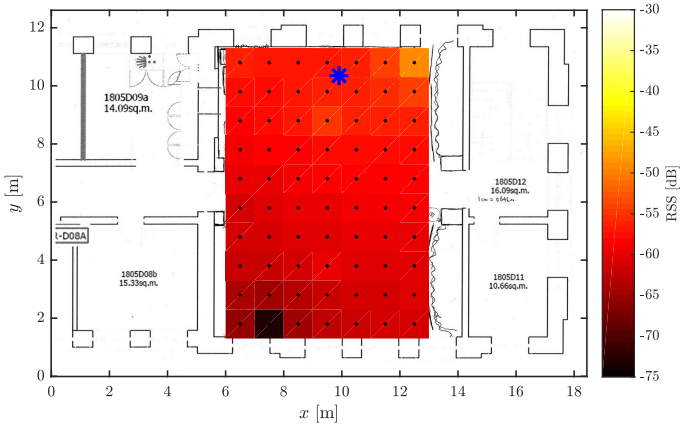

(b) 10% density.

Figure 3.14: IDW recovered fingerprint map for real data experiment.

Figure 3.14, Figure 3.15 and Figure 3.16 show the maps recovered by different methods.

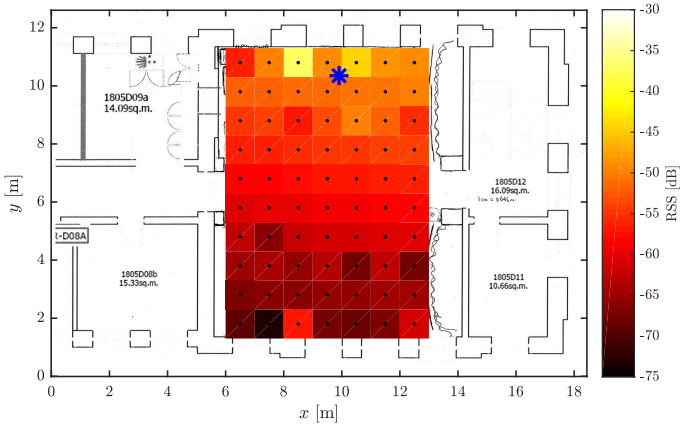

(a) 28.5% density.

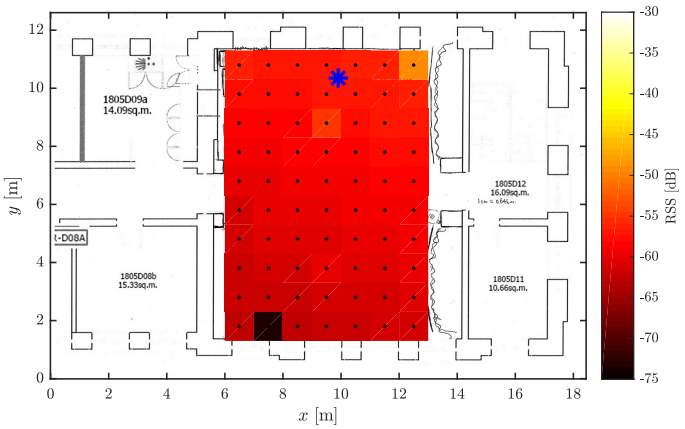

(b) 10% density.

Figure 3.15: Ordinary Kriging recovered fingerprint map for real data experiment.

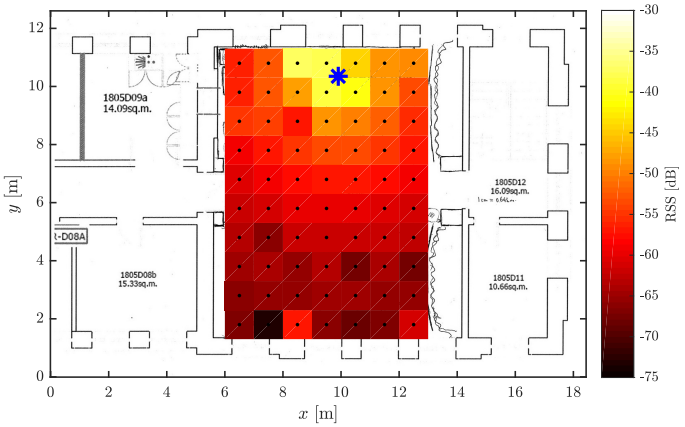

(a) UK recovered map. 28.5% density.

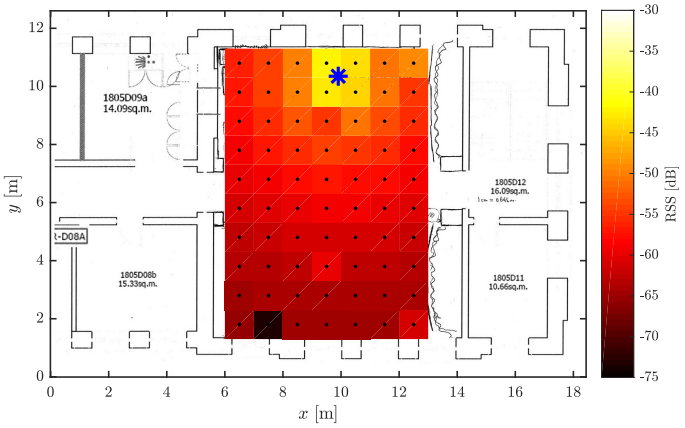

(b) UK recovered map. 10% density.

Figure 3.16: Universal Kriging recovered fingerprint map for real data experiment.

Figure 3.17 depicts the interpolation RMSE profiles calculated in the same manner as simulation. As shown, the capabilities of different methods are demonstrated to a certain extent. More precisely, the IDW method produces the worst interpolation quality in general, but the corresponding RMSE profile decreases as the increase

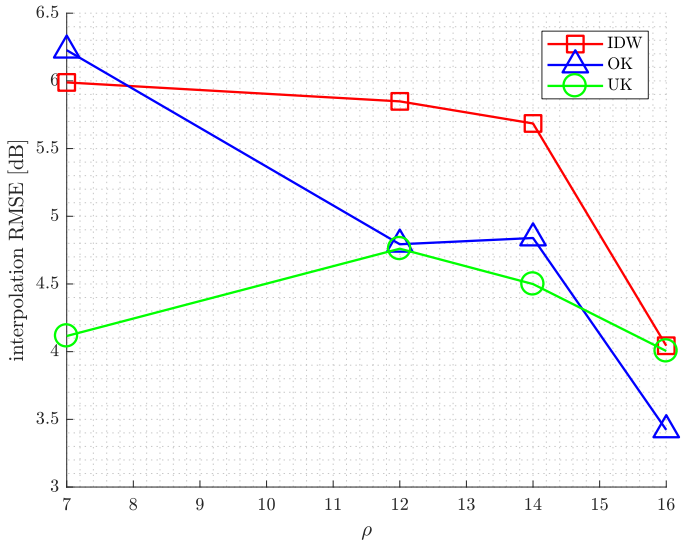

Figure 3.17: Interpolation RMSE for real data experiment.

of data points density. The UK method has the best interpolation quality overall, but the RMSE profile fluctuates with the increase of density rather than generally decreases. The ordinary Kriging method offers the intermediate interpolation quality overall but has the worst RMSE at 10% density and the best RMSE at 28.5% density.

This interpolation result is not as clear and convincing as simulation. It is most likely affected by the significant and rapidly varying shadowing noises. First, take the example of Figure 3.13, the residual variograms are almost flat and obviously could not characterise spatial correlation. Therefore, the Kriging interpolation computation is completely dominated by the trend components, as shown in Figure 3.16a and Figure 3.16b. Second, due to the rapidly varying noises, picking of reference data points are important as well. Figure 3.15b is a typical example. where without a good reference adjacent to the access point, the RSS fingerprint estimates surrounding the access points have significant errors.

3.4 Summary

In this chapter, the Geostatistics tools, Kriging interpolation method, are adopted to estimated RSS fingerprints at unmeasured locations from reference data set. Both

ordinary Kriging and universal Kriging methods are first introduced and then validated through simulation and real data experiments. The results show that compared with a standard interpolation method, inverse distance weighted method, the ordinary Kriging and universal Kriging can provide better interpolation qualities from reference data points of different densities. The ordinary Kriging and universal Kriging interpolated fingerprint databases can also offer better location accuracy with a standard fingerprinting localisation method.

Chapter 4

A Bayesian Framework of Indoor Multi-target Localisation considering Shadowing Correlation

A considerable amount of research has been done to improve the performance of received signal strength (RSS) based localisation, e.g. with variational methods [60]. Joint estimation of the path loss exponent (PLE) and the location is discussed in [61]–[63], the cooperative RSS localization is studied in [64], [65], and the Gaussian process type of methods for the PLE estimation, related parameters and state estimation is proposed in [66]. Recently Gaussian process methods for localisation are also presented in [67], [68].

Most of these studies assume that individual links between targets and beacon base stations are independent. This is an oversimplification since closely located targets and base stations in a network introduce a correlated shadowing effect in RSS measurements. It is shown in [69] that if these correlations are taken into account, it could enhance the localisation performance. This proposition was done by deriving the Cramér-Rao bound for shadowing correlation between nodes.

In practice, the shadowing correlation can be estimated by calculating the sample covariance of RSS measurements, which requires a large amount of data. If the num-

ber of measurements is equal to or smaller than the variable dimension, covariance estimation will be ill-posed and contain a noticeable error, making it non-invertible. However, in a network consisting of multiple targets and base stations, the variable dimension can be large while the measurements are insufficient. Therefore, conventional localisation algorithms cannot readily benefit from the shadowing information.

In [70], an efficient multi-target localisation approaches for scenarios with a limited number of measurements is presented. Specifically, the shrinking techniques is applied to produce a full-ranked shadowing covariance matrix from insufficient RSS measurements a generalised least squares (GLS) based localisation approach is enhanced by employing shrinkage techniques in the estimation of the measurement covariance. It is shown via simulation that covariance estimation using shrinkage techniques has a smaller error compared to computing the sample covariance matrix when the number of measurements is limited. Consequently, localisation performance is improved.

In this chapter, a Bayesian framework of multi-target localisation is proposed. First, taking advantages of inverse Wishart (IW) conjugate prior, a new closed-form posterior of multi-target location is presented, in which the shadowing correlation is exploit given limited number of measurements. Second, an Markov Chain Monte Carlo (MCMC) sampling method, namely the Metropolis-within-Gibbs sampling method, is used to get samples from the posterior. The final estimate of target locations is computed as the mean. Third, an maximum a posterior (MAP) / maximum likelihood (ML) method is developed as an alternative to obtaining the target location estimates from the posterior. The proposed approaches are evaluated via simulation.

The chapter is organised as follows: Section I formulates the multi-target localisation problem and introduces the variable notations for conciseness. A closed-form posterior of target locations is developed in Section III. Section IV first describes the MCMC based location estimation, and the corresponding simulation results are

presented and analysed after. Section V first explained the adopted MAP/ML approach and then studied the simulation results. The final section summaries the chapter.

4.1 Problem Formulation

Based on the RSS measurement model (2.2), the problem will be introduced here in the context of multi-target localisation.

There are m targets, and the location of i-th target is denoted by $\mathbf{s}_i = [x_{s,i}, y_{s,i}]^\mathsf{T}$. There are n base stations, and the location of j-th base station is denoted by $\mathbf{P}_{0,j} = [x_{b,j}, y_{b,j}]^\mathsf{T}$. The distance between the i-th target and j-th base station is given by $d_{i,j} = \sqrt{(x_{s,i} - x_{b,j})^2 + (y_{s,i} - y_{b,j})^2}$.

The signal strength for the j-th base station received by the i-th target, is denoted by $z_{i,j}$ and modelled in dB as

$$z_{i,j} = f_{i,j} + \varepsilon_{i,j}, \tag{4.1}$$

where $\varepsilon_{i,j}$ represents the shadowing attenuation and is Gaussian distributed with zero mean and variance σ_ε^2, and $f_{i,j}$ is given by

$$f_{i,j} = P_{0,j} - l_0 - 10\alpha \log_{10} d_{i,j}, \tag{4.2}$$

in which $P_{0,j}$ is the transmitting power of j-th base station, l_0 is the reference path loss measured at 1 meter away from the base station, and α is the path loss exponent.

For the i-th target, the collected RSS measurement vector is denoted by $\mathbf{z}_i = [z_{i,1}, ...z_{i,n}]^\mathsf{T}$. For multiple targets, $\mathbf{s}_1 \dots \mathbf{s}_m$, the composed RSS vector is given by $\mathbf{z} = [\mathbf{z}_1^\mathsf{T}, , ..., \mathbf{z}_m^\mathsf{T}]^\mathsf{T}$. According to (2.2), $\mathbf{z}$ is Gaussian distributed

$$\mathbf{z} \sim \mathcal{N}(\mathbf{f}, \mathbf{\Sigma}_\varepsilon) \tag{4.3}$$

where the composed vector $\mathbf{f}$ is given by

$$\mathbf{f} = [\mathbf{f}_1^\mathsf{T}, ..., \mathbf{f}_m^\mathsf{T}]^\mathsf{T}, \tag{4.4a}$$

$$\text{where} \quad \mathbf{f}_i = [f_{i,1}, ..., f_{i,n}]^\mathsf{T}, \tag{4.4b}$$

and $\mathbf{\Sigma}_\varepsilon$ is the shadowing covariance matrix that has following form:

$$\mathbf{\Sigma}_\varepsilon = \sigma_\varepsilon^2 \times \begin{bmatrix} \rho(\mathbf{z}_1, \mathbf{z}_1) & \rho(\mathbf{z}_1, \mathbf{z}_2) & \cdots & \rho(\mathbf{z}_1, \mathbf{z}_m) \\ \rho(\mathbf{z}_2, \mathbf{z}_1) & \rho(\mathbf{z}_2, \mathbf{z}_2) & \cdots & \rho(\mathbf{z}_2, \mathbf{z}_m) \\ \vdots & \vdots & \ddots & \vdots \\ \rho(\mathbf{z}_m, \mathbf{z}_1) & \rho(\mathbf{z}_m, \mathbf{z}_2) & \cdots & \rho(\mathbf{z}_m, \mathbf{z}_m) \end{bmatrix} \tag{4.5}$$

in which the matrix blocks are further given by

$$\rho(\mathbf{z}_i, \mathbf{z}_i) = \begin{bmatrix} \rho(z_{i,1}, z_{i,1}) & \cdots & \rho(z_{i,1}, z_{i,n}) \\ \vdots & \ddots & \vdots \\ \rho(z_{i,n}, z_{i,1}) & \cdots & \rho(z_{i,n}, z_{i,n}) \end{bmatrix} \tag{4.6a}$$

$$\rho(\mathbf{z}_i, \mathbf{z}_k) = \begin{bmatrix} \rho(z_{i,1}, z_{k,1}) & \cdots & \rho(z_{i,1}, z_{k,n}) \\ \vdots & \ddots & \vdots \\ \rho(z_{i,n}, z_{k,1}) & \cdots & \rho(z_{i,n}, z_{k,n}) \end{bmatrix} \tag{4.6b}$$

4.2 Bayesian Inference on Multi-target Locations

Typically, given RSS measurements, the posterior of multiple target locations can be computed as

$$p(\mathbf{s}_1 \dots \mathbf{s}_m \mid \mathbf{z}) \propto p(\mathbf{z} \mid \mathbf{s}_1 \dots \mathbf{s}_m) \cdot p(\mathbf{s}_1 \dots \mathbf{s}_m), \tag{4.7}$$

where $p(\mathbf{z} \mid \mathbf{s}_1 \dots \mathbf{s}_m)$ is the likelihood, $p(\mathbf{s}_1 \dots \mathbf{s}_m)$ represents the prior knowledge of target location.

Taking the shadowing correlation into consideration, the above equation can be

rewritten as

$$p(\mathbf{s}_1 \dots \mathbf{s}_m, \mathbf{\Sigma}_\varepsilon \mid \mathbf{z}) \propto p(\mathbf{z} \mid \mathbf{s}_1 \dots \mathbf{s}_m, \mathbf{\Sigma}_\varepsilon) \cdot p(\mathbf{s}_1 \dots \mathbf{s}_m, \mathbf{\Sigma}_\varepsilon). \tag{4.8}$$

The individual posterior of target locations can be further given through marginalising the shadowing covariance $\mathbf{\Sigma}_\varepsilon$, that is

$$p(\mathbf{s}_1 \dots \mathbf{s}_m \mid \mathbf{z}) = \int p(\mathbf{s}_1 \dots \mathbf{s}_m, \mathbf{\Sigma}_\varepsilon \mid \mathbf{z}) \, d\mathbf{\Sigma}_\varepsilon \tag{4.9a}$$

$$\propto \int p(\mathbf{z} \mid \mathbf{s}_1 \dots \mathbf{s}_m, \mathbf{\Sigma}_\varepsilon) \cdot p(\mathbf{s}_1 \dots \mathbf{s}_m, \mathbf{\Sigma}) \, d\mathbf{\Sigma}. \tag{4.9b}$$

The key point now here is to compute the integral in (4.9).

In practice, since the shadowing attenuation changes very slowly and is hard to characterise from a limited number of RSS measurements, it is typical to adopt a certain assumption of shadowing correlation/covariance, such as identity matrix or diagonal matrix. However, is there a way to exploit the limited information of the shadowing correlation contained in the target RSS measurements? In this work, the conjugate prior is utilised to achieve that.

If the posterior distribution belongs to the same family as the prior, then the prior and posterior are called conjugate distribution [71], [72]. Conjugate prior has the advantage that can lead to elegant solutions to challenging practical problems. Recently conjugate prior has been used for tracking extended objects (objects that are not considered as points but instead are considered with their size or volume) [73], [74]. The type of conjugate distribution used here is the inverse Wishart distribution.

4.2.1 Wishart distribution and Inverse Wishart Distribution

The Wishart distribution can be seen as a multivariable extension of χ^2 distribution [75]. Let $\mathbf{x}_1, ..., \mathbf{x}_k$ be independent and identically distributed samples drawn from an mn-dimensional multivariate Gaussian distribution $\mathcal{N}(\mathbf{f}, \mathbf{\Sigma})$. The sum-of-square

matrix $\mathbf{\Psi}$ has an mn-dimensional *Wishart* distribution, which is denoted by

$$\mathbf{\Psi} \sim \mathcal{W}_{mn}(\mathbf{\Sigma}, k), \quad \text{where } \mathbf{\Psi} = \sum_{i=1}^{v} (\mathbf{x}_i - \mathbf{f})(\mathbf{x}_i - \mathbf{f})^{\mathsf{T}}. \tag{4.10}$$

For cases where $k \geq mn$, the probability of $\mathbf{\Psi}$ is given by

$$p(\mathbf{\Psi}) = \frac{1}{2^{\frac{kmn}{2}} |\mathbf{\Sigma}|^{\frac{k}{2}} \mathbf{\Gamma}_{mn}(\frac{k}{2})} \cdot |\mathbf{\Psi}|^{\frac{k-mn-1}{2}} \exp\Big[-\frac{1}{2} \mathrm{tr}(\mathbf{\Psi}\mathbf{\Sigma}^{-1}) \Big]. \tag{4.11}$$

Under the same conditions, the inverse of sum-of-square matrix follows an IW distribution, that is

$$\mathbf{\Psi}^{-1} \sim \mathcal{W}_{mn}^{-1}(\mathbf{\Sigma}^{-1}, v), \quad \text{where } \mathbf{\Psi} = \sum_{i=1}^{v} (\mathbf{x}_i - \mathbf{f})(\mathbf{x}_i - \mathbf{f})^{\mathsf{T}}, \tag{4.12}$$

where v is the degree of freedom.

From an intuitive point of view, generating samples from an IW distribution can be interpreted as taking the inverse of covariance matrix as parameter and generating random inverse of sum-of-square matrices. However, since the scale is the same, it is helpful to look in an alternative way in practice, where the IW distribution takes the sum-of-square matrix as parameter and generates random covariance matrices [75], that is

$$\mathbf{\Sigma} \sim \mathcal{W}_{mn}^{-1}(\mathbf{\Psi}, v), \tag{4.13}$$

where the sum-of-square matrix $\mathbf{\Psi}$ is commonly known as *scale matrix*. Thus, the probability distribution of $\mathbf{\Sigma}$ is given by

$$p(\mathbf{\Sigma}) = \frac{|\mathbf{\Psi}|^{\frac{v}{2}}}{2^{\frac{vmn}{2}} \Gamma_{mn}(\frac{v}{2})} \cdot |\mathbf{\Sigma}|^{-\frac{v+mn+1}{2}} \cdot \exp\Big[-\frac{1}{2} \mathrm{tr}(\mathbf{\Psi}\mathbf{\Sigma}^{-1}) \Big]. \tag{4.14}$$

For $v > mn + 1$, the expected value of $\mathbf{\Sigma}$ is given by [75]

$$\mathbb{E}[\mathbf{\Sigma}] = \frac{\mathbf{\Psi}}{v - P_{0,j} - 1}. \tag{4.15}$$

It is worth to explain again that the degree of freedom v in (4.13) have the same

physical meaning as k in (4.10), which represent the number of samples drawn from the multivariate Gaussian distribution and aggregated in the scale matrix $\mathbf{\Psi}$. To ensure that $\mathbf{\Psi}$ is invertible, both v and m can not be smaller than the dimension of sample u.

4.2.2 A Closed-form Posterior of Multi-target Location

In practice, the IW distribution is applied as the conjugate prior of a multivariate normal distribution. On the one hand, an advantage of involving conjugate prior in Bayesian inference is to acquire elegant solutions [73]. On the other hand, since the shadowing changes very slowly and is hard to characterise from a limited number of RSS measurement, it is acceptable to adopt extra assumption about shadowing covariance. Therefore, this chapter proposes the IW distribution as the prior of shadowing covariances which further would lead to a new closed-form posterior of multi-target location.

Given the shadowing prior (4.14). the posterior in (4.9) is now written as

$$p(\mathbf{s}_1 \dots \mathbf{s}_m \mid \mathbf{z}) \propto p(\mathbf{s}_1 \dots \mathbf{s}_m) \cdot \int p(\mathbf{z} \mid \mathbf{s}_1 \dots \mathbf{s}_m, \mathbf{\Sigma}_\varepsilon) \cdot p(\mathbf{\Sigma}_\varepsilon)\, d\mathbf{\Sigma}_\varepsilon. \tag{4.16}$$

Compare the above equation with (4.7), the likelihood term has been substituted with an marginalised probability, that is

$$p(\mathbf{z} \mid \mathbf{s}_1 \dots \mathbf{s}_m) = \int p(\mathbf{z} \mid \mathbf{s}_1 \dots \mathbf{s}_m, \mathbf{\Sigma}_\varepsilon) \cdot p(\mathbf{\Sigma}_\varepsilon)\, d\mathbf{\Sigma}_\varepsilon, \tag{4.17}$$

where given the target locations and shadowing covariance, the probability of RSS measurement is given by

$$p(\mathbf{z} \mid \mathbf{s}_1 \dots \mathbf{s}_m, \mathbf{\Sigma}_\varepsilon) = \frac{1}{(2\pi)^{\frac{mn}{2}} |\mathbf{\Sigma}_\varepsilon|^{\frac{1}{2}}} \exp\left[-\frac{1}{2}(\mathbf{z}-\mathbf{f})^\top \mathbf{\Sigma}_\varepsilon^{-1}(\mathbf{z}-\mathbf{f}) \right], \tag{4.18}$$

where it is assumed that the necessary parameters (locations of base stations, transmitting powers, reference path loss and path loss exponents have been obtained

priorly through field investigation), so that the composed vector $\mathbf{f}$ can be computed based on (4.2) and (4.4).

The probability product $p(\mathbf{z} \mid \mathbf{s}_1 \dots \mathbf{s}_m, \boldsymbol{\Sigma}_\varepsilon) \cdot p(\boldsymbol{\Sigma}_\varepsilon)$ in (4.17) can be further derived as

$$
\begin{aligned}
& p(\mathbf{z} \mid \mathbf{s}_1 \dots \mathbf{s}_m, \boldsymbol{\Sigma}_\varepsilon) \cdot p(\boldsymbol{\Sigma}_\varepsilon) \\
=& \frac{1}{(2\pi)^{\frac{mn}{2}} |\boldsymbol{\Sigma}_\varepsilon|^{\frac{1}{2}}} \exp\Big[-\frac{1}{2}(\mathbf{z}-\mathbf{f})^{\mathsf{T}} \boldsymbol{\Sigma}_\varepsilon^{-1} (\mathbf{z}-\mathbf{f}) \Big] \\
& \qquad \cdot \frac{|\boldsymbol{\Psi}|^{\frac{v}{2}}}{2^{\frac{vmn}{2}} \Gamma_{mn}(\frac{v}{2})} \cdot |\boldsymbol{\Sigma}_\varepsilon|^{-\frac{v+mn+1}{2}} \cdot \exp\Big[-\frac{1}{2} \mathrm{tr}(\boldsymbol{\Psi} \boldsymbol{\Sigma}_\varepsilon^{-1}) \Big] \qquad (4.19a) \\
=& \frac{1}{(2\pi)^{\frac{mn}{2}}} \cdot \frac{|\boldsymbol{\Psi}|^{\frac{v}{2}}}{2^{\frac{vmn}{2}} \Gamma_{mn}(\frac{v}{2})} \cdot |\boldsymbol{\Sigma}_\varepsilon|^{-\frac{1}{2}} \cdot |\boldsymbol{\Sigma}_\varepsilon|^{-\frac{v+mn+1}{2}} \\
& \qquad \cdot \exp\Big[-\frac{1}{2}(\mathbf{z}-\mathbf{f})^{\mathsf{T}} \boldsymbol{\Sigma}_\varepsilon^{-1} (\mathbf{z}-\mathbf{f}) - \frac{1}{2} \mathrm{tr}(\boldsymbol{\Psi} \boldsymbol{\Sigma}_\varepsilon^{-1}) \Big] \qquad (4.19b) \\
=& \frac{1}{(2\pi)^{\frac{mmn}{2}}} \cdot \frac{|\boldsymbol{\Psi}|^{\frac{v}{2}}}{2^{\frac{vmn}{2}} \Gamma_{mn}(\frac{v}{2})} \cdot |\boldsymbol{\Sigma}_\varepsilon|^{-\frac{(v+1)+mn+1}{2}} \cdot \exp\Big[-\frac{1}{2} \mathrm{tr}(\boldsymbol{\Phi} \boldsymbol{\Sigma}_\varepsilon^{-1}) - \frac{1}{2} \mathrm{tr}(\boldsymbol{\Psi} \boldsymbol{\Sigma}_\varepsilon^{-1}) \Big] \qquad (4.19c) \\
=& \frac{1}{(2\pi)^{\frac{mn}{2}}} \cdot \frac{|\boldsymbol{\Psi}|^{\frac{v}{2}}}{2^{\frac{vmn}{2}} \Gamma_{mn}(\frac{v}{2})} \cdot \frac{2^{\frac{(v+1)mn}{2}} \Gamma_{mn}(\frac{v+1}{2})}{|\boldsymbol{\Phi}+\boldsymbol{\Psi}|^{\frac{v+1}{2}}} \\
& \qquad \cdot \frac{|\boldsymbol{\Phi}+\boldsymbol{\Psi}|^{\frac{v+1}{2}}}{2^{\frac{(v+1)mn}{2}} \Gamma_{mn}(\frac{v+1}{2})} \cdot |\boldsymbol{\Sigma}_\varepsilon|^{\frac{(v+1)+mn+1}{2}} \cdot \exp\Big[-\frac{1}{2} \mathrm{tr}\Big((\boldsymbol{\Phi}+\boldsymbol{\Psi}) \boldsymbol{\Sigma}_\varepsilon^{-1} \Big) \Big], \qquad (4.19d)
\end{aligned}
$$

where from (4.19b) to (4.19c), the first term in the exponent function is first replace by the trace of it, that is

$$
(\mathbf{z}-\mathbf{f})^{\mathsf{T}} \boldsymbol{\Sigma}_\varepsilon^{-1} (\mathbf{z}-\mathbf{f}) = \mathrm{tr}\big((\mathbf{z}-\mathbf{f})^{\mathsf{T}} \boldsymbol{\Sigma}_\varepsilon^{-1} (\mathbf{z}-\mathbf{f}) \big), \tag{4.20}
$$

and then since the trace function is invariant under cyclic permutation, the production order within the trace function has been rotated, that is

$$
\mathrm{tr}((\mathbf{z}-\mathbf{f})^{\mathsf{T}} \boldsymbol{\Sigma}_\varepsilon^{-1} (\mathbf{z}-\mathbf{f})) = \mathrm{tr}\big((\mathbf{z}-\mathbf{f})(\mathbf{z}-\mathbf{f})^{\mathsf{T}} \boldsymbol{\Sigma}_\varepsilon^{-1} \big) = \mathrm{tr}(\boldsymbol{\Phi} \boldsymbol{\Sigma}_\varepsilon^{-1}), \tag{4.21}
$$

and

$$\mathbf{\Phi} = (\mathbf{z} - \mathbf{f})(\mathbf{z} - \mathbf{f})^{\mathsf{T}}. \tag{4.22}$$

Substitute the probability product with (4.19d), the posterior can be further derived as

$$\begin{aligned} & p(\mathbf{z} \mid \mathbf{s}_1 \dots \mathbf{s}_m) \\ =& \frac{1}{(2\pi)^{\frac{mn}{2}}} \cdot \frac{|\mathbf{\Psi}|^{\frac{v}{2}}}{2^{\frac{vmn}{2}} \Gamma_{mn}(\frac{v}{2})} \cdot \frac{2^{\frac{(v+1)mn}{2}} \Gamma_{mn}(\frac{v+1}{2})}{|\mathbf{\Phi} + \mathbf{\Psi}|^{\frac{v+1}{2}}} \\ & \cdot \int \frac{|\mathbf{\Phi} + \mathbf{\Psi}|^{\frac{v+1}{2}}}{2^{\frac{(v+1)mn}{2}} \Gamma_{mn}(\frac{v+1}{2})} \cdot |\mathbf{\Sigma}_\varepsilon|^{\frac{(v+1)+mn+1}{2}} \cdot \exp\left[-\frac{1}{2} \mathrm{tr}\Big((\mathbf{\Phi} + \mathbf{\Psi}) \mathbf{\Sigma}_\varepsilon^{-1} \Big) \right] d\mathbf{\Sigma}_\varepsilon \end{aligned} \tag{4.23a}$$

$$= \frac{1}{(2\pi)^{\frac{mn}{2}}} \cdot \frac{|\mathbf{\Psi}|^{\frac{v}{2}}}{2^{\frac{vmn}{2}} \Gamma_{mn}(\frac{v}{2})} \cdot \frac{2^{\frac{(v+1)mn}{2}} \Gamma_{mn}(\frac{v+1}{2})}{|\mathbf{\Phi} + \mathbf{\Psi}|^{\frac{v+1}{2}}}. \tag{4.23b}$$

where the expression in the integral in (4.23a) is a new IW distribution with parameter $\mathbf{\Psi}' = \mathbf{\Phi} + \mathbf{\Psi}$ and degree of freedom $v' = v + 1$, therefore the integral is equal to 1 and dismisses in (4.23b).

So far, an analytic expression of likelihood $p(\mathbf{z} \mid \mathbf{s}_1 \dots \mathbf{s}_m)$, which utilises the IW conjugate prior to enclose the shadowing correlation information included in the RSS measurements, have been derived.

It is assumed that the location of base stations and other parameters in (**??**) are known. Once given the prior of target location, $\mathbf{\Phi}$ can be calculated from (4.22), and later the posterior distribution can be calculated from (4.23). The next stage is to design the approach to make inference about target location from the posterior.

In this work, an MCMC method, precisely the Metropolis-within-Gibbs sampling method, is first applied to obtained samples of target locations from the posterior. The final estimate of target location is calculated based on the samples. This MCMC based localisation method have been tested in simulations against different parameter configurations.

Secondly, the MAP/ML estimate is studied as an alternative. To evaluate the

MAP estimate approach, simulation results is investigated and analysed.

4.3 MCMC based Location Estimation

An intuitive way to estimate the target location is first to draw enough samples from the posterior and then make inferences based on the samples. In this work, the posterior is multivariable and too complex to directly obtain samples from. Thus, the MCMC method is applied.

Under certain conditions, the probability distribution of states of a Markov chain will gradually converge to a steady distribution, which is called stationary (or steady state) distribution. Therefore, a Markov chain can be designed technically to have the target distribution as its stationary distribution. The states that have been visited after the convergence can be seen as samples drawn from the target distribution.

4.3.1 MCMC Sampler

4.3.1.1 Metropolis-Hastings Sampling

The Metropolis-Hastings sampling method is the most commonly used MCMC method. The target distribution is denoted by $p(\mathbf{s})$. Started from a random/selected initial state $\mathbf{s}^{(0)} = [\mathbf{s}_1^{(0)} \dots \mathbf{s}_m^{(0)}]$, a new point will be generated from the previous state following a proposed distribution, that is

$$\mathbf{s}^* \sim q(\mathbf{s}^* \mid \mathbf{s}^{(t-1)}). \tag{4.24}$$

Then, it is due to an *acceptance ratio* α whether the point is accepted as the new state. The acceptance ratio is calculated as

$$\alpha = \min\left(\frac{p(\mathbf{s}^*) \cdot q(\mathbf{s}^{(t-1)} \mid \mathbf{s}^*)}{p(\mathbf{s}^{(t-1)}) \cdot q(\mathbf{s}_i^* \mid \mathbf{s}^{(t-1)})}, 1\right). \tag{4.25}$$

If the new point is rejected, the previous state will be duplicate as the new one. In this manner, a series of states are generated and the probability distribution

of state will converge to the target distribution $p(\mathbf{s})$. The convergence process is called *burn-in* period. The pseudo-code for Metropolis-Hastings method is given in Algorithm 1.

Algorithm 1 Metropolis-Hastings Sampler

Initialise $\mathbf{s}_1^{(0)} \dots \mathbf{s}_m^{(0)}$.
for $t = 1, 2, \dots,$ **do**
- draw $\mathbf{s}^* \sim q(\mathbf{s}_i^* \mid \mathbf{s}^{(t-1)})$,
- compute the acceptance ratio α from (4.25),
- uniformly generate a random number between 0 and 1, $u \sim U[0, 1]$,
  if $u < \alpha$, accept $\mathbf{s}^*$ as the new state,
  otherwise, remain $\mathbf{s}^{(t-1)}$ as the new state,

end for.

There is a vital disadvantage of Metropolis-Hastings method: the acceptance ratio α can be extremely small especially for high-dimensional problems, which leads to unacceptably long burn-in period.

4.3.1.2 Gibbs Sampler

For high-dimensional sampling, the Gibbs sampler is more efficient compared with the Metropolis-Hastings algorithm [76]. Given the target distribution $p(\mathbf{s})$, assume the full conditional distribution for $\mathbf{s}_i$ is available, which is

$$p(\mathbf{s}_i \mid \mathbf{s}_{(-i)}, \mathbf{z}), \tag{4.26}$$

where $\mathbf{s}_{(-i)}$ includes all targets except for $\mathbf{s}_i$. The full conditional distribution (4.26) can be obtained by marginalising out the other targets, which is

$$p(\mathbf{s}_i \mid \mathbf{s}_{(-i)}, \mathbf{z}) = \int \cdots \int p(\mathbf{s}_1 \dots \mathbf{s}_m \mid \mathbf{z})\, d\mathbf{s}_1 \dots d\mathbf{s}_{i-1} d\mathbf{s}_{i+1} \dots d\mathbf{s}_m. \tag{4.27}$$

From a initial state $\mathbf{s}^{(0)}$, the Gibbs sampler draws each component of the new state according (4.26) in a rotation manner. After getting all components, the new state is immediately accepted. The pseudo-code for Gibbs sampler is given in Algorithm 2.

Algorithm 2 Gibbs sampler

Initialise $\mathbf{s}_1^{(0)} \dots \mathbf{s}_m^{(0)}$.
for $t = 1, 2, \dots,$ **do**
- draw $\mathbf{s}_1^{(t)} \sim p(\mathbf{s}_1^{(t-1)} \mid \mathbf{s}_{(-1)}^{(t-1)}, \mathbf{z})$,
- draw $\mathbf{s}_2^{(t)} \sim p(\mathbf{s}_2^{(t-1)} \mid \mathbf{s}_{(-2)}^{(t-1)}, \mathbf{z})$,
- $\vdots$
- draw $\mathbf{s}_m^{(t)} \sim p(\mathbf{s}_m^{(t-1)} \mid \mathbf{s}_{(-m)}^{(t-1)}, \mathbf{z})$,

end for.

However, in practice, the full conditional probability (4.26) is usually not available and is hard to derive from the target distribution $p(\mathbf{s})$. Thus, an alternative solution which combined the Metropolis-Hastings method and Gibbs sampler are developed.

4.3.2 Metropolis-within-Gibbs Sampler

When performing the Gibbs sampling, in cases where the full conditional distribution (4.26) is unavailable, it is replaced by a Metropolis step. This approach is known as *Metropolis-within-Gibbs* sampler [77].

More precisely, when generating a new point $\mathbf{s}^*$, the i-th component $\mathbf{s}_i^*$ is drawn from a proposed distribution $q(\mathbf{s}_i^* \mid \mathbf{s}_i^{(t-1)})$,

$$\mathbf{s}_i^* \sim q(\mathbf{s}_i^* \mid \mathbf{s}_i^{(t-1)}). \tag{4.28}$$

In this work, the proposed distribution is Gaussian, given by

$$\mathbf{s}_i^* \sim \mathcal{N}(\mathbf{s}_i^{(t-1)}, w^2 \mathrm{I}_{2\times 2}). \tag{4.29}$$

This is also known as *random-walk* mechanism, where the centre of proposed distribution is the corresponding element of previous state, and w is known as the step size of random walk which controls the distance "travelled" by the new point.

Afterwards, the point is accepted based on the *acceptance ratio*, which is

$$\alpha = \min\left(\frac{p(\mathbf{s}_i^*, \mathbf{s}_{(-i)}^{(t-1)} \mid \mathbf{z}) \times q(\mathbf{s}_i^{(t-1)} \mid \mathbf{s}_i^*)}{p(\mathbf{s}_i^{(t-1)}, \mathbf{s}_{(-i)}^{(t-1)} \mid \mathbf{z}) \times q(\mathbf{s}_i^* \mid \mathbf{s}_i^{(t-1)})}, 1\right) \tag{4.30}$$

The pseudo-code for Metropolis-within-Gibbs sampler is given in Algorithm 3.

Algorithm 3 Metropolis-within-Gibbs sampler

Initialise $\mathbf{s}_1^{(0)} \ldots \mathbf{s}_m^{(0)}$.
for $t = 1, 2 \ldots$ **do**
  for $i = 1 \ldots m$, **do**
    - draw $\mathbf{s}_i^{(t)} \sim q(\mathbf{s}_i^* \mid \mathbf{s}_i^{(t-1)})$,
    - compute acceptance ration α from (4.30),
    - uniformly generate a random number between 0 and 1, $u \sim U[0, 1]$,
      if $u < \alpha$, accept $\mathbf{s}_i^*$ as the new state,
      otherwise, remain $\mathbf{s}_i^{(t-1)}$ as the new state,
  end for
end for.

In this work, the target location posterior developed in (4.23) is apparently multi-dimensional and is difficult to derive the marginal probability of a single target. Thus, in this work, the Metropolis-within-Gibbs sampler is more practical than the other two MCMC methods.

4.3.3 Target Location Estimation

By applying the Metropolis-within-Gibbs method, a sequence of samples following the posterior of target location can be obtained after the burn-in period t_b. The estimate of multiple target locations is computed as the mean of the samples, that is

$$\hat{\mathbf{s}} = \frac{1}{t - t_b} \sum_{i=t_b}^{t} \mathbf{s}^{(i)}, \tag{4.31}$$

where t is the total number of MCMC samples. The estimate covariance can be calculated as *sample covariance* as

$$\mathbf{\Sigma} = \frac{1}{t - t_b - 1} \sum_{i=t_b}^{t} (\mathbf{s}^{(i)} - \hat{\mathbf{s}})^{\mathsf{T}} (\mathbf{s}^{(i)} - \hat{\mathbf{s}}), \tag{4.32}$$

where the diagonal of $\mathbf{\Sigma}$ consists of estimate variances of individual target locations.

4.3.4 Simulation and Results Analysis

The proposed closed-form posterior of multi-target location and MCMC based localisation approach have been tested in two simulation scenarios. As shown in Figure 4.1, there are 3 base stations and 2 targets, which meets the minimum requirement for multi-targets localisation. The RSS measurements is generated using the model (4.1), (4.2) and the shadowing correlation simulated adopting the Gudmundson's model (2.7). The model parameters adopt typical value [78] and are listed in Table 4.1. The target location posterior is computed by the proposed method given in (4.16) and (4.23). The prior of target location adopts the uniform distribution as for general scenarios where it is uninformed.

Table 4.1: Table of propagation model parameters

Parameter Name	Notation	Value
transmitting power	$P_{0,j}$	10
referencing path loss	l_0	0
path loss exponent	α	5
decorrelation distance [m]	d_c	3

Figure 4.1 depicts MCMC samples generated under difference conditions. Each sample colour stands a target. The initial point is set at the middle point between the two targets. For each simulation, there are 1000 MCMC samples generated. The

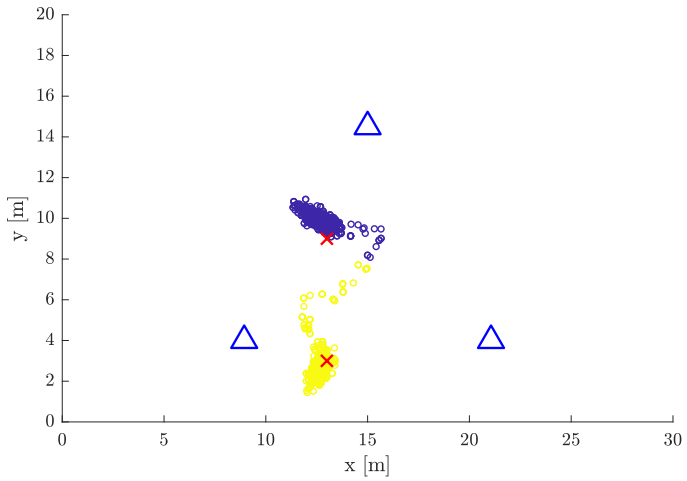

(a) $\mathbf{\Psi} = \mathrm{I}$.

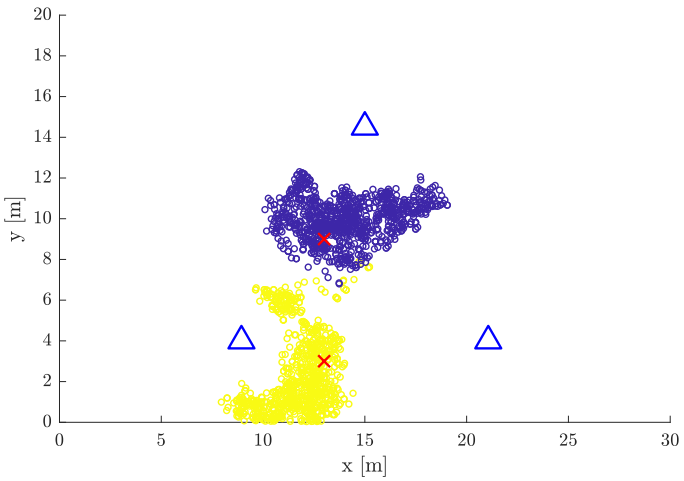

(b) $\mathbf{\Psi} = \sigma_{\varepsilon}^2 \mathrm{I}$.

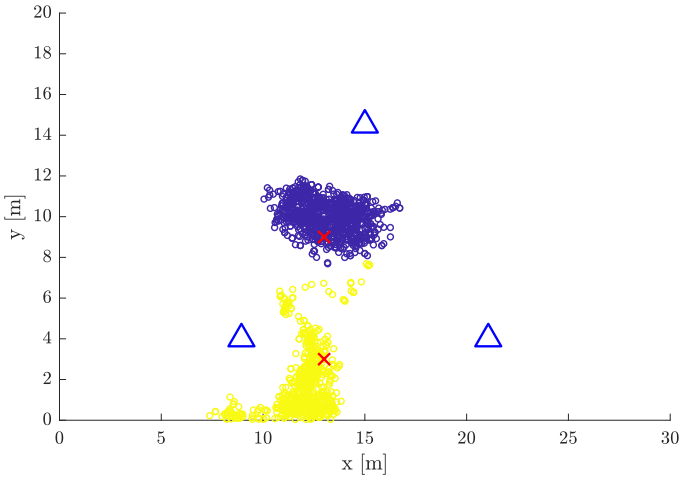

(c) $\mathbf{\Psi} = \mathbf{\Sigma}_{\varepsilon}$.

Figure 4.1: MCMC samples drawn from posteriors with difference IW hyperparameters.

degree-of-free parameter is set to the dimension of shadowing covariance, $v = mn+2$, which meets requirements of IW distribution and further makes the expected value of shadowing covariance equal to the scale matrices. For different simulation, the scale matrices adopts different assumptions, give as 1) identity matrix I, 2) diagonal matrix $\sigma_{\varepsilon}^2 \mathrm{I}$, and 3) true shadowing covariance $\mathbf{\Sigma}_{\varepsilon}$.

4.3.4.1 Mean of Samples

The target location estimates are computed as the mean of MCMC samples obtained after burn-in period (4.32). By investigating the results given in Figure 4.1, it is noticeable that the sample means do not always overlap the true location of

targets. One of the reasons for it is that there exist the local maximums, e.g., the small cluster of yellow sample points apart from the larger cluster. This is a common situation of multi-dimensional problems. Another reason is the shadowing attenuations are relatively high in quantity compared with the noise-free RSS. So the effect of shadowing cannot be completely avoided in localisation.

4.3.4.2 Spread of Samples

The other aspect that can be studied from Figure 4.1 is the spread of samples. On the one hand, with smaller shadowing variance (identity shadowing covariance), the MCMC samples in Figure 4.1a are more concentrated around the true target locations than Figure 4.1b (diagonal shadowing covariance).

On the other hand, it is not hard to realise that more information provided when making inferences, more concentration the sample will be. Taking examples of Figure 4.1b and Figure 4.1c, the latter adopts the true shadowing covariance as hyperparameter which carries more information about shadowing correlation in the off-diagonal elements compared with the only-diagonal matrix for the former. Consequently, the MCMC samples in Figure 4.1c are more concentrated.

4.3.4.3 Convergence of MCMC

As introduced previously, for a designed MCMC, the probability of states will gradually converge to the target distribution. From the visual point of view, the sample points propagate from the initial points, and will eventually move to and wander around the actual target locations.

For localisation, the convergence of MCMC process is important in the aspects of capability and efficiency. The capability of convergence refers to whether the MCMC will finally generate samples concentrated around the actual target location rather than a local maximum or even be non-convergence, while efficiency indicates how fast the convergence would be and how long the burn-in would take. By investigating the simulation results, there are two major factors found that have significant influences

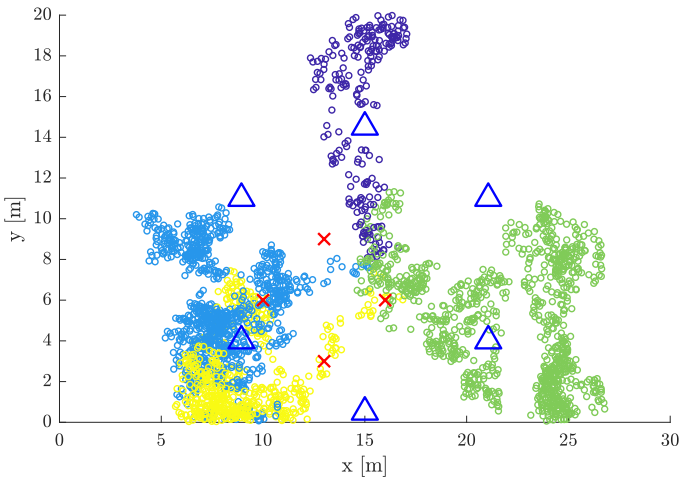

(a) $\mathbf{\Psi} = \mathrm{I}$

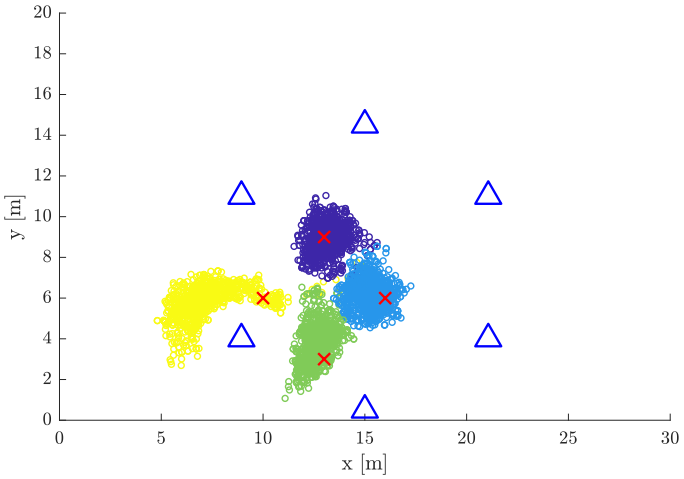

(b) $\mathbf{\Psi} = \mathbf{\Sigma}_{\varepsilon}$

Figure 4.2: MCMC samples drawn from posteriors with difference IW hyperparameters.

on the MCMC convergence.

Since the Metropolis-Hastings method adopts "random walk" searching strategy which is essential "blind" searching, the step size of random walk is the first vital factor that affects the convergence. The selection of searching step size is technical and case-specific. The trick is to balance the convergence efficiency and capability. More precisely,

- With a large random walk length, the new sample might be spawn far from the previous one. Consequently, it has a higher probability to jump out of the local maxima/minima but has a lower probability to be accepted and consequently reduce the efficiency of convergence, especially for a high-dimensional problem.

- With a small random walk length, the new sample might be drawn near to the previous one. Consequently, it has a higher probability to be accepted but might be stuck in the local maxima/minima.

The Figure 4.2 illustrates alternative simulation tests of the proposed MCMC based localisation approach. There are $m = 6$ base stations and $n = 4$ targets where consequently the dimension of the problem increases to $mn = 24$. The RSS measurements and shadowing covariance are generated under the same models and the same parameter configurations as the previous test. To compute the target location posterior, again different values of IW hyperparameter $\mathbf{\Psi}$ are adopted, including the identity matrix and true shadowing covariance.

With the same random walk step size, in Figure 4.1 the identity IW scale matrix hyperparameter produces more concentrated samples than the true shadowing covariance, while contrarily in Figure 4.2 the MCMC samples could not converge under identity scale matrix condition and the true shadowing covariance produces better samples. Therefore, it is clear that the sampling result is influenced by the specifics of target distribution. More precisely,

- Depending on the practical scenario, a "sharp" target distribution might result in
  - concentration of samples (Figure 4.1a),
  - failure of sampling convergence due to "poor guidance" of sample acceptance (Figure 4.2a). More precisely, a too "sharp" target distribution might have too "flat" "off-central area", which results in high acceptance ratios. Therefore, "poor quality" samples will be accepted.
- Similarly, depending of the practical scenario, a "flat" target distribution might results in
  - "better guidance" of sample acceptance due to better probability gradient in "off-central area". (Figure 4.2b), or

– samples spread too much due to the "flatness" of overall target distribution (Figure 4.1c).

In summary, though the MCMC sampler can be used to generate samples from a complex multidimensional probability distribution, the samples are significantly and complicatedly affected by searching mechanism and target distribution. Therefore, estimating the target locations as the mean of samples has obvious shortcomings.

4.4 Maximum A Posterior/Maximum Likelihood Estimate

Given the posterior of target location, the aim here is to obtain the estimate according to the posterior. Except for producing samples from the posterior and making estimate based on the sample mean, a more "directive" approach is the MAP estimate. In other words, the MAP estimate believes that the most possible location for targets will achieve the maximum value of posterior.

The MAP estimate is closely related to the maximum likelihood (ML) estimate. In this work, if the target locations are considered priorly uninformed and following a uniform distribution, the estimate that has achieved the maximum of posterior given in (4.16) will also achieve the maximum of IW marginalised likelihood as given in (4.23), which is

$$\hat{\mathbf{s}} = \max_{\mathbf{s}\in\mathbb{R}} p(\mathbf{s} \mid \mathbf{z}) = \int p(\mathbf{z} \mid \mathbf{s}, \boldsymbol{\Sigma}_\varepsilon) \cdot p(\boldsymbol{\Sigma}_\varepsilon)\, d\boldsymbol{\Sigma}_\varepsilon, \text{ if } p(\mathbf{z}) \text{ is uniform.} \tag{4.33}$$

Substitute the IW marginalised likelihood with (4.23), the above expression can be further derived as

$$\hat{\mathbf{s}} = \max_{\mathbf{s}\in\mathbb{R}} \frac{1}{(2\pi)^{\frac{mn}{2}}} \cdot \frac{|\boldsymbol{\Psi}|^{\frac{v}{2}}}{2^{\frac{vn}{2}}\Gamma_n(\frac{v}{2})} \cdot \frac{2^{\frac{(v+1)n}{2}}\Gamma_n(\frac{v+1}{2})}{|\boldsymbol{\Phi}+\boldsymbol{\Psi}|^{\frac{v+1}{2}}} \tag{4.34a}$$

$$= \min_{\mathbf{s}\in\mathbb{R}} |\boldsymbol{\Phi}+\boldsymbol{\Psi}|, \tag{4.34b}$$

where from (4.34a) to (4.34b) all the constant values have been ignored and the optimisation operator has been changed from "maximisation" to "minimisation" due to the monotonicity of reciprocal function and power function.

If the scale matrix is identity, the optimisation can be further derived as [79]

$$\hat{\mathbf{s}} = \min_{\mathbf{s}\in\mathbb{R}} \ |\mathrm{I} + \mathbf{\Phi}| \tag{4.35a}$$

$$= \min_{\mathbf{s}\in\mathbb{R}} \ \left|\mathrm{I} + (\mathbf{z}-\mathbf{f})(\mathbf{z}-\mathbf{f})^{\mathsf{T}}\right| \tag{4.35b}$$

$$= \min_{\mathbf{s}\in\mathbb{R}} \ 1 + (\mathbf{z}-\mathbf{f})^{\mathsf{T}}(\mathbf{z}-\mathbf{f}), \tag{4.35c}$$

Hereby, if the IW adopts identity scale matrix, the MAP/ML estimate coincides with the least square estimate.

In cases where the IW adopts non-identity matrix as scale matrix, the computation of the determinant is too complex to have an explicit form, and therefore there is no clear conclusion.

4.4.1 Simulation Validation and Results Analysis

The proposed MAP/ML location estimation approach have been tested in simulation. The test bed in given in Figure 4.3. There are $m = 6$ base stations and $n = 4$ targets. The RSS measurements including correlated shadowing noises are generated according to (4.1), (4.2) and (2.7). All necessary parameters are as the same as listed in Table 4.1 expect for the shadowing standard deviation σ_ε.

As for comparison, a practically standard solution where the likelihood adopts the multivariate Gaussian distribution with a specific shadowing covariance assumption is considered. Therefore, the likelihood is given by (4.18). Similarly, the shadowing covariance could have forms of identity matrix or the true one. Via further investigation, the MAP/ML estimate for the standard multivariate Gaussian likelihood is equivalent to the weighted least square estimate, that is

$$\hat{\mathbf{s}} = \max_{\mathbf{s}\in\mathbb{R}} \ p(\mathbf{z} \mid \mathbf{s}, \mathbf{\Sigma}_\varepsilon) \tag{4.36a}$$

$$= \max_{\mathbf{s}\in\mathbb{R}} \frac{1}{(2\pi)^{\frac{mn}{2}} |\mathbf{\Sigma}_\varepsilon|^{\frac{1}{2}}} \exp\left[-\frac{1}{2}(\mathbf{z}-\mathbf{f})^\mathsf{T}\mathbf{\Sigma}_\varepsilon^{-1}(\mathbf{z}-\mathbf{f})\right] \tag{4.36b}$$

$$= \min_{\mathbf{s}\in\mathbb{R}} (\mathbf{z}-\mathbf{f})^\mathsf{T}\mathbf{\Sigma}_\varepsilon^{-1}(\mathbf{z}-\mathbf{f}). \tag{4.36c}$$

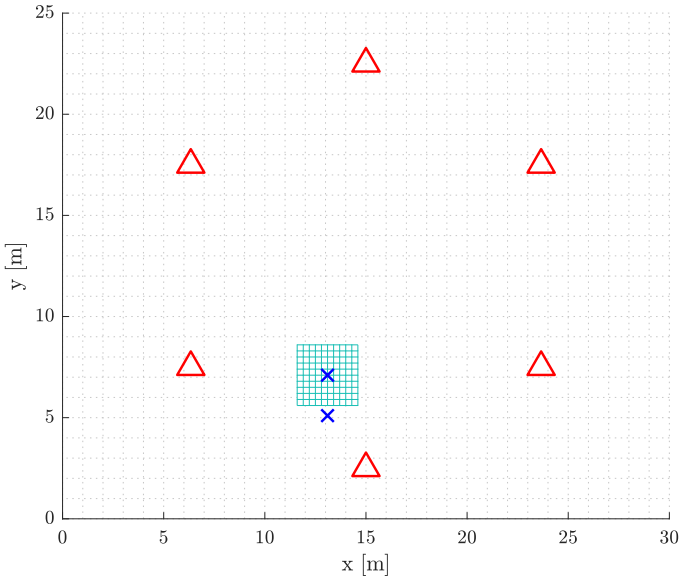

Figure 4.3: Grid based searching.

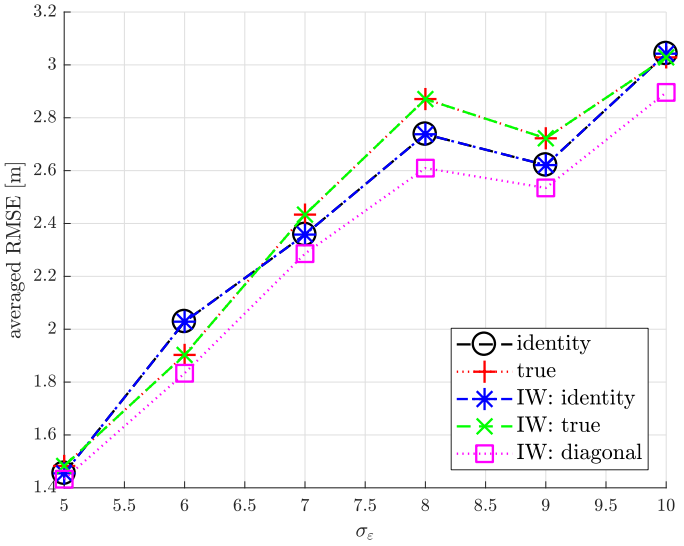

Figure 4.4: The RMSE of grid-based MAP estimate as a function shadowing standard deviation σ_ε based on 150 Monte Carlo runs.

The proposed MAP/ML localisation approach and the comparison approach have been tested under two searching strategies. Firstly, in order to avoid the searching getting stuck in local maximums, a grid-based searching is performed as shown in Figure 4.3. The square area of 3m by 3m around the target location is divided into

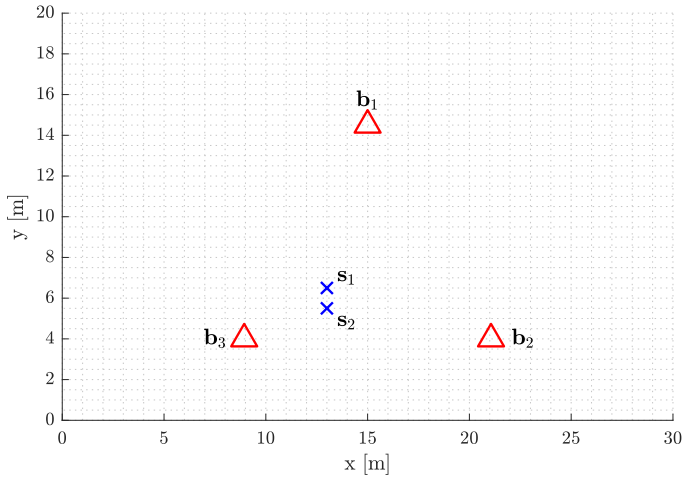

Figure 4.5: The second test beds for MAP/ML based estimation approaches.

grids of size 0.3m by 0.3m. The posterior/likelihood values are computed for all grid points, and the one that achieves the maximum posterior/likelihood is given as the target location estimate.

Figure 4.4 depicts the root mean square error (RMSE) of grid-based MAP/ML estimate of target locations for different approaches as a function shadowing standard deviation. The "identity" and "true" stand for the comparison approaches where the shadowing covariances have identity form and true value respectively. The "IW: identity", "IW: true" and "IW: diagonal" stand for the proposed IW approaches where the scale matrices have the identity, true shadowing covariance and diagonal matrix respectively. All the RMSE results are calculated based on 150 Monte Carlo runs.

As shown, the likelihoods with the same assumptions provide similar performances, while the two likelihoods adopting the true shadowing covariance produce the same results as well. In conclusion, it verifies that the proposed IW marginalised likelihood achieves the maximum at the same location as the standard Gaussian likelihood with the same shadowing covariance assumption, and furthermore coincides with the weighted least square estimate with the same assumption. Overall, all the approaches produce location estimates with acceptable accuracies referring to the scale of shadowing noises.

The second testing scenario is demonstrated in Figure 4.5. There are $m = 3$

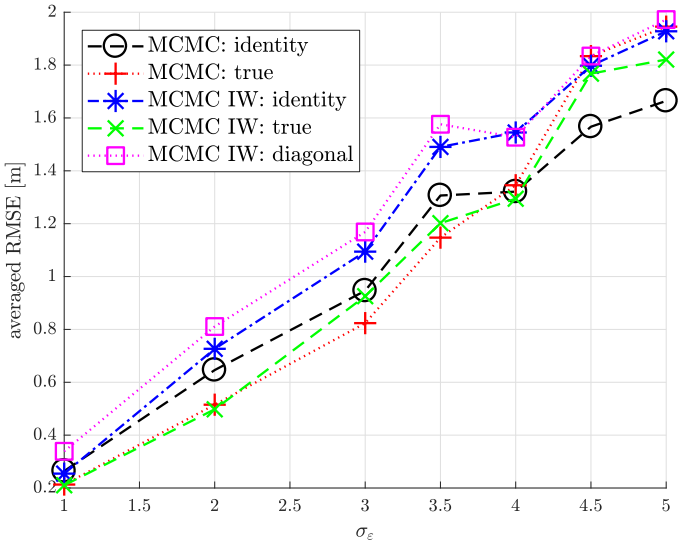

(a) $\sigma_\varepsilon \in [1, 5]$

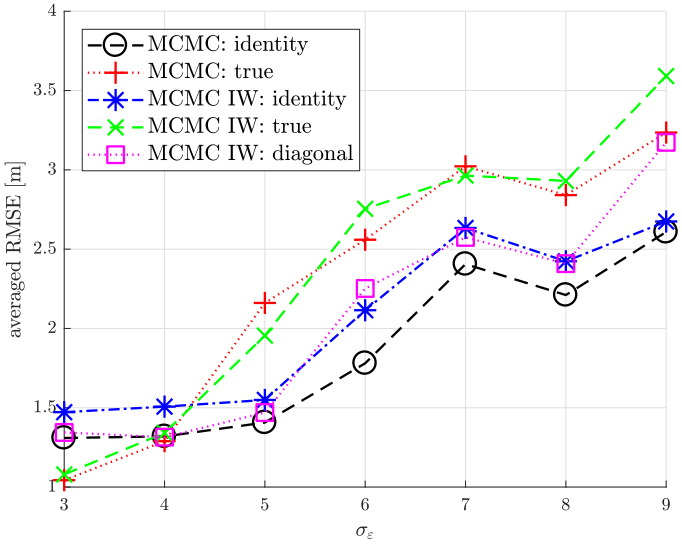

(b) $\sigma_\varepsilon \in [3, 9]$

Figure 4.6: RMSE of MCMC-based MAP/ML estimate as a function of shadowing standard deviation based on 50 Monte Carlo runs.

base stations and $n = 2$ targets which meet the basic compositions of multi-target localisation. Again, RSS measurements that involving correlation shadowing noises are generated based on (4.1), (4.2) and (2.7), while parameters involved are as same as listed in 4.1 except for the shadowing standard deviation.

Except for grid-based searching which is extremely time-consuming, the aforementioned Metropolis-within-Gibbs method is applied here to perform guided searching. After obtaining the samples, the one that achieves the maximum posterior is given as the target location estimate. The comparison approaches are as same as

employed in the first testing scenario.

Figure 4.6 demonstrates the RMSE MCMC-based MAP/ML location estimate as a function of shadowing standards deviation. The Figure 4.6a shows results where the shadowing SD varies from 1dB to 5dB, while the Figure 4.6b shows lager shadowing SD that varies from 3dB to 9dB.

Unfortunately, although there are differences between approaches, the trend of the performance are not consistent. There are two possible reason: firstly, referring the grid-based MAP/ML result, the gaps between different estimation approaches are too small; secondly, as analysed previously, the performance of MCMC sampler are controlled by several factors in complex manners. However, all the approaches produce location estimates with acceptable accuracies referring to the scale of shadowing noises.

4.5 Summary

In this chapter, a new approach of Bayesian inference on target location posterior is proposed. To take advantage of correlated shadowing noises, the IW conjugate prior is studied, and a new likelihood can be computed by marginalising the shadowing covariance.

To estimate target locations, the MCMC sampler is considered to generate samples from the posterior and further produce the estimate as the mean of samples. The MCMC sampler employed here is the Metropolis-within-Gibbs sampler, which follows "random walk" manner. Simulations are conducted, and the performances of MCMC sampler under different assumptions of IW hyperparameters are investigated. It has been found that the quality of MCMC samples is significantly and complexly affected by several factors, such as the step size of random walk and the specifics of the posterior function.

An alternative to estimate target location is the MAP/ML approach. To validate the proposed method, the grid-based searching strategy is considered to produce the location estimate under different scales of shadowing noise. It has been found that

under the same shadowing covariance assumption (identity matrix or true covariance matrix) the MAP/ML estimates produce the similar results as the standard solution of Gaussian likelihood and the weighted least square method. Moreover, the aforementioned MCMC method is proposed as another searching tools. After obtaining enough samples from the target location posterior, the one that achieved the maximum posterior/likelihood value is given as the target location estimate. The MCMC-based MAP/ML approaches with different shadowing covariance assumptions are tested against the scale of shadowing noise. Overall, the localisation results achieve acceptable accuracies.

Chapter 5

TDOA-FDOA based Localisation with Linear Nuisance Parameters[1]

Source geolocation refers to identifying the spatial position of a source on Earth using signal measurements such as the received signal strength (RSS), time of arrival (TOA) and time difference of arrival (TDOA) [80], [81]. When the source is static, its position can be uniquely determined using a dual-satellite geolocation system with two satellites that are moving relatively to the source. First, the TDOA and frequency difference of arrival (FDOA) of the source signal received by the two satellites are estimated. The obtained TDOA and FDOA measurements are then exploited together with the source altitude information to achieve source geolocation using, e.g., the algebraic algorithm in [82], or in reverse, determine the satellite orbits [83], [84]. Dual-satellite geolocation systems have found civilian and military applications including locating the ground interference to commercial satellites [85], [86] and space electronic reconnaissance [87].

The estimation of the source TDOA and FDOA requires joint processing of the source signals received at the two satellites, e.g., computing the cross ambiguity function (CAF) [88]–[90]. Therefore, precise time synchronisation and frequency locking between the two satellites are needed for measuring TDOA and FDOA with

[1]In statistics, a nuisance parameter is any parameter which is not of immediate interest but which must be accounted for in the analysis of those parameters which are of interest, Which indicates the time and frequency offsets in TDOA and FDOA models.

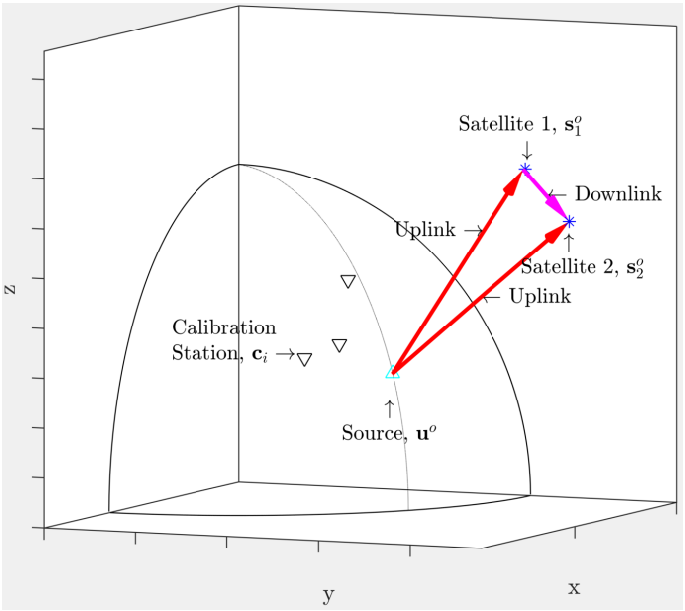

Figure 5.1: Short-baseline dual-satellite geolocation scenario. Satellite 2 estimates the source and calibration TDOAs and FDOAs for source geolocation via cross-correlating the received downlink signal from satellite 1 and its own uplink signal.

high accuracy. However, in practice, time and frequency alignment could be difficult to attain. Consider the geolocation scenario shown in Figure 5.1 for example, where satellite 1 transfers its received signal using a bent pipe transponder [91]. The TDOA and FDOA are estimated via cross-correlating the *downlink* signal from satellite 1 and the *uplink* signal from satellite 2. The obtained TDOA and FDOA may be subject to unknown time and frequency offsets, due to inaccurate knowledge on the group delay and local frequency of the satellite 1 transponder.

If the time and frequency offsets are small, they can be neglected in source geolocation and this would generally lead to biased source position estimates (see e.g., the analysis in [92]). When they have large absolute values, existing TDOA-FDOA geolocation algorithms such as those developed in [82], [87], [93] generally fail to produce a reasonable solution. This is because with only a pair of source TDOA and FDOA, it is not sufficient to geolocate the source while simultaneously estimating the time and frequency offsets. In other words, in the absence of time synchronisation and frequency locking, the source position may become unidentifiable.

Precise knowledge on the satellite location information[2] is also essential for

[2]For simplicity, the satellite location is used in this work to represent satellite position and

achieving satisfactory geolocation performance. It is well known that the presence of satellite location errors can significantly degrade the TDOA-FDOA geolocation accuracy [93]–[95]. However, the satellite location errors are almost inevitable because the satellites are moving and/or they are in orbits distant from Earth, which makes accurate satellite locations difficult to obtain.

In this work, the use of calibration stations at known positions is investigated to improve the geolocation performance of the dual-satellite system when the two satellites have imperfect time and frequency alignment as well as erroneous locations. It is assumed that the source and calibration TDOAs and FDOAs are obtained within a short interval such that they are subject to the same time and frequency offsets and the same satellite location errors [96]–[98]. A new closed-form source geolocation algorithm is proposed for the above problem. In particular, it first fuses the measurements from the unknown source and calibration stations using a best linear unbiased estimator (BLUE) [99]. The time and frequency offsets are eliminated in the fusion process, and the presence of satellite location errors is appropriately taken into account in the weighting matrix. The measurement fusion step only produces a single pair of source TDOA and FDOA, which is then utilised by an existing algebraic technique for source geolocation. The developed algorithm has low computational complexity, and more importantly, theoretical performance analysis shows that it can attain the Cramér-Rao lower bound (CRLB) under Gaussian noise and mild conditions. We illustrate the performance of the proposed algorithm via simulations based on the dual-satellite geolocation scenario shown in Figure 5.1, which is challenging due to the short baseline between the two satellites. The obtained simulation results corroborate the theoretical developments.

This work is different from [100] where precise sensor locations were assumed and source localisation was achieved using a sequence of source TDOAs and FDOAs received during a short interval. A maximum likelihood (ML) estimator that jointly identifies the source position, as well as time and frequency offsets, was used in [100].

velocity.

It is iterative and computationally intensive. In [92], [101]–[104], several techniques were proposed to deal with the problem of node localisation in the presence of unknown clock offset in sensor networks. However, they all involved joint time synchronisation and node localisation based on iterative convex optimisation [101] or closed-form methods [92], [102], [103]. Moreover, except for [103], they assumed accurate sensor locations.

This work is closely related to [105]–[108]. In [105], [106], the clock offset was removed by forming differential TDOAs for node localisation. They did not consider sensor position errors, and an iterative ML location estimator was used. The algorithm developed in [107] eliminated the clock bias via the use of asymmetric trip ranging (ATR). This protocol required the target node to be cooperative, which may not be fulfilled in the dual-satellite geolocation problem considered in this work. In [108], the sensors used for TDOA localisation were partitioned into groups. Each group had a different clock offset, which was cancelled out by taking differences between the TDOA measurements within each group. In contrast, the algorithm proposed in this work eliminates the time and frequency offsets in all the measurements and fuses them using a BLUE to generate only a pair of source TDOA and FDOA for source geolocation.

The rest of the chapter is organised as follows. The geolocation problem is formulated in Section 5.1. The geolocation CRLB is derived in Section 5.2. The proposed geolocation algorithm together with its performance analysis is presented in 5.3. Simulation results are given in Section 5.4. Summary are drawn in Section 5.5.

5.1 Problem Formulation

We consider locating a static source on Earth whose unknown position is denoted by $\mathbf{u}^o = [u_x^o, u_y^o, u_z^o]^T$. Under the oblate spheroidal Earth model specified in World Geodetic System 1984 (WGS84), $\mathbf{u}^o$ is related to the source geodetic latitude ϕ and

longitude φ via [109]

$$u_x^o = (r+h)\cos(\phi)\cos(\varphi) \tag{5.1a}$$

$$u_y^o = (r+h)\cos(\phi)\sin(\varphi) \tag{5.1b}$$

$$u_z^o = (r(1-e^2)+h)\sin(\phi) \tag{5.1c}$$

where $r = \frac{r_e}{\sqrt{1-e^2\sin^2\phi}}$, $r_e = 6378.137$ km is the equatorial radius, $e = 0.081819190842$ is the eccentricity, and h is the source altitude which is assumed to be known.

The dual-satellite system receives the source signal and computes the TDOA and FDOA between the two satellites. Let $\mathbf{s}_i^o = [s_{x,i}^o, s_{y,i}^o, s_{z,i}^o]^T$ and $\dot{\mathbf{s}}_i^o = [\dot{s}_{x,i}^o, \dot{s}_{y,i}^o, \dot{s}_{z,i}^o]^T$ be the true geocentric position and velocity of satellite i, $i = 1, 2$. Without time synchronisation and frequency locking, the estimated source TDOA and FDOA can be expressed as [100], after being multiplied respectively with the signal propagation speed and the source signal wavelength,

$$y_u = d_u^o + \tau + \Delta y_u \tag{5.2a}$$

$$\dot{y}_u = \dot{d}_u^o + \delta + \Delta \dot{y}_u. \tag{5.2b}$$

τ and δ are the unknown time and frequency offsets between the two satellites. d_u^o and $\dot{d}_u^o$ are the true source TDOA and FDOA, and they are equal to

$$d_u^o = ||\mathbf{u}^o - \mathbf{s}_1^o|| - ||\mathbf{u}^o - \mathbf{s}_2^o|| \tag{5.3a}$$

$$\dot{d}_u^o = \frac{-(\mathbf{u}^o - \mathbf{s}_1^o)^T \dot{\mathbf{s}}_1^o}{||\mathbf{u}^o - \mathbf{s}_1^o||} - \frac{-(\mathbf{u}^o - \mathbf{s}_2^o)^T \dot{\mathbf{s}}_2^o}{||\mathbf{u}^o - \mathbf{s}_2^o||} \tag{5.3b}$$

where $||\cdot||$ represents the Euclidean distance. For notation simplicity, we collect y_u and $\dot{y}_u$ to form the source measurement vector $\mathbf{y}_u = [y_u, \dot{y}_u]^T$. Moreover, we introduce

$$\boldsymbol{\alpha}^o = [\tau, \delta]^T \tag{5.4}$$

to collect the time and frequency offsets. Note that with only $\mathbf{y}_u$, the source position

is unidentifiable, due to the presence of the additional unknown $\boldsymbol{\alpha}^o$.

The true satellite location information is not available. The geolocation algorithm only has access to noisy observations of $\mathbf{s}_i^o$ and $\dot{\mathbf{s}}_i^o$, which are denoted as

$$\mathbf{s}_i = \mathbf{s}_i^o + \Delta\mathbf{s}_i \tag{5.5a}$$

$$\dot{\mathbf{s}}_i = \dot{\mathbf{s}}_i^o + \Delta\dot{\mathbf{s}}_i. \tag{5.5b}$$

Collecting the known satellite locations yields $\boldsymbol{\beta} = [\mathbf{s}_1^T, \dot{\mathbf{s}}_1^T, \mathbf{s}_2^T, \dot{\mathbf{s}}_2^T]^T$. Its true value is $\boldsymbol{\beta}^o = [\mathbf{s}_1^{oT}, \dot{\mathbf{s}}_1^{oT}, \mathbf{s}_2^{oT}, \dot{\mathbf{s}}_2^{oT}]^T$. The satellite location error vector is denoted by $\Delta\boldsymbol{\beta} = \boldsymbol{\beta} - \boldsymbol{\beta}^o = [\Delta\mathbf{s}_1^T, \Delta\dot{\mathbf{s}}_1^T, \Delta\mathbf{s}_2^T, \Delta\dot{\mathbf{s}}_2^T]^T$, which is assumed to be zero-mean Gaussian distributed with covariance matrix $\mathbf{Q}_\beta$ [93], [96]–[98], [103], [108].

There are N ground calibration stations at known positions $\mathbf{c}_n = [c_{x,n}, c_{y,n}, c_{z,n}]^T$, $n = 1, 2, ..., N$, deployed to improve the geolocation accuracy in the absence of time and frequency alignment between satellites and precise satellite locations. When the measurements from the unknown source and calibration stations are obtained during a short interval, they would be subject to the same time and frequency offsets. As a result, the calibration TDOAs and FDOAs can be modelled similarly to (5.2) as

$$y_{c,n} = d_{c,n}^o + \tau + \Delta y_{c,n} \tag{5.6a}$$

$$\dot{y}_{c,n} = \dot{d}_{c,n}^o + \delta + \Delta\dot{y}_{c,n}. \tag{5.6b}$$

where $d_{c,n}^o$ and $\dot{d}_{c,n}^o$ are the true TDOA and FDOA from the n-th calibration station and are equal to

$$d_{c,n}^o = ||\mathbf{c}_n - \mathbf{s}_1^o|| - ||\mathbf{c}_n - \mathbf{s}_2^o|| \tag{5.7a}$$

$$\dot{d}_{c,n}^o = \frac{-(\mathbf{c}_n - \mathbf{s}_1^o)^T\dot{\mathbf{s}}_1^o}{||\mathbf{c}_n - \mathbf{s}_1^o||} - \frac{-(\mathbf{c}_n - \mathbf{s}_2^o)^T\dot{\mathbf{s}}_2^o}{||\mathbf{c}_n - \mathbf{s}_2^o||}. \tag{5.7b}$$

It can be seen from (5.6) that with calibration stations, the source position becomes identifiable because there are $(N+1) \geq 2$ pairs of measurements, which are sufficient to determine the source position and time and frequency offsets.

Collecting $y_{c,n}$ and $\dot{y}_{c,n}$, and stacking the results over n yield the calibration measurement vector $\mathbf{y}_c = [\mathbf{y}_{c,1}^T, \mathbf{y}_{c,2}^T, ..., \mathbf{y}_{c,N}^T]^T$, where $\mathbf{y}_{c,n} = [y_{c,n}, \dot{y}_{c,n}]^T$. Combining the source measurement vector $\mathbf{y}_u$ with $\mathbf{y}_c$ yields the composed measurement vector $\mathbf{y} = [\mathbf{y}_u^T, \mathbf{y}_c^T]^T$. According to (5.2) and (5.6), the true value of $\mathbf{y}$ can be expressed as

$$\mathbf{y}^o = [\mathbf{d}_u^{oT}, \mathbf{d}_{c,1}^{oT}, \mathbf{d}_{c,2}^{oT}, ..., \mathbf{d}_{c,N}^{oT}]^T + \mathbf{G}\boldsymbol{\alpha}^o. \tag{5.8}$$

The coefficient matrix $\mathbf{G}$ is equal to

$$\mathbf{G} = \mathbf{1}_{(N+1)\times 1} \otimes \mathbf{I}_{2\times 2} \tag{5.9}$$

where $\otimes$ denotes the Kronecker product, $\mathbf{1}_{(N+1)\times 1}$ denotes a $(N+1) \times 1$ column vector of ones and $\mathbf{I}_{2\times 2}$ represents a 2×2 identity matrix. The vectors $\mathbf{d}_u^o$ and $\mathbf{d}_{c,n}^o$ are defined as

$$\mathbf{d}_u^o = [d_u^o, \dot{d}_u^o]^T \tag{5.10a}$$

$$\mathbf{d}_{c,n}^o = [d_{c,n}^o, \dot{d}_{c,n}^o]^T. \tag{5.10b}$$

The measurement noise in $\mathbf{y}$ can be shown to be

$$\Delta\mathbf{y} = \mathbf{y} - \mathbf{y}^o = [\Delta y_u, \Delta\dot{y}_u, \Delta y_{c,1}, \Delta\dot{y}_{c,1}, ..., \Delta y_{c,N}, \Delta\dot{y}_{c,N}]^T. \tag{5.11}$$

As in [96]–[98], it is assumed that $\Delta\mathbf{y}$ is a zero-mean Gaussian random vector with covariance matrix $\mathbf{Q}_y$ and $\Delta\mathbf{y}$ is also independent of the satellite location error $\Delta\boldsymbol{\beta}$.

We are interested in estimating at a low computational cost the source position $\mathbf{u}^o$ using the source and calibration TDOAs and FDOAs in $\mathbf{y}$ as well as the noisy satellite locations in $\boldsymbol{\beta}$.

5.2 CRLB Analysis and Insights

This section derives the CRLB of $\mathbf{u}^o$, denoted by CRLB($\mathbf{u}^o$). For this purpose, note that according to the previous section, besides the source position $\mathbf{u}^o$, the time and frequency offsets in $\boldsymbol{\alpha}^o$ and true satellite location vector $\boldsymbol{\beta}^o$ are also unknown. As the source altitude h is known, the CRLB of $[\mathbf{u}^{oT}, \boldsymbol{\alpha}^{oT}, \boldsymbol{\beta}^{oT}]^T$ would be an equality-constrained one [110]. To simplify the derivation, we follow the re-parametrisation approach [111] and establish CRLB($\mathbf{u}^o$) via relating it to the CRLB of $\boldsymbol{\theta}^o = [\phi, \varphi]^T$, where ϕ and φ are the source geodetic latitude and longitude (5.1). Specifically, we have [99]

$$\text{CRLB}(\mathbf{u}^o) = \left(\frac{\partial \mathbf{u}^o}{\partial \boldsymbol{\theta}^o}\right) \cdot \text{CRLB}(\boldsymbol{\theta}^o) \cdot \left(\frac{\partial \mathbf{u}^o}{\partial \boldsymbol{\theta}^o}\right)^T. \tag{5.12}$$

To find CRLB($\boldsymbol{\theta}^o$), we need to derive the CRLB of the composed unknown vector $\boldsymbol{\eta}^o = [\boldsymbol{\theta}^{oT}, \boldsymbol{\alpha}^{oT}, \boldsymbol{\beta}^o]^T$ first. Express $\boldsymbol{\eta}^o$ as $\boldsymbol{\eta}^o = [\boldsymbol{\gamma}^{oT}, \boldsymbol{\beta}^o]^T$, where $\boldsymbol{\gamma}^o = [\boldsymbol{\theta}^{oT}, \boldsymbol{\alpha}^{oT}]^T$ contains the source position as well as time and frequency offsets.

Note from Section 5.1 that the composed TDOA and FDOA measurement vector $\mathbf{y}$ and the known satellite locations $\boldsymbol{\beta}$ are jointly Gaussian distributed. Taking logarithm of this joint distribution, differentiating it twice with respect to $\boldsymbol{\eta}^o$, negating the sign and taking expectation yields the Fisher information matrix (FIM) of $\boldsymbol{\eta}^o$ [99]. The partitioned matrix form of FIM($\boldsymbol{\eta}^o$) is

$$\text{FIM}(\boldsymbol{\eta}^o) = \begin{bmatrix} \mathbf{X} & \mathbf{Y} \\ \mathbf{Y}^T & \mathbf{Z} \end{bmatrix}. \tag{5.13}$$

The matrix partitions are defined as

$$\mathbf{X} = \left(\frac{\partial \mathbf{y}^o}{\partial \boldsymbol{\gamma}^o}\right)^T \mathbf{Q}_y^{-1} \left(\frac{\partial \mathbf{y}^o}{\partial \boldsymbol{\gamma}^o}\right) \tag{5.14a}$$

$$\mathbf{Y} = \left(\frac{\partial \mathbf{y}^o}{\partial \boldsymbol{\gamma}^o}\right)^T \mathbf{Q}_y^{-1} \left(\frac{\partial \mathbf{y}^o}{\partial \boldsymbol{\beta}^o}\right) \tag{5.14b}$$

$$\mathbf{Z} = \mathbf{Q}_\beta^{-1} + \left(\frac{\partial \mathbf{y}^o}{\partial \boldsymbol{\beta}^o}\right)^T \mathbf{Q}_y^{-1} \left(\frac{\partial \mathbf{y}^o}{\partial \boldsymbol{\beta}^o}\right). \tag{5.14c}$$

$\mathbf{X}$ is the FIM of $\boldsymbol{\gamma}^o$ when the satellite location errors are absent. Inversing FIM($\boldsymbol{\eta}^o$) gives CRLB($\boldsymbol{\eta}^o$), and its upper-left 2×2 block is the desired CRLB($\boldsymbol{\theta}^o$).

We shall derive a detailed expression for CRLB($\boldsymbol{\theta}^o$) to gain insights. First, taking the inverse of FIM($\boldsymbol{\eta}^o$) and retaining only the upper-left 4×4 block yield the CRLB of $\boldsymbol{\gamma}^o$, which is given by

$$\text{CRLB}(\boldsymbol{\gamma}^o) = \left(\mathbf{X} - \mathbf{Y}\mathbf{Z}^{-1}\mathbf{Y}^T\right)^{-1}. \tag{5.15}$$

Putting the definitions of $\mathbf{X}$, $\mathbf{Y}$ and $\mathbf{Z}$ and applying the matrix inversion Lemma [99], we arrive at

$$\text{CRLB}(\boldsymbol{\gamma}^o) = \left(\left(\frac{\partial \mathbf{y}^o}{\partial \boldsymbol{\gamma}^o}\right)^T \tilde{\mathbf{Q}}_y^{-1} \left(\frac{\partial \mathbf{y}^o}{\partial \boldsymbol{\gamma}^o}\right)\right)^{-1} \tag{5.16}$$

where

$$\tilde{\mathbf{Q}}_y = \mathbf{Q}_y + \left(\frac{\partial \mathbf{y}^o}{\partial \boldsymbol{\beta}^o}\right) \mathbf{Q}_\beta \left(\frac{\partial \mathbf{y}^o}{\partial \boldsymbol{\beta}^o}\right)^T. \tag{5.17}$$

It is easy to show that $\tilde{\mathbf{Q}}_y - \mathbf{Q}_y$ is positive semi-definite. Moreover, $\tilde{\mathbf{Q}}_y$ is generally not block diagonal, even if the TDOA and FDOA measurements from the source and calibration stations are independent to one another and $\mathbf{Q}_y$ has a block diagonal structure. As a result, by taking the inverse of CRLB($\boldsymbol{\gamma}^o$) in (5.16) and comparing the result with (5.14a), we have that FIM($\boldsymbol{\gamma}^o$) = CRLB($\boldsymbol{\gamma}^o$)$^{-1}$ can be considered as the FIM of $\boldsymbol{\gamma}^o$ when accurate satellite locations are known but the measurements have an increased covariance matrix $\tilde{\mathbf{Q}}_y$. In other words, satellite location errors affect the estimation of the source position and time and frequency offsets via degrading and introducing extra correlation into the source and calibration measurements.

According to the definition $\boldsymbol{\gamma}^o = [\boldsymbol{\theta}^{oT}, \boldsymbol{\alpha}^{oT}]^T$, CRLB($\boldsymbol{\theta}^o$) is given by the upper-left 2×2 block of CRLB($\boldsymbol{\gamma}^o$). To evaluate (5.16), we put (5.8) and express the

partial derivative ($\frac{\partial \mathbf{y}^o}{\partial \boldsymbol{\gamma}^o}$) as

$$\left(\frac{\partial \mathbf{y}^o}{\partial \boldsymbol{\gamma}^o}\right) = \left[\mathbf{H}\left(\frac{\partial \mathbf{d}_u^o}{\partial \boldsymbol{\theta}^o}\right), \mathbf{G}\right] \tag{5.18}$$

where $\mathbf{G}$ is defined in (5.9), the matrix $\mathbf{H}$ is defined as

$$\mathbf{H} = \begin{bmatrix} \mathbf{I}_{2\times 2} \\ \mathbf{O}_{N\times 2} \end{bmatrix} \tag{5.19}$$

and N is the number of calibration stations. Substituting (5.18) into (5.16) and applying the partitioned matrix inversion formula [99] yield

$$\text{CRLB}(\boldsymbol{\theta}^o) = \left(\left(\frac{\partial \mathbf{d}_u^o}{\partial \boldsymbol{\theta}^o}\right)^T \left(\mathbf{H}^T \mathbf{P}_y \mathbf{H}\right) \left(\frac{\partial \mathbf{d}_u^o}{\partial \boldsymbol{\theta}^o}\right)\right)^{-1}. \tag{5.20}$$

which is the desired form for CRLB($\boldsymbol{\theta}^o$). The matrix $\mathbf{P}_y$ is equal to

$$\mathbf{P}_y = \tilde{\mathbf{Q}}_y^{-1} - \tilde{\mathbf{Q}}_y^{-1}\mathbf{G}\left(\mathbf{G}^T\tilde{\mathbf{Q}}_y^{-1}\mathbf{G}\right)^{-1}\mathbf{G}^T\tilde{\mathbf{Q}}_y^{-1}. \tag{5.21}$$

$\mathbf{P}_y$ is in fact a singular matrix, which can be verified as follows. Applying the Cholesky decomposition $\tilde{\mathbf{Q}}_y = \tilde{\mathbf{L}}_y\tilde{\mathbf{L}}_y^T$ to (5.21), we obtain $\mathbf{P}_y = \tilde{\mathbf{L}}_y^{-T}\mathbf{P}\tilde{\mathbf{L}}_y^{-1}$, where

$$\mathbf{P} = \mathbf{I}_{(N+1)\times 2} - \tilde{\mathbf{L}}_y^{-1}\mathbf{G}\left(\mathbf{G}^T\tilde{\mathbf{L}}_y^{-T}\tilde{\mathbf{L}}_y^{-1}\mathbf{G}\right)^{-1}\mathbf{G}^T\tilde{\mathbf{L}}_y^{-T}. \tag{5.22}$$

$\mathbf{P}$ is clearly a projection matrix, which is singular and renders $\mathbf{P}_y$ non-invertible.

Note that the three terms on the right-hand side of (5.20) are all 2×2 matrices. For CRLB($\boldsymbol{\theta}^o$) to be existent, they must be non-singular. Hence, substituting (5.20) back to (5.12) gives

$$\begin{aligned} &\text{CRLB}(\mathbf{u}^o) \\ &= \left(\frac{\partial \mathbf{u}^o}{\partial \boldsymbol{\theta}^o}\right)\left(\frac{\partial \mathbf{d}_u^o}{\partial \boldsymbol{\theta}^o}\right)^{-1}\left(\mathbf{H}^T\mathbf{P}_y\mathbf{H}\right)^{-1}\left(\frac{\partial \mathbf{d}_u^o}{\partial \boldsymbol{\theta}^o}\right)^{-T}\left(\frac{\partial \mathbf{u}^o}{\partial \boldsymbol{\theta}^o}\right)^T. \end{aligned} \tag{5.23}$$

This is the CRLB of the source position $\mathbf{u}^o$ under the considered dual-satellite geolocation scenario where unknown time and frequency offsets between satellites and satellite location errors are present. It lower-bounds the error covariance matrix of any unbiased estimator of $\mathbf{u}^o$. The required partial derivatives, $\left(\frac{\partial \mathbf{u}^o}{\partial \boldsymbol{\theta}^o}\right)$, $\left(\frac{\partial \mathbf{d}_u^o}{\partial \boldsymbol{\theta}^o}\right)$ and $\left(\frac{\partial \mathbf{y}^o}{\partial \boldsymbol{\beta}^o}\right)$, are given in the Appendix B.

Carefully examining (5.23) reveals that the source position CRLB does not depend on the actual values of the time and frequency offsets. More importantly, it has the same functional form as the geolocation CRLB with precise time-frequency alignment between satellites, accurate satellite locations and a source TDOA-FDOA covariance matrix $(\mathbf{H}^T\mathbf{P}_y\mathbf{H})^{-1}$ (see e.g., [82]). The measurements from calibration stations affect the source geolocation performance only through the term $(\mathbf{H}^T\mathbf{P}_y\mathbf{H})^{-1}$. These observations are essential for the low-complexity geolocation algorithm development in the following section.

5.3 A Two-step TDOA-FDOA Geolocation Method

The geolocation algorithm development begins with noting from (5.6) and (5.7) that the TDOA and FDOA measurements from calibration stations are not dependent on the source position $\mathbf{u}^o$. According to the CRLB analysis in Section 5.2, they contribute to the source geolocation accuracy indirectly through providing information on the time and frequency offsets $\boldsymbol{\alpha}^o$ and true satellite locations.

In this section, we shall develop a novel two-step algorithm that avoids the estimation of any extra variables (i.e., the true satellite locations $\boldsymbol{\beta}^o$ as well as the time and frequency offsets $\boldsymbol{\alpha}^o$). Step-1 of the proposed algorithm fuses the TDOA and FDOA measurements from the unknown source and calibration stations using a BLUE. It eliminates $\boldsymbol{\alpha}^o$ and takes into account the presence of satellite location errors in the weighting matrix. The output of Step-1, which is an estimate of the source TDOA and FDOA d_u^o and $\dot{d}_u^o$ (5.3), is utilised in Step-2 of the proposed algorithm for geolocating the source.

5.3.1 A Two-step TDOA-FDOA Geolocation Methods

Step-1: We start with considering the composed measurement vector $\mathbf{y} = \mathbf{y}^o + \Delta\mathbf{y}$ that contains the TDOAs and FDOAs from the source and calibration stations. Note from (5.3) and (5.7) that the true value of $\mathbf{y}$, $\mathbf{y}^o$, depends on the true satellite locations $\boldsymbol{\beta}^o$, which is unknown. We therefore approximate $\mathbf{y}^o$, after applying the first-order Taylor-Series expansion around the known satellite locations $\boldsymbol{\beta}$, as

$$\mathbf{y}^o \approx \hat{\mathbf{y}}^o - \mathbf{D}\Delta\boldsymbol{\beta} \tag{5.24}$$

where

$$\hat{\mathbf{y}}^o = \left[\hat{\mathbf{d}}_u^{oT}, \hat{\mathbf{d}}_{c,1}^T, ..., \hat{\mathbf{d}}_{c,N}^T\right]^T + \mathbf{G}\boldsymbol{\alpha}^o. \tag{5.25}$$

$\hat{\mathbf{d}}_u^o = [\hat{d}_u^o, \hat{\dot{d}}_u^o]^T$ and $\hat{\mathbf{d}}_{c,n} = [\hat{d}_{c,n}.\hat{\dot{d}}_{c,n}]^T$ have the same functional forms as $\mathbf{d}_u^o$ in (5.3) and $\mathbf{d}_{c,n}^o$ in (5.7) except that the true satellite locations $\boldsymbol{\beta}^o$ are replaced with their known but noisy version $\boldsymbol{\beta}$. Mathematically, we have

$$\hat{d}_u^o = ||\mathbf{u}^o - \mathbf{s}_1|| - ||\mathbf{u}^o - \mathbf{s}_2|| \tag{5.26a}$$

$$\hat{\dot{d}}_u^o = \frac{-(\mathbf{u}^o - \mathbf{s}_1)^T\dot{\mathbf{s}}_1}{||\mathbf{u}^o - \mathbf{s}_1||} - \frac{-(\mathbf{u}^o - \mathbf{s}_2)^T\dot{\mathbf{s}}_2}{||\mathbf{u}^o - \mathbf{s}_2||} \tag{5.26b}$$

$$\hat{d}_{c,n} = ||\mathbf{c}_n - \mathbf{s}_1|| - ||\mathbf{c}_n - \mathbf{s}_2|| \tag{5.26c}$$

$$\hat{\dot{d}}_{c.n} = \frac{-(\mathbf{c}_n - \mathbf{s}_1)^T\dot{\mathbf{s}}_1}{||\mathbf{c}_n - \mathbf{s}_1||} - \frac{-(\mathbf{c}_n - \mathbf{s}_2)^T\dot{\mathbf{s}}_2}{||\mathbf{c}_n - \mathbf{s}_2||} \tag{5.26d}$$

where $n = 1, 2, ..., N$. The coefficient matrix $\mathbf{D}$ for the satellite location error $\Delta\boldsymbol{\beta}$ can be shown to be

$$\mathbf{D} = \left(\frac{\partial\hat{\mathbf{y}}^o}{\partial\boldsymbol{\beta}}\right). \tag{5.27}$$

Putting (5.25) and (5.26) into (5.27) and comparing the result with B.4 indicate that $\mathbf{D}$ is equal to the partial derivative $\left(\frac{\partial\mathbf{y}^o}{\partial\boldsymbol{\beta}^o}\right)$ evaluated at the noisy satellite locations $\boldsymbol{\beta}$.

Note from (5.26) that $\hat{\mathbf{d}}_{c,n}$ is indeed a known quantity because the calibration station positions $\mathbf{c}_n$ and satellite locations $\boldsymbol{\beta}$ are both available. Exploring the above

fact and putting (5.25) transform the composed measurement vector $\mathbf{y}$ into

$$\hat{\mathbf{y}} \approx \mathbf{H}\hat{\mathbf{d}}_u^o + \mathbf{G}\boldsymbol{\alpha}^o + (\Delta\mathbf{y} - \mathbf{D}\Delta\boldsymbol{\beta}) \tag{5.28}$$

where $\mathbf{G}$ and $\mathbf{H}$ are defined in (5.9) and (5.19). Besides,

$$\hat{\mathbf{y}} = \mathbf{y} - [\mathbf{0}^T, \hat{\mathbf{d}}_{c,1}^T, ..., \hat{\mathbf{d}}_{c,N}^T]^T. \tag{5.29}$$

We shall estimate the source TDOA and FDOA $\hat{\mathbf{d}}_u^o$ from $\hat{\mathbf{y}}$ to accomplish the desired measurement fusion. For this purpose, note that in (5.28), the noise term $(\Delta\mathbf{y} - \mathbf{D}\Delta\boldsymbol{\beta})$ is zero-mean Gaussian distributed with covariance matrix

$$\hat{\mathbf{Q}}_y = \mathbf{Q}_y + \mathbf{D}\mathbf{Q}_\beta\mathbf{D}^T \tag{5.30}$$

because $\Delta\mathbf{y}$ and $\Delta\boldsymbol{\beta}$ are independent zero-mean Gaussian random vectors with covariance matrices $\mathbf{Q}_y$ and $\mathbf{Q}_\beta$ (see Section 5.1). We eliminate the time and frequency offsets $\boldsymbol{\alpha}^o$ in (5.28) by first pre-whitening the noise in $\hat{\mathbf{y}}$ using $\hat{\mathbf{L}}_y^{-1}$ and then multiplying both sides of (5.28) by the projection matrix

$$\hat{\mathbf{P}} = \mathbf{I}_{(N+1)\times 2} - \hat{\mathbf{L}}_y^{-1}\mathbf{G}\left(\mathbf{G}^T\hat{\mathbf{L}}_y^{-T}\hat{\mathbf{L}}_y^{-1}\mathbf{G}\right)^{-1}\mathbf{G}^T\hat{\mathbf{L}}_y^{-T}. \tag{5.31}$$

Here, $\hat{\mathbf{Q}}_y = \hat{\mathbf{L}}_y\hat{\mathbf{L}}_y^T$ is the Cholesky decomposition of $\hat{\mathbf{Q}}_y$. After these manipulations, (5.28) becomes

$$\hat{\mathbf{P}}\hat{\mathbf{L}}_y^{-1}\hat{\mathbf{y}} = \hat{\mathbf{P}}\hat{\mathbf{L}}_y^{-1}\mathbf{H}\hat{\mathbf{d}}_u^o + \hat{\mathbf{P}}\hat{\mathbf{L}}_y^{-1}(\Delta\mathbf{y} - \mathbf{D}\Delta\boldsymbol{\beta}) \tag{5.32}$$

where $\hat{\mathbf{P}}\mathbf{G} = 0$ has been applied. The BLUE of $\hat{\mathbf{d}}_u^o$ is [99], [112]

$$\hat{\mathbf{d}}_u = [\hat{d}_u, \hat{\dot{d}}_u]^T = \left(\mathbf{H}^T\hat{\mathbf{P}}_y\mathbf{H}\right)^{-1}\mathbf{H}^T\hat{\mathbf{P}}_y\hat{\mathbf{y}} \tag{5.33}$$

where the fact that $\hat{\mathbf{Q}}_y^{-1} = \hat{\mathbf{L}}_y^{-T}\hat{\mathbf{L}}_y^{-1}$ and $\hat{\mathbf{P}}$ is idempotent (i.e., $\hat{\mathbf{P}}^2 = \hat{\mathbf{P}}$) has been

applied, and

$$\hat{\mathbf{P}}_y = \hat{\mathbf{Q}}_y^{-1} - \hat{\mathbf{Q}}_y^{-1}\mathbf{G}\left(\mathbf{G}^T\hat{\mathbf{Q}}_y^{-1}\mathbf{G}\right)^{-1}\mathbf{G}^T\hat{\mathbf{Q}}_y^{-1}. \tag{5.34}$$

This completes the Step-1 processing of the proposed algorithm that fuses the source and calibration measurements.

It is worthwhile to point out that the approach used to cancel $\boldsymbol{\alpha}^o$ in (5.28) is referred to as orthogonal subspace projection (OSP) in some literature [112]–[114]. A recent study [112] showed that results identical to the fusion output in (5.33) can be obtained via jointly estimating $\hat{\mathbf{d}}_u^o$ and $\boldsymbol{\alpha}^o$, or "differential signal processing", where measurement differencing is used to eliminate $\boldsymbol{\alpha}^o$. In this work, we adopt the OSP approach to facilitate the performance analysis of the proposed algorithm.

Step-2: With the source TDOA and FDOA estimates in (5.33), the source position $\mathbf{u}^o$ can be estimated using e.g., the algebraic TDOA-FDOA geolocation technique developed in [82][3] that jointly utilises $\hat{d}_u$, $\hat{\dot{d}}_u$, the source altitude h and known satellite locations $\boldsymbol{\beta}$. The obtained source position estimate, denoted by $\mathbf{u}$, is the algorithm output.

Realising the proposed algorithm requires the evaluation of $\hat{\mathbf{Q}}_y$ defined in (5.30). However, it depends on the unknown source position $\mathbf{u}^o$ through the matrix $\mathbf{D}$ define in (5.27). To address this difficulty, we set $\hat{\mathbf{Q}}_y = \mathbf{Q}_y$ to obtain an initial estimate of $\mathbf{u}^o$ and then plug the result back to (5.27) and (5.30) so that improved estimates of $\hat{\mathbf{Q}}_y$ and $\mathbf{u}^o$ can be obtained. In the algorithm implementation, we do not iterate the above process and simulations show that this approximation does not lead to observable performance degradation.

5.3.2 Performance Analysis

We derive the covariance matrix of the source position estimate $\mathbf{u}$, denoted by $\text{cov}(\mathbf{u})$, and compare it with $\text{CRLB}(\mathbf{u}^o)$. Note that the proposed algorithm finds $\mathbf{u}$ from $\hat{\mathbf{d}}_u$ in (5.33), which is the estimate of the source TDOA and FDOA $\hat{\mathbf{d}}_u^o = [\hat{d}_u^o, \hat{\dot{d}}_u^o]^T$ (5.26). Following the same approach adopted in [82], we can show that

[3]This algorithm was indeed used to generate the simulation results presented in Section 5.4.

$\text{cov}(\mathbf{u})$ is approximately equal to

$$\text{cov}(\mathbf{u}) \approx \left(\frac{\partial \mathbf{u}^o}{\partial \boldsymbol{\theta}^o}\right)\left(\frac{\partial \hat{\mathbf{d}}_u^o}{\partial \boldsymbol{\theta}^o}\right)^{-1} \text{cov}(\hat{\mathbf{d}}_u)\left(\frac{\partial \hat{\mathbf{d}}_u^o}{\partial \boldsymbol{\theta}^o}\right)^{-T}\left(\frac{\partial \mathbf{u}^o}{\partial \boldsymbol{\theta}^o}\right)^{T} \tag{5.35}$$

where $\text{cov}(\hat{\mathbf{d}}_u)$ is the covariance matrix of $\hat{\mathbf{d}}_u$. It can be derived by putting (5.28) into (5.33) and subtracting $\hat{\mathbf{d}}_u^o$ from both sides to obtain the estimation error in $\hat{\mathbf{d}}_u$. Post-multiplying the estimation error with its transpose and taking expectation yield

$$\text{cov}(\hat{\mathbf{d}}_u) = \left(\mathbf{H}^T \hat{\mathbf{P}}_y \mathbf{H}\right)^{-1}. \tag{5.36}$$

Putting (5.36) and comparing (5.35) with (5.23) indicate that

$$\text{cov}(\mathbf{u}) \approx \text{CRLB}(\mathbf{u}^o) \tag{5.37}$$

if $\left(\frac{\partial \hat{\mathbf{d}}_u^o}{\partial \boldsymbol{\theta}^o}\right) \approx \left(\frac{\partial \mathbf{d}_u^o}{\partial \boldsymbol{\theta}^o}\right)$ and $\mathbf{P}_y \approx \hat{\mathbf{P}}_y$ (i.e., $\tilde{\mathbf{Q}}_y \approx \hat{\mathbf{Q}}_y$ or equivalently $\mathbf{D} \approx \left(\frac{\partial \mathbf{y}^o}{\partial \boldsymbol{\beta}}\right)$). It can be verified that the above approximations are valid under the conditions $\Delta\mathbf{s}_i/||\mathbf{u}^o - \mathbf{s}_i^o|| \approx 0$ and $\Delta\dot{\mathbf{s}}_i/||\mathbf{u}^o - \mathbf{s}_i^o|| \approx 0$ for $i = 1, 2$. In other words, when the satellite location errors are negligible with respect to the source-satellite range, the proposed algorithm can attain the CRLB accuracy under Gaussian noise model.

The above analysis implicitly assumes that the matrix $\mathbf{D}$ is evaluated using the true source position. Similar assumption was also utilised in [96]–[98], [103], [108]. However, as pointed out in the previous subsection, the algorithm implementation uses the estimated source position instead to produce $\mathbf{D}$. The amount of error introduced is dependent on the TDOA and FDOA noise as well as satellite location errors. As a result, the estimation performance of the proposed technique would eventually deviate from CRLB when the noise level becomes sufficiently large and the thresholding effect [99] occurs.

5.4 Performance Validation and Evaluation

We study the performance of the proposed two-step source geolocation algorithm via simulations. The performance metrics used are the geolocation root mean square error (RMSE), $\text{RMSE}(\mathbf{u}) = \sqrt{\frac{1}{K}\sum_{k=1}^{K}\|\mathbf{u}_k - \mathbf{u}^o\|^2}$, and the estimation bias, $\text{Bias}(\mathbf{u}) = ||\frac{1}{K}\sum_{k=1}^{K}\mathbf{u}_k - \mathbf{u}^o||$. Here, $K = 20000$ is the number of Monte Carlo runs and $\mathbf{u}_k$ denotes the geolocation result in the k-th ensemble run.

The geolocation performance of the proposed algorithm is compared with the CRLB and that of two benchmark methods, namely an iterative ML estimator and a differential calibration (DC)-based estimator [94], [96]. The ML algorithm estimates the source latitude and longitude $\boldsymbol{\theta}^o$ together with the time and frequency offsets $\boldsymbol{\alpha}^o$ and true satellite locations $\boldsymbol{\beta}^o$. The estimate of the geocentric position of the source is then found by plugging the result into (5.1). We initialise the ML algorithm via adding to the true values zero-mean Gaussian noise with covariance matrix equal to $4{\cdot}\text{FIM}(\boldsymbol{\eta}^o)^{-1}$, where $\text{FIM}(\boldsymbol{\eta}^o)$ is given in (5.13). The DC-based method cancels $\boldsymbol{\alpha}^o$ by subtracting from the calibration measurements the source TDOA and FDOA and performing source geolocation using the transformed calibration measurements. Note that the satellite location errors are not explicitly taken into account in the DC-based method.

The simulated dual-satellite geolocation scenario is depicted in Figure 5.1. The source is located at [124^{o}E, 25^{o}N] with known altitude $h = 100$m. There are three ground calibration stations and they are located at [116.3^{o}E, 39.9^{o}N], [119^{o}E, 39^{o}N] and [121^{o}E, 31.5^{o}N]. Two satellites are located at [86.71^{o}E, 0.029^{o}S] and [86.78^{o}E, 0.042^{o}S] with altitudes 35792km and 35742km. They are moving with velocities $\dot{\mathbf{s}}_1^o = [3.76, -0.67, 126.5]^T$m/s and $\dot{\mathbf{s}}_2^o = [1.27, 0.15, 133.7]^T$m/s. This simulation scenario is challenging mainly because the baseline (i.e., the distance between two satellites) is around 72km, which is much smaller than the source-satellite distance of more than 37778km. Hence, is a short-baseline geolocation geometry.

The source carrier frequency is $f_c = 14.5$GHz. To simplify the simulation, the

carrier frequencies of the calibration stations are all set to be f_c as well, although in practice, they could be different from but close to f_c. The transponder at satellite 1 is assumed to have a group delay of 0.06μs and a local oscillator of 2.5GHz, both of which are unknown. We set that the covariance matrix for the source and calibration measurements $\mathbf{Q}_y$ is a diagonal matrix. Unless stated otherwise, the standard deviations of the TDOA and FDOA noises are $\sigma_t = 0.1\mu$s and $\sigma_f =$ 10mHz, while the standard deviations of the satellite position and velocity errors are $\sigma_s = 1000$m and $\sigma_{\dot{s}} = 0.01$m/s.

For the ML algorithm, each of the parameters is initialised by randomly drawing a sample from a normal distribution, of which the mean is the corresponding practical value and the variance equals to twice of the corresponding CRLB entry.

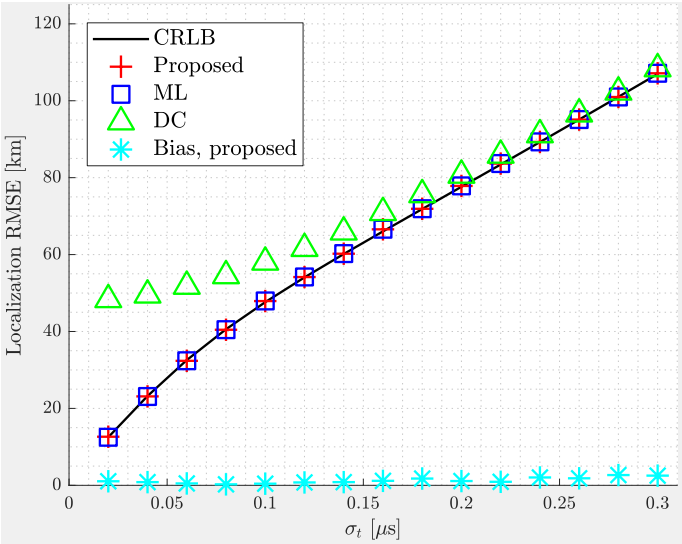

Figure 5.2: Geolocation RMSE as a function of the TDOA noise standard deviation σ_t.

Figure 5.2 plots as a function of the TDOA noise standard deviation σ_t the geolocation RMSE of the proposed two-step algorithm. It can be seen that the two-step method can provide geolocation accuracy very close to the CRLB when $\sigma_t \leq 0.25\mu$s, which is consistent with the performance analysis in subsection 5.3.2.

The ML estimator is also able to attain the CRLB accuracy. However, since time and frequency offsets are unknown, there is no ready explicit formulation to calculate the ML estimate. Instead, the ML estimates are obtained via iterative

numerical approximation, while the extra parameters are assessed in a joint manner. It is intuitive that the ML estimation is more computationally complex and time-consuming. According to simulation results, the proposed algorithm is at least 2 times faster than the ML method in terms of running time on our desktop with Intel Core i5-4590 3.30GHz CPU and 12GB RAM.

The DC-based technique, on the other hand, is unable to offer the CRLB performance under small TDOA noise, because it does not take into consideration the statistical information on the satellite location errors when performing measurement differencing. Note that as σ_t increases over 0.2μs, the performance of the DC-based approaches the CRLB. This is possibly because the TDOA noise now dominates the equivalent error covariance matrix $\hat{\mathbf{Q}}_y$ (5.30) and the effect of the satellite location errors is less influential Notice that the estimation bias of the proposed algorithm is always less than 3km, which is negligible compared with the geolocation RMSE. It indicates that the proposed algorithm is approximately unbiased in this simulation.

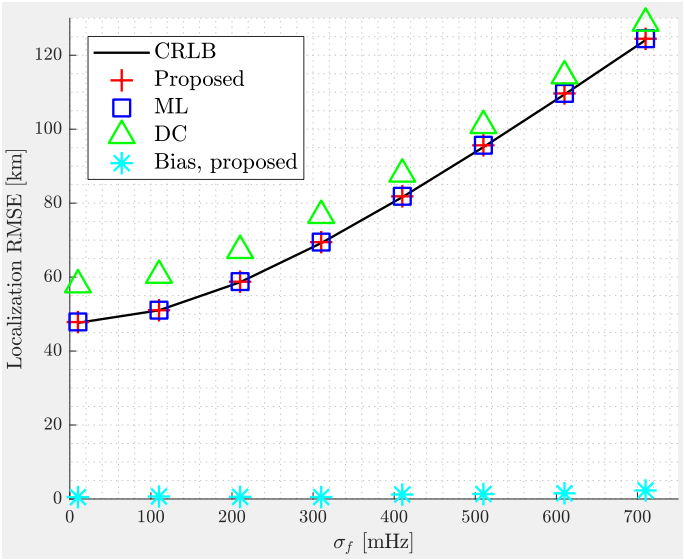

Figure 5.3: Geolocation RMSE as a function of the FDOA noise standard deviation σ_f.

Figure 5.3 shows the results as a function of the FDOA noise standard deviation σ_f. The obtained observations are similar to those from Figure 5.2. Again, as expected, the proposed two-step algorithm attains the CRLB accuracy.

Figure 5.4 compares the geolocation performance as a function of the satellite po-

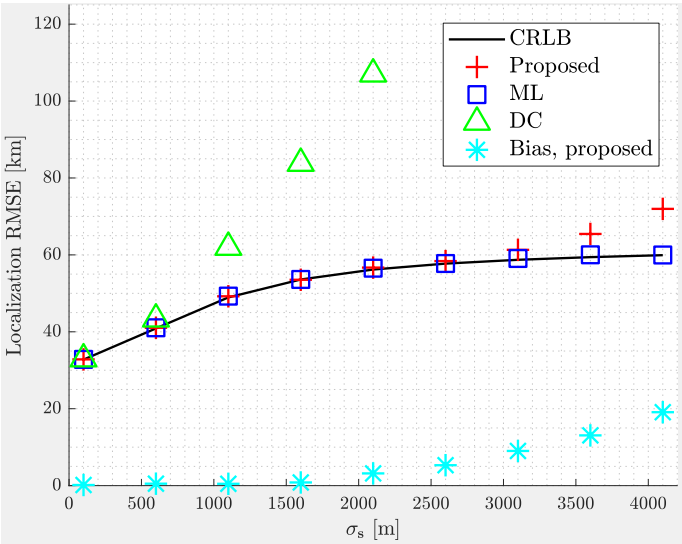

Figure 5.4: Geolocation RMSE as a function of the satellite position error standard deviation σ_s.

sition error standard deviation $\sigma_{\mathbf{s}}$. When $\sigma_{\mathbf{s}}$ is smaller than 2500m, the geolocation RMSEs of both the proposed two-step method and ML estimator remain very close to the CRLB. However, the performance of the proposed algorithm starts to deviate from the CRLB and become inferior to that of the ML estimator, as the satellite position error further increases. This is because the proposed algorithm does not refine the noisy satellite locations, in contrast to the ML estimator that estimates all the unknowns simultaneously.This is also the reason why the bias of the proposed algorithm increases apparently when $\sigma_{\mathbf{s}}$ is larger than 2500m. The geolocation performance of the DC-based method is very sensitive to the satellite position error and it degrades significantly as $\sigma_{\mathbf{s}}$ has larger values. We also investigated the geolocation performance as a function of the satellite velocity error standard deviation $\sigma_{\dot{s}}$. The observations are very similar and hence, the obtained results are omitted here.

Figure 5.5 demonstrates location CRLB and RMSE under different satellite velocity noise configuration. Similarly to Figure 5.4, both RMSEs of the proposed algorithm and the ML attain the CRLB when the satellite velocity standard deviation is less than 0.4m/s ($\sigma_{\dot{\mathbf{s}}} < 0.4$m/s). As larger satellite velocity error introduced, the proposed algorithm gives less location accuracy than the ML estimator. Noticing that the CRLB merely changes with variation of the velocity standard deviation.

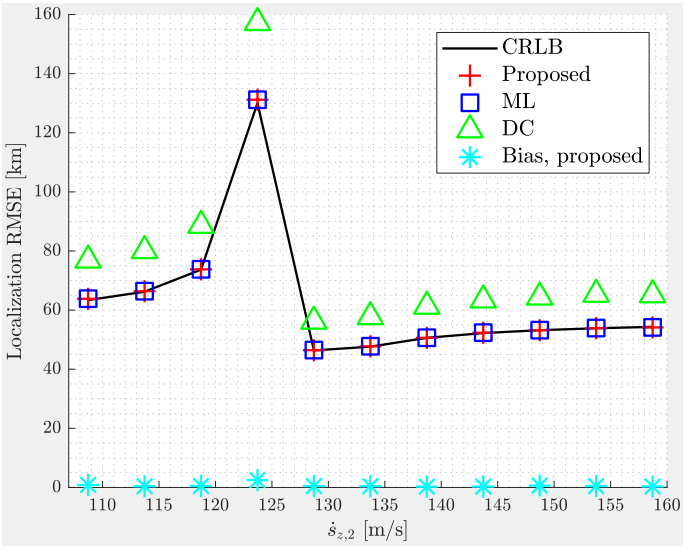

Figure 5.5: Geolocation RMSE as a function of the z-axis velocity of satellite 2.

It is because of that the effect of the velocity error on the source location CRLB is scaled by the partial derivative matrix $\frac{\partial \mathbf{y}^0}{\partial \boldsymbol{\beta}^o}$ as shown in (16). Through investigating practical value of $\frac{\partial \mathbf{y}^0}{\partial \boldsymbol{\beta}^o}$, we found that the submatrix corresponding to the satellite velocity error is of relatively small value.

Inspired by [115], Figure 5.5 illustrates the impact of different satellite velocity configurations on the geolocation performance of the three algorithms simulated. In particular, the velocity of satellite 2 is artificially varied using $\dot{\mathbf{s}}_2^o + k \cdot [0, 0, 5]^T$. It can be seen that the geolocation performance changes greatly under different satellite velocity configurations, mainly because they affect the amount of information provided by the FDOA measurements on the source position (5.3).

Figure 5.6 shows the geolocation performance as a function of the assumed source altitude. Specifically, the true source altitude is unknown (which is 100m) and practically some certain values of h are adopted in geolocation instead. As shown, the proposed algorithm and ML algorithm remain very close to the CRLB, while the DC-based produces obviously larger location errors. In a whole, the proposed algorithm, as well as the other two approaches, is insensitive to the error in the source altitude.

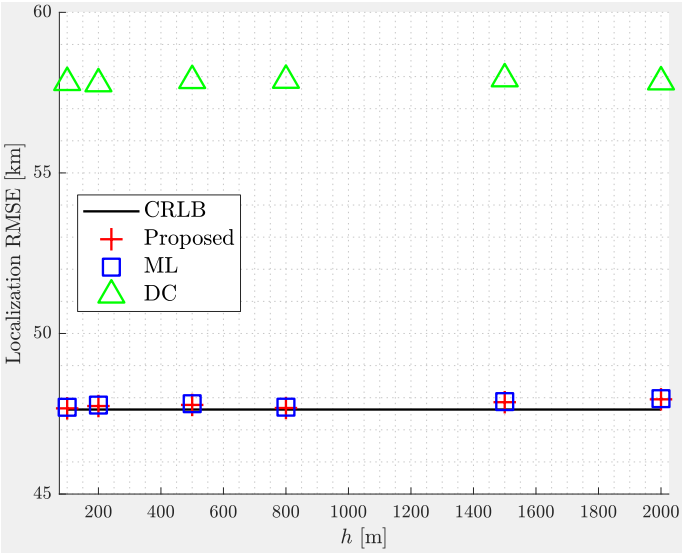

Figure 5.6: Geolocation RMSE as a function of the assumed source altitude.

5.5 Summary

We investigated the problem of dual-satellite source geolocation when time and frequency offsets between satellites and satellite location errors are present. The source position CRLB was derived. The insights from the CRLB analysis motivated the development of a closed-form two-step geolocation algorithm. In its Step-1 processing, the new method fuses using a BLUE the TDOAs and FDOAs from the source and calibration stations to produce as the output a single pair of source TDOA and FDOA. The time and frequency offsets are eliminated and the satellite location errors are taken into account in the weighting matrix of the BLUE. The second step of the proposed algorithm geolocates the source using the Step-1 output and the noisy satellite locations using an existing algebraic solution. Simulations using a short-baseline dual-satellite geolocation scenario verified the theoretical performance analysis result that the proposed algorithm can attain the CRLB performance under Gaussian noise and mild conditions.

In the future work, there is a plan to extend the proposed geolocation framework to the more general case with multiple satellites and satellite location refinement for further performance enhancement.

Chapter 6

Conclusion and Future Work

This thesis firstly investigated the existing wireless measurement types and corresponding positioning techniques. Then, three different scenarios where the localisation methods need to be applied with incomplete data have been studies. For each scenario, the thesis first analyses the shortcomings of current localisation methods and later proposes improved approaches. The proposed positioning methods are tested in simulations. The results are presented and evaluated.

- The first work investigates the RSS location fingerprinting techniques. Building a received signal strength (RSS) fingerprint database requires massive offline workload. Therefore, given a database of sparsely collected data points, spatial interpolation approaches, namely ordinary Kriging and universal Kriging , are applied to estimate RSS at unmeasured locations. A spatial model, namely variogram or residual variogram, is first developed to characterised measurement spatial correlations. Then, the RSS at a nearby unknown location can be estimated as a weighted sum of the RSS of known grid points, where the weights are calculated from the spatial model.

  The proposed approaches are validated by simulation and real-data experiments. Through analysing the results, it concludes that 1) the variogram models established on the sparsely collected data can effectively characterise the spatial correlation within the decorrelation range, 2) compared with the

inverse distance weighted interpolation, both ordinary Kriging and universal Kriging can produce RSS fingerprints of good quality, and the interpolation/estimate error decrease with the increase of density of known data points, 4) the recovered/interpolated fingerprint database can provide acceptable localisation qualities, and localisation accuracy increased with the density of known data points.

In the future work, firstly the proposed approaches can be tested with more real data. Secondly, there are literature considering the Kriging method belonging to Gaussian process. It is worth to investigate the similarities and differences between the Kriging method and Gaussian process method in the context of RSS based localisation.

- The second work investigated multi-target localisation in the Bayesian framework. For closely located targets, the radio signals propagate through similar paths that would result in correlations of shadowing effect. Taking advantage of shadowing correlation could improve the localisation performances. However, the shadowing effect changes very slowly, and for a short period there are usually not enough measurements to sufficiently characterise the shadowing correlation. To solve the problem, a Bayesian framework is proposed to calculate the posterior distribution of target location. To cope with the prior knowledge of shadowing correlation contained in a limited number of measurements, the inverse Wishart (IW) distribution is proposed and a close-form of the posterior is derived. To investigate how the IW scale matrix affects the posterior, different cases for scale matrix, including identity matrix, diagonal matrix and the true shadowing covariance, are tested in simulation.

  After obtaining the posterior, the first approach to estimate target locations is to utilise MCMC method (Metropolis-within-Gibbs sampler) to generate samples from the posterior and further yield the sample mean as location estimate. By analysing the simulation result, conclusions can be made: 1) the performance of MCMC sampler are influenced by several parameters in a complex

way and therefore are case-dependent, 2) the MCMC sampler clearly suffers from the local maximum of posterior especially for high-dimensional problems. As a result, the sample mean based location estimate is not generally liable.

As an alternative solution, the maximum a posterior (MAP) / maximum likelihood (ML) method is applied to produce location estimates. To validate this, a grid-based searching strategy and an MCMC based searching strategy are both tested in simulation. By studying the result, it concludes that: 1) the MAP/ML estimate can coincide with the weighted least square estimate which adopts the equivalent assumptions, 2) the MCMC based searching is sufficient to achieve the maximum of posterior/likelihood, the location estimates are of acceptable accuracy, 3) the consequence of different IW scale matrix assumption is not distinguishable for MAP/ML estimate.

In the future work, other guided searching strategies, such as gradient assisted searching, can be considered to find the global maximum of posterior/likelihood.

- The third work investigates the dual-satellite geolocation system. Given the location and velocity of the satellites, the time difference of arrival (TDOA) and frequency difference of arrival (FDOA) measurement are utilised to geolocate a ground target. There are unknown components, i.e. unknown time delay and frequency shift. To solve the problem, a new closed-form source geolocation algorithm is proposed using calibration stations at known positions. In particular, it first fuses the measurements from the unknown source and calibration stations using a best linear unbiased estimator (BLUE) [99]. The time and frequency offsets are eliminated in the fusion process and the presence of satellite location errors is appropriately taken into account in the weighting matrix. The measurement fusion step only produces a single pair of source TDOA and FDOA, which is then utilised by an existing algebraic technique for source geolocation. The developed algorithm has low computational complexity, and more importantly, theoretical performance analysis

shows that it can attain the Cramér-Rao lower bound (CRLB) under Gaussian noise and mild conditions.

Simulations using a short-baseline dual-satellite geolocation scenario verified the theoretical performance analysis result that the proposed algorithm can attain the CRLB performance under Gaussian noise and mild conditions.

In the future work, there is a plan to extend the proposed geolocation framework to the more general case with multiple satellites and satellite location refinement for further performance enhancement.

Appendices

Appendix A

Gradient Assisted Searching for MAP/ML Estimate

This section gives the derivatives of both the multivariate Gaussian likelihood and the inverse Wishart integrated likelihood w.r.t. the target location. Further algorithm based on the derivative, e.g., gradient based sampling method, can be developed.

A.1 Derivative of Multivariate Gaussian Likelihood

The multivariate Gaussian likelihood is given in (4.18). The derivative w.r.t. the target location, $\mathbf{s}$, can be derived as

$$\frac{\partial p(\mathbf{s} \mid \mathbf{z})}{\partial \mathbf{s}} = \frac{1}{\sqrt{(2\pi)^{mn}\,|\boldsymbol{\Sigma}_\varepsilon|}} \exp\left[-\frac{1}{2}\big(\mathbf{z}-\mathbf{f}\big)^{\mathsf{T}}\boldsymbol{\Sigma}_\varepsilon^{-1}\big(\mathbf{z}-\mathbf{f}\big)\right]\cdot\left(-\frac{1}{2}\right)\cdot\left(\frac{\partial}{\partial \mathbf{s}}\big(\mathbf{z}-\mathbf{f}\big)^{\mathsf{T}}\boldsymbol{\Sigma}_\varepsilon^{-1}\big(\mathbf{z}-\mathbf{f}\big)\right) \tag{A.1}$$

in which the derivative part is further given by

$$\frac{\partial}{\partial \mathbf{s}}\big(\mathbf{z}-\mathbf{f}\big)^{\mathsf{T}}\boldsymbol{\Sigma}_\varepsilon^{-1}\big(\mathbf{z}-\mathbf{f}\big) = -\big(\mathbf{z}-\mathbf{f}\big)^{\mathsf{T}}\big(\boldsymbol{\Sigma}_\varepsilon^{-1}+\boldsymbol{\Sigma}_\varepsilon^{-\mathsf{T}}\big)\frac{\partial \mathbf{f}}{\partial \mathbf{s}} \tag{A.2}$$

The derivative of shadowing-free RSS w.r.t. the target location is given by

$$\frac{\partial \mathbf{f}}{\partial \mathbf{s}} = \frac{\partial [\mathbf{f}_1^\mathsf{T} \dots \mathbf{f}_m^\mathsf{T}]^\mathsf{T}}{\partial [\mathbf{s}_1^\mathsf{T} \dots \mathbf{s}_m^\mathsf{T}]^\mathsf{T}} = \begin{bmatrix} \frac{\partial \mathbf{f}_1}{\partial \mathbf{s}_1} & & \\ & \ddots & \\ & & \frac{\partial \mathbf{f}_m}{\partial \mathbf{s}_m} \end{bmatrix} \tag{A.3}$$

where

$$\frac{\partial \mathbf{f}_i}{\partial \mathbf{s}_i} = \begin{bmatrix} \frac{\partial \mathbf{f}_i}{\partial x_{s,i}} & \frac{\partial \mathbf{f}_i}{\partial y_{s,i}} \end{bmatrix} = \begin{bmatrix} \frac{\partial f_{i,1}}{\partial x_{s,i}} & \frac{\partial f_{i,1}}{\partial y_{s,i}} \\ \vdots & \vdots \\ \frac{\partial f_{i,n}}{\partial x_{s,i}} & \frac{\partial f_{i,n}}{\partial y_{s,i}} \end{bmatrix} \tag{A.4}$$

and

$$\frac{\partial f_{i,j}}{\partial x_{s,i}} = \frac{10\alpha}{\ln 10} \cdot \frac{x_{s,i} - x_{b,j}}{d_{i,j}^2} \tag{A.5a}$$

$$\frac{\partial f_{i,j}}{\partial y_{s,i}} = \frac{10\alpha}{\ln 10} \cdot \frac{y_{s,i} - y_{b,j}}{d_{i,j}^2} \tag{A.5b}$$

A.2 Derivative of Inverse Wishart Integrated Likelihood

The inverse Wishart integrated likelihood is given in (4.23). The derivative w.r.t. the target location can be derived as

$$\frac{\partial p(\mathbf{s} \mid \mathbf{z})}{\partial \mathbf{s}} = \frac{1}{(2\pi)^{\frac{mn}{2}}} \cdot \frac{|\mathbf{\Psi}|^{\frac{v}{2}}}{2^{\frac{v \cdot mn}{2}} \Gamma_{mn}(\frac{v}{2})} \cdot 2^{\frac{(1+v)mn}{2}} \Gamma_{mn}(\frac{1+v}{2}) \cdot \left(\frac{\partial}{\partial \mathbf{s}} |\mathbf{\Phi} + \mathbf{\Psi}|^{-\frac{1+v}{2}} \right) \tag{A.6}$$

Noticing that the derivative of a matrix w.r.t. a vector should be considered specifically in the aspect of layout. The original derivative is taken of a scalar (determinant of a matrix) over a column vector, therefore the result should be a row vector, that is

$$\frac{\partial}{\partial \mathbf{s}} |\mathbf{\Phi} + \mathbf{\Psi}|^{-\frac{1+v}{2}} = \begin{bmatrix} \frac{\partial}{\partial \mathbf{s}_1} |\mathbf{\Phi} + \mathbf{\Psi}|^{-\frac{1+v}{2}} & \cdots & \frac{\partial}{\partial \mathbf{s}_2} |\mathbf{\Phi} + \mathbf{\Psi}|^{-\frac{1+v}{2}} \end{bmatrix} \tag{A.7}$$

in which each element should be a 1×2 row vector consist of scalars, i.e.

$$\frac{\partial}{\partial \mathbf{s}_i} \left|\mathbf{\Phi}+\mathbf{\Psi}\right|^{-\frac{1+v}{2}} = \left[\frac{\partial}{\partial x_{s,i}} \left|\mathbf{\Phi}+\mathbf{\Psi}\right|^{-\frac{1+v}{2}} \quad \frac{\partial}{\partial y_{s,i}} \left|\mathbf{\Phi}+\mathbf{\Psi}\right|^{-\frac{1+v}{2}}\right] \tag{A.8}$$

The derivative of square-error matrix w.r.t. $x_{s,i}$ is further given by

$$\frac{\partial}{\partial x_{s,i}} \left|\mathbf{\Phi}+\mathbf{\Psi}\right|^{-\frac{1+v}{2}} = -\frac{1+v}{2} \cdot \left|\mathbf{\Phi}+\mathbf{\Psi}\right|^{-\frac{1+v}{2}} \cdot \mathrm{tr}\left((\mathbf{\Phi}+\mathbf{\Psi})^{-1}\frac{\partial \mathbf{\Phi}}{\partial x_{s,i}}\right) \tag{A.9}$$

where

$$\frac{\partial \mathbf{\Phi}}{\partial x_{s,i}} = \frac{\partial}{\partial x_{s,i}}\big(\mathbf{z}-\mathbf{f}\big)\big(\mathbf{z}-\mathbf{f}\big)^{\mathsf{T}} \tag{A.10a}$$

$$= \frac{\partial}{\partial x_{s,i}} \begin{bmatrix} (\mathbf{z}_1-\mathbf{f}_1)(\mathbf{z}_1-\mathbf{f}_1)^{\mathsf{T}} & (\mathbf{z}_1-\mathbf{f}_1)(\mathbf{z}_2-\mathbf{f}_2)^{\mathsf{T}} & \cdots & (\mathbf{z}_1-\mathbf{f}_1)(\mathbf{z}_m-\mathbf{f}_m)^{\mathsf{T}} \\ (\mathbf{z}_2-\mathbf{f}_2)(\mathbf{z}_1-\mathbf{f}_1)^{\mathsf{T}} & (\mathbf{z}_2-\mathbf{f}_2)(\mathbf{z}_2-\mathbf{f}_2)^{\mathsf{T}} & \cdots & (\mathbf{z}_2-\mathbf{f}_2)(\mathbf{z}_m-\mathbf{f}_m)^{\mathsf{T}} \\ \vdots & \vdots & \ddots & \vdots \\ (\mathbf{z}_m-\mathbf{f}_m)(\mathbf{z}_1-\mathbf{f}_1)^{\mathsf{T}} & (\mathbf{z}_m-\mathbf{f}_m)(\mathbf{z}_2-\mathbf{f}_2)^{\mathsf{T}} & \cdots & (\mathbf{z}_m-\mathbf{f}_m)(\mathbf{z}_m-\mathbf{f}_m)^{\mathsf{T}} \end{bmatrix} \tag{A.10b}$$

and

$$\frac{\partial}{\partial x_{s,i}}\big(\mathbf{z}_k-\mathbf{f}_k\big)\big(\mathbf{z}_l-\mathbf{f}_l\big)^{\mathsf{T}} = \begin{cases} \mathbf{0}_{n\times n}, & \text{if } k \neq i \text{ and } l \neq i \\ -\left((\mathbf{z}_l-\mathbf{f}_l)\cdot\dfrac{\partial \mathbf{f}_i}{\partial x_{s,i}}\right)^{\mathsf{T}}, & \text{if } k = i \text{ and } l \neq i \\ -(\mathbf{z}_k-\mathbf{f}_k)\cdot\dfrac{\partial \mathbf{f}_i}{\partial x_{s,i}}, & \text{if } k \neq i \text{ and } l = i \\ -\left((\mathbf{z}_i-\mathbf{f}_i)\cdot\dfrac{\partial \mathbf{f}_i}{\partial x_{s,i}}\right)^{\mathsf{T}} - (\mathbf{z}_i-\mathbf{f}_i)\cdot\dfrac{\partial \mathbf{f}_i}{\partial x_{s,i}}, & \text{if } k = i \text{ and } l = i \end{cases} \tag{A.11}$$

where the derivative of shadowing-free RSS w.r.t. the $x_{s,i}$ can be summarised from (A.4) and (A.5). The derivative of square-error matrix w.r.t. $y_{s,i}$ is similar to (A.9), (A.10b) and (A.11).

Appendix B

Complementary Derivative for Dual-Satellite TDOA-FDOA Geolocation

Expressions for the partial derivatives $\left(\frac{\partial \mathbf{u}^o}{\partial \boldsymbol{\theta}^o}\right)$, $\left(\frac{\partial \mathbf{d}_u^o}{\partial \boldsymbol{\theta}^o}\right)$ and $\left(\frac{\partial \mathbf{y}^o}{\partial \boldsymbol{\beta}^o}\right)$ are provided here to complete the derivation of the source geolocation CRLB in (5.23).

From the definition $\boldsymbol{\theta}^o = [\phi, \varphi]^T$, the partial derivative $\left(\frac{\partial \mathbf{u}^o}{\partial \boldsymbol{\theta}^o}\right)$ can be easily shown to be equal to

$$\left(\frac{\partial \mathbf{u}^o}{\partial \boldsymbol{\theta}^o}\right) = \left[\left(\frac{\partial \mathbf{u}^o}{\partial \phi}\right), \left(\frac{\partial \mathbf{u}^o}{\partial \varphi}\right)\right]. \tag{B.1}$$

The detailed expression can be easily found using (5.1) and will be omitted here.

In the following derivation, we need the following definitions. Specifically, $\boldsymbol{\rho}_{\mathbf{a},\mathbf{b}} = \frac{(\mathbf{a}-\mathbf{b})}{||\mathbf{a}-\mathbf{b}||}$ denotes a unit vector from $\mathbf{b}$ to $\mathbf{a}$ and $\mathbf{g}_{\mathbf{a},\mathbf{b}} = -\frac{\dot{\mathbf{b}}}{||\mathbf{a}-\mathbf{b}||} + \frac{(\mathbf{a}-\mathbf{b})^T\dot{\mathbf{b}}}{||\mathbf{a}-\mathbf{b}||^2}\boldsymbol{\rho}_{\mathbf{a},\mathbf{b}}$.

By Chain Rule, $\left(\frac{\partial \mathbf{d}_u^o}{\partial \boldsymbol{\theta}^o}\right)$ can be expressed as

$$\left(\frac{\partial \mathbf{d}_u^o}{\partial \boldsymbol{\theta}^o}\right) = \left(\frac{\partial \mathbf{d}_u^o}{\partial \mathbf{u}^o}\right)\left(\frac{\partial \mathbf{u}^o}{\partial \boldsymbol{\theta}^o}\right) \tag{B.2}$$

where $\left(\frac{\partial \mathbf{u}^o}{\partial \boldsymbol{\theta}^o}\right)$ is given in (B.1) and $\left(\frac{\partial \mathbf{d}_u^o}{\partial \mathbf{u}^o}\right)$ is equal to, from (5.3),

$$\left(\frac{\partial \mathbf{d}_u^o}{\partial \mathbf{u}^o}\right) = \begin{bmatrix} \boldsymbol{\rho}^T_{\mathbf{u}^o,\mathbf{s}_1^o} - \boldsymbol{\rho}^T_{\mathbf{u}^o,\mathbf{s}_2^o} \\ \mathbf{g}^T_{\mathbf{u}^o,\mathbf{s}_1^o} - \mathbf{g}^T_{\mathbf{u}^o,\mathbf{s}_2^o} \end{bmatrix}. \tag{B.3}$$

Using (5.8), we have that

$$\left(\frac{\partial \mathbf{y}^o}{\partial \boldsymbol{\beta}^o}\right) = \left[\left(\frac{\partial \mathbf{d}_u^o}{\partial \boldsymbol{\beta}^o}\right)^T, \left(\frac{\partial \mathbf{d}_{c,1}^o}{\partial \boldsymbol{\beta}^o}\right)^T, ..., \left(\frac{\partial \mathbf{d}_{c,N}^o}{\partial \boldsymbol{\beta}^o}\right)^T\right]^T. \tag{B.4}$$

From (5.3) and (5.7), it can be shown that

$$\left(\frac{\partial \mathbf{d}_u^o}{\partial \boldsymbol{\beta}^o}\right) = \begin{bmatrix} -\boldsymbol{\rho}^T_{\mathbf{u}^o,\mathbf{s}_1^o} & \mathbf{0}^T & \boldsymbol{\rho}^T_{\mathbf{u}^o,\mathbf{s}_2^o} & \mathbf{0}^T \\ -\mathbf{g}^T_{\mathbf{u}^o,\mathbf{s}_1^o} & -\boldsymbol{\rho}^T_{\mathbf{u}^o,\mathbf{s}_1^o} & \mathbf{g}^T_{\mathbf{u}^o,\mathbf{s}_2^o} & \boldsymbol{\rho}^T_{\mathbf{u}^o,\mathbf{s}_2^o} \end{bmatrix} \tag{B.5a}$$

$$\left(\frac{\partial \mathbf{d}_{c,n}^o}{\partial \boldsymbol{\beta}^o}\right) = \begin{bmatrix} -\boldsymbol{\rho}^T_{\mathbf{c}_n,\mathbf{s}_1^o} & \mathbf{0}^T & \boldsymbol{\rho}^T_{\mathbf{c}_n,\mathbf{s}_2^o} & \mathbf{0}^T \\ -\mathbf{g}^T_{\mathbf{c}_n,\mathbf{s}_1^o} & -\boldsymbol{\rho}^T_{\mathbf{c}_n,\mathbf{s}_1^o} & \mathbf{g}^T_{\mathbf{c}_n,\mathbf{s}_2^o} & \boldsymbol{\rho}^T_{\mathbf{c}_n,\mathbf{s}_2^o} \end{bmatrix} \tag{B.5b}$$

where $n = 1, 2, ..., N$. This completes the derivation of the partial derivatives required in the CRLB result in Section III.

Bibliography

[1] C. Liu, A. Kiring, N. Salman, L. Mihaylova, and I. Esnaola, "A kriging algorithm for location fingerprinting based on received signal strength", in *Proceedings of 2015 Workshop on Sensor Data Fusion (SDF 2015)*, 2015.

[2] C. Liu, L. Yang, and L. Mihaylova, "Dual-satellite source geolocation with time and frequency offsets and satellite location errors", in *Proceedings of 20th International Conference on Information Fusion (FUSION 2017)*, 2017. (**ISIF 2017 Tammy Blair Best Student Paper Award**).

[3] Y. Zhao, C. Liu, L. S. Mihaylova, and F. Gunnarsson, "Gaussian process for rss fingerprints construction in indoor localization", in *21st International Conference on Information Fusion (FUSION 2018)*, 2018.

[4] A. Kiring, N. Salman, C. Liu, I. Esnaola, and L. Mihaylova, "A shrinkage-based particle filter for tracking with correlated measurements", in *Proceedings of 2015 Workshop on Sensor Data Fusion (SDF 2015)*, 2015.

[5] A. Kiring, N. Salman, C. Liu, I. Esnaola, and L. Mihaylova, "Tracking with sparse and correlated measurements via a shrinkage-based particle filter", vol. 17, no. 10, pp. 3152–3164, 10 2017.

[6] N. R. Kumar and E. Nagabhooshanam, "An extended kalman filter for low-cost positioning system in agricultural vehicles", in *Proceedings of 2016 International Conference on Wireless Communications, Signal Processing and Networking (WiSPNET)*, Chennai, India, 2016, pp. 151–157.

[7] Y. Dobrev, M. Vossiek, M. Christmann, I. Bilous, and P. Gulden, "Steady delivery: Wireless local positioning systems for tracking and autonomous navigation of transport vehicles and mobile robots", *IEEE Microwave Magazine*, vol. 18, no. 6, pp. 26–37, 2017.

[8] I. Dobson, Q. Doan, and G. Hung, "A systematic review of patient tracking systems for use in the pediatric emergency department", *The Journal of emergency medicine*, vol. 44, no. 1, pp. 242–248, 2013.

[9] X. Li, X. Zhang, X. Ren, M. Fritsche, J. Wickert, and H. Schuh, "Precise positioning with current mult-constellation global navigation satellites systems: Gps, glonass, galileo and beidou", *Scientific Reports*, vol. 5, no. 8328, 2015.

[10] V. Honkavirta, T. Perälä, S. Ali-löytty, and R. Piché, "A comparative survey of wlan location fingerprinting methods", in *Proceddings of 6th Workshop on Positioning, Navigation and Vommunication 2009 (WPNC'09)*, Hannover, Germany, 2009, pp. 243–251.

[11] F. Gustafsson and F. Gunnarsson, "Mobile positioning using wireless networks: Possibilities and fundamental limitations based on available wireless network measurements", vol. 22, no. 4, pp. 41–53, 4 2005.

[12] N. Patwari, J. N. Ash, S. Kyperountas, A. O. Hero, R. L. Moses, and N. S. Correal, "Locating the nodes: Cooperative localization in wireless sensor networks", vol. 22, no. 4, pp. 54–69, 2005.

[13] G. Han, J. Jiang, C. Zhang, T. Q. Duong, M. Guizani, and G. K. Karagiannidis, "A survey on mobile anchor node assisted localization in wireless sensor networks", *IEEE Communications Surveys Tutorials*, vol. 18, no. 3, pp. 2220–2243, 2016.

[14] H. Liu, H. Darabi, P. Banerjee, and J. Liu, "Survey of wireless indoor positioning techniques and systems", *IEEE Transactions on Systems, Man, and Cybernetics, Part C (Applications and Reviews)*, vol. 37, no. 6, pp. 1067–1080, 6 2007.

[15] M. Bouet and A. L. dos Santos, "Rfid tags: Positioning principles and localization techniques", in *Proceedings of 2008 1st IFIP Wireless Days*, Dubai, United Arab Emirates, 2008, pp. 1–5.

[16] T. Sanpechuda and L. Kovavisaruch, "A review of rfid localization: Applications and techniques", in *Proceedings of 5th International Conference on Electrical Engineering/Electronics, Computer, Telecommunications and Information Technology*, vol. 2, Krabi, Thailand, 2008, pp. 769–772.

[17] B. D. Van Veen and K. M. Buckley, *Beamforming: A versatile approach to spatial filtering*, 1988.

[18] B. Ottersten, M. Viberg, P. Stoica, and A. Nehorai, "Exact and large sample maximum likelihood techniques for parameter estimation and detection in array processing", in *Radar Array Processing*, 1993, pp. 99–151.

[19] D. Niculescu and B. Nath, "Ad hoc positioning system (aps) using aoa", in *Proceedings of 22nd Annual Joint Conference of the IEEE Computer and Communications Societies (IEEE INFOCOM 2003)*, vol. 3, San Francisco, CA, USA, 2003, pp. 1734–1743.

[20] İ. Güvenç and C. C. Chong, "A survey on toa based wireless localization and nlos mitigation techniques", *IEEE Communications Surveys & Tutorials*, vol. 11, no. 3, pp. 107–124, 2009.

[21] Z. Ma and K. C. Ho, "Toa localization in the presence of random sensor position errors", in *Proceedings of 2011 IEEE International Conference on Acoustics, Speech and Signal Processing (ICASSP)*, Prague, Czech Republic, 2011.

[22] M. Vossiek, L. Wiebking, P. Gulden, J. Wieghardt, C. Hoffmann, and P. Heide, "Wireless local positioning", *IEEE Microwave Magazine*, vol. 4, no. 4, pp. 77–86, 2003.

[23] D. Li and Y. Hu, "Energy-based collaborative source localization using acoustic microsensor array", *EURASIP Journal on Applied Signal Processing*, vol. 2003, no. 4, pp. 321–337, 2003.

[24] Q. Shi and C. He, "A new incremental optimization algorithm for ml-based source localization in sensor networks", vol. 15, pp. 45–48, 2008.

[25] D. Blatt and A. O. Hero, "Energy-based sensor network source localization via projection onto convex sets", vol. 54, no. 9, pp. 3614–3619, 2006.

[26] X. Sheng and Y. Hu, "Maximum likelihood multiple-source localization using acoustic energy measurements with wireless sensor networks", vol. 53, no. 1, pp. 44–53, 2005.

[27] N. Patwari, A. O. Hero, M. Perkins, N. S. Correal, and R. J. O'Dea, "Relative location estimation in wireless sensor networks", vol. 51, no. 8, pp. 2137–2148, 2003.

[28] J. B. Andersen, T. S. Rappaport, and S. Yoshida, "Propagation measurements and models for wireless communications channels", vol. 33, no. 1, pp. 42–49, 1995.

[29] P. Bahl and V. N. Padmanabhan, "Radar: An in-building rf-based user location and tracking system", in *Proceedings of 19th Annual Joint Conference of the IEEE Computer and Communications Societies (INFOCOM 2000)*, vol. 2, Tel Aviv, Israel, 2000, pp. 775–784.

[30] M. B. Kjærgaard, "Indoor positioning with radio location fingerprinting", PhD thesis, Department of Computer Science, University of Aarhus, Denmark, 2010.

[31] Y. Zhao, F. Yin, F. Gunnarsson, M. Amirijoo, and G. Hendeby, "Gaussian process for propagation modelling and proximity reports based indoor posioning", in *Proceedings of 2016 IEEE 83rd Vehicular Technology Conference (VTC Spring)*, Nanjing, China, 2016.

[32] K. Kaemarungsi and P. Krishnamurthy, "Properties of indoor received signal strength for wlan location fingerprinting", in *The First Annual International Conference on Mobile and Ubiquitous Systems: Networking and Services*, Boston, MA, USA, 2004, pp. 14–23.

[33] P. Prasithsangaree, P. Krishnamurthy, and P. Chrysanthis, "On indoor position location with wireless lans", in *Proceedings of 13th IEEE International Symposium on Personal, Indoor and Mobile Radio Communications*, vol. 2, Lisboa, Portugal, 2002, pp. 720–72.

[34] W. M. Yeung, J. Zhou, and J. K. Ng, "Enhanced fingerprint-based location estimation system in wireless lan enviroment", in *Emerging Directions in Embedded and Ubiquitous Computing (EUC 2007)*. 2007, pp. 273–284.

[35] J. Talvitie, M. Renfors, and E. S. Lohan, "Distance-based interpolation and extrapolation methods for rss-based localization with indoor wireless signals", vol. 64, no. 4, pp. 1340–1353, 2015.

[36] T. Roos, P. Myllymäki, H. Tirri, P. Misikangas, and J. Sievänen, "A probabilistic approach to wlan user location estimation", *International Journal of Wireless Information Networks*, vol. 9, no. 3, pp. 155–164, Feb. 2002.

[37] M. A. Youssef, A. Agrawala, and A. U. Shankar, "Wlan location determination via clustring and probability distributions", in *Proceedings of the First IEEE International Conference on Pervasive Computing and Communications*, Fort Worth, TX, USA, Mar. 2003, pp. 143–150.

[38] T. N. Lin and P. C. Lin, "Performance comparison of indoor positioning techniques based on location fingerprinting in wireless networks", in *Proceedings of International Conference on Wireless Networks, Communications and Mobile Computing*, 2 vols., Maui, HI, USA, Jun. 2005, pp. 1569–1574.

[39] Y. Ji, S. Biaz, S. Pandey, and P. Agrawal, "Ariadne: A dynamic indoor signal map construction and localization system", in *Proceedings of 4th Interna-*

tional Conference on Mobile Systems, Applications and Services, Uppsala, Sweden, 2006, pp. 151–164.

[40] R. Kubota, S. Tagashira, Y. Arakawa, T. Kitasuka, and A. Fukuda, "Efficient survey database construction using location fingerprinting interpolation", in *Proceedings of 2013 IEEE 27th International Conference on Advanced Information Networking and Applications (AINA)*, Barcelona, Spain, 2013, pp. 469–476.

[41] K. Arai and H. Tolle, "Color radiomap interpolation for efficient fingerprint wifi-based indoor location estimation", *International Journal of Advanced Research in Artificial Intelligence*, vol. 2, no. 3, pp. 10–15, 2013.

[42] W. Bong and Y. Kim, "Fingerprint wi-fi radio map interpolated by discontinuity preserving smoothing", in *Convergence and Hybrid Information Technology: 6th International Conference (ICHIT 2012)*. 2012, pp. 138–145.

[43] M. Gudmundson, "Correlation model for shadow fading in mobile radio systems", *Electron. Lett.*, vol. 27, no. 23, pp. 2145–2146, 1991.

[44] S. R. Saunders and A. A. Zavala, *Antenna and Propagation for Wireless Communication Systems*. Wiley, 2007.

[45] S. S. Szyszkowicz, H. Yanikomeroglu, and J. S. Thompson, "On the feasibility of wireless shadowing correlation models", *IEEE Transaction on Vehicular Technology*, vol. 59, no. 9, pp. 4222–4236, 2010.

[46] T. Klingenbrunn and P. Mogensen, "Modelling cross-correlated shadowing in network simulations", in *Proceedings of IEEE 50th Vehicular Technology Conference*, 3 vols., Amsterdam, The Netherlands, 1999, pp. 1407–1411.

[47] V. Graziano, "Propagation correlations at 900 mhz", vol. 27, no. 4, pp. 182–189, 1978.

[48] T. B. Sørensen, "Slow fading cross-correlation against azimuth separation of base stations", *Electron. Lett.*, vol. 35, no. 2, pp. 127–129, 1999.

[49] K. S. Butterworth, K. W. Sowerby, and A. G. Williamson, "Correlated shadowing in an in-building propagation environment", *Electron. Lett.*, vol. 33, no. 2, pp. 420–422, 1997.

[50] R. K. Sharma and J. W. Wallace, "Indoor shadowing correlation measurements for cognitive radio studies", in *Proceedings of 2009 IEEE Antennas and Propagation Society International Symposium*, Charleston, SC, USA, 2009, pp. 4–7.

[51] F. Graziosi and F. Santucci, "A general correlation model for shadow fading in mobile radio systems", vol. 6, no. 3, pp. 102–104, 2002.

[52] M. A. Oliver and R. Webster, "A tutorial guide to geostatistics: Computing and modelling variograms and kriging", *CATENA*, vol. 113, no. Supplement C, pp. 56–69, 2014.

[53] E. H. Isaaks and R. M. Srivastava, *Applied Geostatistics*. Oxford University Press, 1989.

[54] J. P. Chilès and P. Delfiner, *Geostatistics: Modeling Spatial Uncertainty*. Wiley, 1999, ch. 3, pp. 150–224.

[55] G. Matheron, "Principles of geostatistics", *Econ. Geol.*, vol. 58, no. 8, pp. 1246–1266, 1963.

[56] N. Cressie, *Statistics for Spatial Data*. John Wiley, 1993.

[57] G. C. Bohling, *Introduction to geostatistics and variogram analysis*. [Online]. Available: `http://people.ku.edu/~gbohling/cpe940/Variograms.pdf` (visited on Apr. 7, 2015).

[58] N. Cressie, "Fitting variogram models by weighted least squares", *Math. Geol.*, vol. 17, no. 5, pp. 563–586, 1985.

[59] G. C. Bohling, *Kriging*. [Online]. Available: `http://people.ku.edu/~gbohling/cpe940/Kriging.pdf` (visited on Apr. 7, 2015).

[60] B. Zhou, Q. Chen, H. Wymeersch, P. Xiao, and L. Zhao, "Variational inference-based positioning with nondeterministic measurement accuracies and reference location errors", vol. 16, no. 10, pp. 2955–2969, 2017.

[61] N. Salman, M. Ghogho, and A. H. Kemp, "On the joint estimation of the rss-based location and path-loss exponent", vol. 1, no. 1, pp. 34–37, 2012.

[62] N. Salman, A. H. Kemp, and M. Ghogho, "Low complexity joint estimation of location and path-loss exponent", vol. 1, no. 4, pp. 364–367, 2012.

[63] A. Bel, J. L. Vicario, and G. Seco-Granados, "Localization algorithm with on-line path loss estimation and node selection", *Sensors*, vol. 11, no. 7, pp. 6905–6925, 2011.

[64] H. Wymeersch, J. Lien, and M. Z. Win, "Cooperative localization in wireless networks", vol. 97, no. 2, pp. 427–450, 2009.

[65] R. W. Ouyang, A. K.-S. Wong, and C.-T. Lea, "Received signal strength-based wireless localization via semidefinite programming: Noncooperative and cooperative schemes", vol. 59, no. 3, pp. 1307–1318, 2010.

[66] L. S. Muppirisetty, T. Svensson, and H. Wymeersch, "Spatial wireless channel prediction under location uncertainty", vol. 15, no. 2, pp. 1031–1044, 2016.

[67] F. Yin and F. Gunnarsson, "Distributed recursive gaussian processes for rss map applied to target tracking", vol. 11, no. 3, pp. 492–503, 2017.

[68] K. Liu, Z. Meng, and C.-M. Own, "Gaussian process regression plus method for localization reliability improvement", *Sensors*, vol. 16, no. 8, pp. 1193–1210, 2016.

[69] N. Patwari and P. Agrawal, "Nesh: A joint shadowing model for links in a multi-hop network", in *Proceedings of 2008 IEEE International Conference on Acoustics, Speech and Signal Processing*, 2008, pp. 2873–2876.

[70] N. Salman, L. Mihaylova, and A. H. Kemp, "Localization of multiple nodes based on correlated measurements and shrinkage estimation", in *Proceedings of 2014 Sensor Data Fusion: Trends, Solutions, Applications (SDF)*, Bonn, Germany, 2014.

[71] A. K. Gupta and D. K. Nagar, *Matrix Variate Distributions*. Chapman & Hall, 1999.

[72] K. Yu, *A note on inverted wishart distribution*. [Online]. Available: `https://pdfs.semanticscholar.org/bcbc/d6e63bc9c2f231490513bd1c1414f05b606e.pdf` (visited on Oct. 10, 2016).

[73] J. W. Koch, "Bayesian approach to extended object and cluster tracking using random matrices", vol. 44, no. 3, 1042?1059, 2008.

[74] K. Granström, M. Baum, and S. Reuter, "Extended object tracking: Introduction, overview and applications", *ISIF Journal of Advances in Information Fusion*, vol. 12, no. 2, 2017.

[75] S. W. Nydick, *The wishart and inverse wishart distributions*. [Online]. Available: `https://pdfs.semanticscholar.org/ac51/ee74af59c432d493da98bd950cc6f856a0ca.pdf` (visited on Sep. 8, 2016).

[76] G. Casella and E. I. George, "Explaining the gibbs sampler", *The American Statistician*, vol. 46, no. 3, pp. 167–174, 1992.

[77] C. Andrieu, N. De Freitas, A. Doucet, and M. I. Jordan, "An introduction to mcmc for machine learning", *Machine Learning*, vol. 50, no. 1-2, pp. 5–43, 2003.

[78] T. S. Rappaport, *Wireless Communications: Principles and Practice*. Prentice Hall PTR, 2002.

[79] K. B. Petersen and M. S. Pedersen, "The matrix cookbook", Tech. Rep., 2012. [Online]. Available: `http://www2.imm.dtu.dk/pubdb/p.php?3274`.

[80] K. Radnosrati, F. Gunnarsson, and F. Gustafsson, "New trends in radio network positioning", in *Proc. International Conference on Information Fusion (FUSION)*, 2015, pp. 492–498.

[81] K. Radnosrati, C. Fritsche, G. Hendeby, F. Gunnarsson, and F. Gustafsson, "Fusion of TOF and TDOA for 3GPP positioning", in *Proc. International Conference on Information Fusion (FUSION)*, 2016.

[82] K. C. Ho and Y. T. Chan, "Geolocation of a known altitude object from TDOA and FDOA measurements", *IEEE Transactions on Aerospace and Electronic Systems*, vol. 33, pp. 770–783, Jul. 1997.

[83] M. Sun and K. C. Ho, "Refining inaccurate sensor positions using target at unknown location", *Signal Processing*, vol. 92, pp. 2097–2104, Sep. 2012.

[84] J. Geeraert, J. W. McMahon, and B. A. Jones, "Orbit determination observability of the dual-satellite geolocation system with TDOA and FDOA", in *Proc. AIAA/AAS Astrodynamics Specialist Conference*, 2016, pp. 5367–5388.

[85] D. P. Haworth, N. G. Smith, R. Bardelli, and T. Clement, "Interference localization for EUTELSAT satellites-the first European transmitter location system", *International Journal of Satellite Communications and Networking*, vol. 15, pp. 155–183, Jul. 1997.

[86] M. H. Chan, "Application of a dual satellite geolocation system on locating sweeping interference", *World Academy of Science, Engineering and Technology*, vol. 6, pp. 939–944, Sep. 2012.

[87] F. Guo, Y. Fan, Y. Zhou, C. Zhou, and Q. Li, *Space Electronic Reconnaissance: Localization Theories and Methods*. Hoboken, NJ, USA: Wiley, 2014.

[88] S. Stein, "Algorithms for ambiguity function processing", *IEEE Transactions on Acoustics, Speech, and Signal Processing*, vol. 29, pp. 588–599, Jun. 1981.

[89] C. L. Yatrakis, "Computing the cross ambiguity function - a review", Master's thesis, Binghamton University, State University of New York, 2005.

[90] J. Overfield, Z. Biskaduros, and R. M. Buehrer, "Geolocation of MIMO signals using cross ambiguity function and TDOA/FDOA", in *Proc. IEEE International Conference on Communications (ICC)*, 2012, pp. 3648–3653.

[91] D. Roddi, *Satellite Communications*, 4th. New York, USA: McGraw Hill, 2006.

[92] M. Sun and L. Yang, "On the joint time synchronization and source localization using TOA measurements", *International Journal of Distributed Sensor Networks*, vol. 2013, Feb. 2013.

[93] Y. Cao, P. Li, J. Li, L. Yang, and F. Guo, "A new iterative algorithm for geolocating a known altitude target using TDOA and FDOA measurements in the presence of satellite location uncertainty", *Chinese Journal of Aeronautics*, vol. 28, pp. 1510–1518, Sep. 2015.

[94] T. Pattison and S. I. Chou, "Sensitivity analysis of dual-satellite geolocation", *IEEE Transactions on Aerospace and Electronic Systems*, vol. 36, pp. 56–71, Jan. 2000.

[95] H. Yan, J. K. Cao, and L. Chen, "Study on location accuracy of dual-satellite geolocation system", in *Proc. IEEE International Conference on Signal Processing (ICSP)*, 2010, pp. 107–110.

[96] K. C. Ho and L. Yang, "On the use of a calibration emitter for source localization in the presence of sensor position uncertainty", *IEEE Transactions on Signal Processing*, vol. 56, pp. 5758–5772, Dec. 2008.

[97] L. Yang and K. C. Ho, "Alleviating sensor position error in source localization using calibration emitters at inaccurate locations", *IEEE Transactions on Signal Processing*, vol. 58, pp. 67–83, Jan. 2010.

[98] J. Li, F. Guo, L. Yang, and W. Jiang, "On the use of calibration sensors in source localization using TDOA and FDOA measurements", *Digital Signal Processing*, vol. 27, pp. 33–43, Apr. 2014.

[99] S. M. Kay, *Fundamentals of Statistical Signal Processing.* Prentice Hall, 1993.

[100] A. Yeredor, "On passive TDOA and FDOA localization using two sensors with no time or frequency synchronization", in *Proc. IEEE International Conference on Acoustics, Speech, and Signal Processing (ICASSP)*, 2013, pp. 4066–4070.

[101] O. Jean and A. J. Weiss, "Convex joint emitter localization and passive sensor network synchronization", in *Proc. IEEE Workshop on Sensor Array and Multichannel Signal Processing (SAM)*, 2012, pp. 201–204.

[102] S. Zhou and Z. Ding, "Joint synchronization and localization using TOAs: A linearization-based WLS solution", *IEEE Journal on Selected Areas in Communications*, vol. 28, pp. 1016–1025, Sep. 2010.

[103] Y. Wang, J. Huang, L. Yang, and Y. Xue, "TOA-based joint synchronization and source localization with random errors in sensor positions and sensor clock biases", *Ad Hoc Networks*, vol. 27, pp. 99–111, Apr. 2015.

[104] J. Liu, Z. Wang, J. Cui, S. Zhou, and B. Yang, "A joint time synchronization and localization design for mobile underwater sensor networks", *IEEE Transactions on Mobile Computing*, vol. 15, pp. 530–543, Mar. 2016.

[105] H. H. Fan and C. Yan, "Asynchronous differential TDOA for sensor self-localization", in *Proc. IEEE International Conference on Acoustics, Speech, and Signal Processing (ICASSP)*, 2007, pp. 1109–1112.

[106] C. Yan and H. H. Fan, "Asynchronous differential TDOA for non-GPS navigation using signals of opportunity", in *Proc. IEEE International Conference on Acoustics, Speech, and Signal Processing (ICASSP)*, 2008, pp. 5312–5315.

[107] Y. Wang, X. Ma, and G. Leus, "Robust time-based localization for asynchronous networks", *IEEE Transactions on Signal Processing*, vol. 59, pp. 4397–4410, Sep. 2011.

[108] Y. Wang and K. C. Ho, "TDOA source localization in the presence of synchronization clock bias and sensor position errors", *IEEE Transactions on Signal Processing*, vol. 61, Sep. 2013.

[109] P. D. Groves, *Principles of GNSS, Inertial, and Multisensor Integrated Navigation Systems*, 2nd. Boston, MA, USA: Artech House, 2013.

[110] P. Stoica and B. C. Ng, "On the Cramer-Rao bound for parametric constraints", *IEEE Signal Processing Letters*, vol. 5, pp. 177–179, Jul. 1998.

[111] T. J. Moor, R. J. Kozick, and B. M. Sadler, "The constrainted Cramer-Rao bound from the perspective of fitting a model", *IEEE Signal Processing Letters*, vol. 14, pp. 564–567, Aug. 2007.

[112] Y. Hu and G. Leus, "On a unified framework for linear nuisance parameters", *EURASIP Journal on Advances in Signal Processing*, vol. 2017, 2017.

[113] C.-I. Chang, "Orthogonal subspace projection (OSP) revisited: A comprehensive study and analysis", *IEEE Transactions on Geoscience and Remote Sensing*, vol. 43, pp. 502–518, Mar. 2005.

[114] M. Song and C.-I. Chang, "A theory of recursive orthogonal subspace projection for hyperspectral imaging", *IEEE Transactions on Geoscience and Remote Sensing*, vol. 53, pp. 3055–3072, Jun. 2015.

[115] H. Hmam, "Optimal sensor velocity configuration for tdoa-fdoa geolocation", *IEEE Transactions on Signal Processing*, vol. 65, pp. 628–637, Feb. 2017.